SPECTRAL DATABASE AND FRAMEWORK FOR COMPUTATIONALLY EFFICIENT CRYSTAL PLASTICITY SIMULATIONS

A Dissertation
Presented to
The Academic Faculty

by

Akash Gupta

In Partial Fulfillment
of the Requirements for the Degree
Doctor of Philosophy in the
George W. Woodruff School of Mechanical Engineering

Georgia Institute of Technology
December, 2020

SPECTRAL DATABASE AND FRAMEWORK FOR COMPUTATIONALLY EFFICIENT CRYSTAL PLASTICITY SIMULATIONS

Approved by:

Dr. Surya R. Kalidindi, Advisor
George W. Woodruff School of
Mechanical Engineering
Georgia Institute of Technology

Dr. Stephane Berbenni
George W. Woodruff School of
Mechanical Engineering
Georgia Institute of Technology Lorraine

Dr. Etienne Patoor
George W. Woodruff School of
Mechanical Engineering
Georgia Institute of Technology Lorraine

Dr. B. P. Gautham
TCS Research
Tata Consultancy Services

Dr. Luis Barrales Mora
George W. Woodruff School of
Mechanical Engineering
Georgia Institute of Technology Lorraine

Date Approved: November 20, 2020

Dedicated to my wife, Dr. Manisha Varshney (M.D.)

For her support, patience and sacrifices

ACKNOWLEDGEMENTS

I would like to thank my advisor Prof. Surya R. Kalidindi for his guidance and immense support over the years in research and non-research related matters without which this work was not possible. I am indebted to him for providing the opportunity and all the help during my higher studies and for all the invaluable feedback during the course of my research. I would also like to thank my other committee members Dr. Etienne Patoor, Dr. Luis Barrales Mora, Dr. Stephane Berbenni and Dr. B. P. Gautham for their valuable feedback. I would like to thank management of Tata Consultancy Services (TCS) especially Dr. B. P. Gautham, Dr. A. K. Singh, Dr. Pradip, Dr. Beena Rai and CTO Mr. K. Ananth Krishnan for their support over the years for this work. I am thankful to Dr. Etienne Patoor and management of Georgia Tech Lorraine for their assistance, guidance and support during my stay in France while I attended Georgia Tech Lorraine. I am also thankful to Office of Naval Research (ONR) for financial assistance under award number N00014-15-1-2478 for my stay in US while I attended Georgia Tech.

I am very thankful to former and present members of my research group Marat, Evdokia, David, Noah, Dipen, Almambet and Andrew for all their help and support in this research work. For all their help in non-technical matters I would like to express my sincere gratitude to student services and administrative staff at Georgia Tech Atlanta, Georgia Tech Lorraine and TRDDC TCS where I spent time doing this research work. I am also thankful to all my friends and well-wishers who helped and supported me in this endeavour over the years.

I would like to thank my parents, Pramod Kumar and Madhavi, and my siblings, Swapnil and Rahul, for their encouragement and support throughout this endeavour. Lastly, I am thankful to my wife, Mani for her invaluable advices and for being a pillar of support standing with me every step of the way. Without her continuous encouragement, I wouldn’t have been able to start or complete my higher studies.

TABLE OF CONTENTS

LIST OF TABLES

LIST OF FIGURES

LIST OF ABBREVIATIONS

FCC	Face Centered Cubic
C3D8	Continuum Three-Dimensional Eight-Noded Solid Element
CPFEM	Crystal Plasticity Finite Element Method
CP-FLD	Crystal Plasticity Forming Limit Diagram
DFTs	Discrete Fourier Transforms
FE	Finite Element
FEM	Finite Element Method
FLD	Forming Limit Diagram
FFT	Fast Fourier Transform
FZ	Fundamental Zone
GPU	Graphic Processing Unit
GSH	Generalized Spherical Harmonics
IDFTs	Inverse Discrete Fourier Transforms
MGI	Material Genome Initiative
M-K	Marciniak–Kuczynski
RVE	Representative Volume Element
SCPFEM	Spectral Crystal Plasticity Finite Element Method
SCP-FLD	Spectral Crystal Plasticity Forming Limit Diagram
UMAT	User Material Subroutine

SUMMARY

Most of the commercially used metals and alloys exhibit polycrystalline microstructures that are composed of numerous grains (individual crystals). In these metals and alloys, plastic deformation occurs mainly through the movement of dislocations in specific crystallographic planes and directions. Crystal plasticity models have been developed and used over the past several decades to describe physically the behavior of metals. They not only provide better predictions of the anisotropic material response but can also capture the texture evolution in a polycrystalline sample subjected to finite plastic deformation. Hence they present an important avenue for improving the fidelity of multiscale modeling and simulation. However, crystal plasticity models are extremely computationally expensive, limiting their adoption by materials development community and manufacturing industries. In this work, this limitation is addressed by using a recently developed spectral database approach based on discrete Fourier transforms (DFTs). This approach has demonstrated impressive computational advantages over the conventional approaches that explicitly solve the governing constitutive equations using sophisticated numerical algorithms. In this approach, the important variables of interest from crystal plasticity computations can be stored in precomputed databases based on DFTs. Although the database generation requires one-time high computational cost, it dramatically reduces the computational cost in all subsequent computations.

Despite their wide applicability, in some applications the DFT database approach has encountered significant hurdles such as for prediction of crystal plasticity based

forming limit diagram (CP-FLD) and for carrying out simulations of crystal plasticity finite element method (CPFEM). Forming limit diagram (FLD) is the most commonly used indicator of localized necking in automotive industry. In this work, the main hurdles encountered are tracked to certain unintended biases introduced in the formulation of the first generation spectral DFT databases. Specific strategies have been designed and implemented to address these biases in this work. Significant improvements were made to the prior approach and a new DFT database (second generation) was developed for Face Centered Cubic (FCC) metals to address the challenges of predictions of CP-FLD and for performing simulations of CPFEM in a highly computationally efficient manner. This is achieved using developed numerical tools of spectral crystal plasticity forming limit diagram (SCP-FLD) and spectral crystal plasticity finite element method (SCPFEM) framework. Efficiency of the DFT database approach is demonstrated by a significant reduction in the computational cost involved in CP-FLD predictions. With the development of fast and robust SCP-FLD numerical tool, the accurate predictions of forming limit diagrams could be done very efficiently. The new DFT database and framework was also implemented with commercial finite elements (FE) package ABAQUS through a user materials subroutine, UMAT. These improvements to the spectral databases and SCPFEM framework implemented in this work has shown to improve markedly the accuracy of the database solutions for both the stress-strain responses as well as the stability of jacobians needed in finite element computations. The benefits of the improved databases are demonstrated with selected case studies using SCPFEM numerical tool. Proper utilization of these toolsets can lead to accelerated insertion of new and improved materials into practice.

CHAPTER 1. INTRODUCTION

After the introduction of Materials Genome Initiative (MGI) in 2011, focus of materials development community shifted to accelerated discovery, development and deployment of advanced materials using the confluence of computational tools, experimental tools and digital data (McDowell and Kalidindi, 2016). The success stories of initial phase of MGI have concluded that through the continuing application of data-driven, integrated efforts in experiment, theory, and computation, the extraordinary advances can be obtained which are capable of generating a new generation of advanced materials and materials innovators capable of transformative impact (Pablo et al., 2019). The computational tools were developed for material simulations to cut down the need for large number of time consuming expensive experiments, but for simulating complex material system and processes, huge computational time and resources are needed which increases by many folds for the simulations conducted at lower length scales presenting as bottleneck. This research work presents an example of fast and robust numerical framework based on spectral DFT database which can be used to speed up physics based computational tools for crystal plasticity computations.

Plastic deformation shapes and strengthens the products in metal forming processes. Plasticity also influences material failure (e.g., necking and fracture, fatigue). Consequently, a deeper understanding of plastic deformation in metals and alloys is central to efforts aimed at improving the manufacturing processes for optimizing the cost and the performance of the finished product. Plasticity describes the deformation of a (solid) material undergoing non-reversible changes of shape in response to applied forces

(Lubliner, 2008). In metals and alloys the occurrence of plastic deformations at the micro-scale is due to the motion of dislocations. Most of the commercially used metals and alloys exhibit polycrystalline microstructures that are composed of numerous grains (individual crystals). In such materials, plastic deformation occurs predominantly by dislocation glide on specific crystallographic planes (typically close-packed planes) in specific crystallographic directions (typically close-packed directions) (Callister, 2007). Consequently, the details of the material microstructure (such as the distribution of grain orientations, also referred as the crystallographic texture) play an important role in plasticity (Barlat, 2007). The elastic–plastic deformation of crystalline aggregates depends on the direction of loading, i.e. crystals are mechanically anisotropic.

Most simulations of deformation processing operations on metals employ phenomenological descriptions of the constitutive laws controlling the macroscale (effective) elastic-plastic response of polycrystalline materials. Although such models require relatively short computation times, they are often not able to capture accurately the evolving anisotropy and properties (i.e., mechanical performance) of the finished product. In such situations, it is essential to employ more physics-based descriptions of the material constitutive laws. For crystalline solids, these can be expressed in the form of crystal plasticity theories (Adams et al., 2013). A salient feature of these models is that they aim to express the constitutive relations of the material starting from the description of the key physical mechanisms at the single crystal scale. These constitutive relations account for the relevant microstructural mechanisms at this scale, such as slip on specific crystallographic planes and directions, the lattice rotation, and the dislocation motion and multiplication in the description of strain hardening. The behavior at the macroscale is

then subsequently derived from that of the constituent single crystals via suitable scale-transition schemes. Such micromechanical modeling approaches have demonstrated significant improvements in the predictions of the concomitant anisotropic mechanical response in polycrystalline materials and the evolution of the underlying texture in finite plastic deformation. Crystal plasticity models have been developed and used over the past several decades to describe physically the behavior of metals by accounting for the details of their microstructure and the crystallography of the prevalent grain scale deformation mechanisms at length scales smaller than a single crystal or individual grains in a polycrystalline sample (e.g., Asaro and Needleman, 1985; Bronkhorst et al., 1992; Kalidindi et al., 1992; Beaudoin et al., 1995).

The transition from the response of single crystals to the overall (effective) response of the polycrystalline aggregate is usually accomplished using a suitable homogenization scheme. The commonly employed homogenization schemes can be classified based on the assumptions made with regards to the local interactions between grains, such as Taylor-type (also known as full constraints) (Taylor, 1938), relaxed constraints (Kocks and Mecking, 2003), LAMEL (Van Houtte et al., 2005), self-consistent (Molinari et al., 1987; Lebensohn et al., 2004, 2007), and crystal plasticity finite element (Needleman et al., 1985; Kalidindi et al., 1992; Kalidindi and Anand, 1994; Bachu and Kalidindi, 1998; Kalidindi and Schoenfeld, 2000; Raabe et al., 2005) models. These models can be differentiated based on the assumptions made with regard to the local interactions between the constituent grains. For example, the Taylor-type model assumes that there is no local interaction between the grains. The self-consistent approach assumes that each crystal acts as an ellipsoidal inclusion embedded in a

homogenous effective medium that has uniform property. Therefore, the local interaction between each crystal and the neighboring crystals is taken in an average sense over the complete polycrystal. Furthermore, the CPFEM takes into account the local interaction between each grain and their neighbors by satisfying the equilibrium and compatibility conditions between the grains. The simplest and the most widely used approach is the Taylor-type model. In this method, the applied velocity gradient tensor at the microscale is assumed to be the same as the one applied at the macroscale (on the polycrystal). The macroscopic stress is obtained as a volume average over the entire polycrystalline aggregate. The Taylor-type model usually provides good predictions of the overall anisotropic stress-strain response and the averaged texture evolution for single-phase, high stacking faulty energy, cubic metals (Bronkhorst et al., 1992). However, it usually lacks good predictions at the scale of individual crystals and it fails to capture the development of heterogeneities within the grains (Kalidindi, 2004; Van Houtte et al., 2005). Crystal plasticity finite element method (CPFEM) offers a powerful tool for modeling a wide range of mechanical problems that take into account the local interactions between all grains in the sample. CPFEM simulations have been successfully employed in prior literature in two different ways: (i) the constitutive response at each integration point is defined using a single crystal plasticity theory (Beaudoin et al., 1995; Anand, 2004), and (ii) each integration point was assumed to correspond to a polycrystalline material point whose constitutive response is prescribed by a suitable mean-field homogenization scheme (Kalidindi et al., 1992; Roters et al., 2010). Because of their tremendous successes, crystal plasticity theories and their implementations have attracted substantial attention for addressing problems requiring consideration of the

microscale details of plastic deformation experienced in a variety of deformation processing operations on metals (Kalidindi et al., 1992; Beaudoin et al., 1994; Kumar and Dawson, 1995; Raabe et al., 2005).

However, crystal plasticity models are extremely computationally expensive, limiting their wide adoption by materials development community and manufacturing industries. Even when the constitutive equations are developed and implemented efficiently, the time integration of the highly nonlinear single crystal response demands high computational resources. Consequently, in recent years, much attention has been devoted to the development of novel techniques that reduce the computational cost involved, without significant loss of accuracy. Various strategies have been explored both related to advanced numerical procedures and computer architecture in order to speed up the crystal plasticity computations. These have included the Bunge–Esling approach (Bunge and Esling, 1984; Li et al., 2003; Kalidindi and Duvvuru, 2005), direct fast Fourier transform (FFT)-based formulation (Lebensohn, 2001; Lebensohn et al., 2008; Grennerat et al., 2012), parallel implementations of FFT-based formulation on CPU's using OpenMP and MPI (Eghtesad et al., 2018a), Newton–Krylov method in place of the Newton–Raphson (NR) method for solving sets of highly nonlinear crystal plasticity equations (Chockalingam et al., 2013), reduced order model based on machine learning (Yuan et al., 2018; Reimann et al., 2019) and the database approaches which rely primarily on databases of precomputed solutions either in the form of Fourier (spectral) coefficients of the generalized spherical harmonics (GSH) (Kalidindi et al., 2006) or discrete Fourier transforms (DFTs) with homogenization schemes of Taylor-type or crystal plasticity finite element (Knezevic et al., 2008; Alharbi and Kalidindi, 2015;

Zecevic et al., 2015a, 2015b). Among these, the database approaches have demonstrated the most dramatic reduction in the computational cost without any significant loss of accuracy. This is mainly because the database approaches retrieve the solutions to the single crystal constitutive equations from the pre-computed databases instead of computing them directly (e.g., using the iterative NR method). More recently, DFT database was also coupled with direct FFT-based formulation (Lebensohn et al., 2008) and found to be computationally efficient compared to conventional direct FFT-solver (Eghtesad et al., 2018b). Some efforts have also been focused on using a specialized computer hardware that utilizes graphics-processing units (GPU) to perform crystal plasticity calculations using DFT database (Knezevic and Savage, 2014 ; Mihaila et. al, 2014; Savage and Knezevic, 2015). The viability and the computational benefits of using the DFT database approach (for facilitating crystal plasticity solutions) have already been highlighted in prior work (cf. Knezevic et al., 2008, 2009; Kalidindi et al., 2009; Alharbi et al., 2010; Knezevic and Savage, 2014; Alharbi and Kalidindi, 2015; Zecevic et al., 2015a, 2015b; Knezevic and Kalidindi, 2017; Eghtesad et al., 2018b; Kalidindi et al., 2018). In this research work also, a compact spectral database approach, based on the discrete Fourier transforms (DFTs), is successfully used to speed up the conventional crystal plasticity computations.

In this thesis work, the new DFTs-based database and framework for speeding up the conventional crystal plasticity computations is presented and its efficiency is demonstrated using case studies. Details of spectral DFT database and framework will be demonstrated and validated through example case studies on Face Centered Cubic (FCC) metals. Despite their wide applicability, in some applications the DFT database approach

has encountered significant hurdles such as for prediction of crystal plasticity based forming limit diagram (CP-FLD) and for carrying out simulations of crystal plasticity finite element method (CPFEM). In this study, these hurdles are tracked to certain biases introduced inadvertently in the formulation of the first-generation spectral databases. These biases cause inaccuracies for some special cases in the computation of stress-strain responses and also cause instabilities in the computation of the jacobians needed in the finite element computations. These issues currently hinders application of spectral crystal plasticity forming limit diagram (SCP-FLD) framework for fast and accurate predictions of FLD and also preclude the application of spectral crystal plasticity finite element method (SCPFEM) framework to the broader range of problems as the iterations employed to solve the governing equilibrium equations for arbitrary heterogeneous deformations do not converge. In this work, the origins of these issues are carefully tracked, and strategies are designed and implemented to specifically address them. Significant improvements were made to the prior approach and a new spectral database (second generation DFT database) and framework was developed to address the challenges of predictions of CP-FLD and for performing simulations of CPFEM in a highly computationally efficient manner using developed numerical tools of SCP-FLD and SCPFEM respectively. This research work presents the first application of the DFT spectral database strategy to predict localized necking and the associated FLDs of thin metal sheets, represented as spectral crystal plasticity forming limit diagram (SCP-FLD). This new tool is presented and validated in this work by comparing the predicted SCP-FLDs with the predictions from conventional methods (CP-FLD) and it is demonstrated that the strategy proposed here leads to major savings of computational cost (96%

reduction in the computational cost for FLD predictions). A new DFT database free of the discovered biases was also integrated with a user material subroutine (UMAT) in the commercial FEM software ABAQUS (referred henceforth as spectral UMAT). In this implementation, an FE integration point can represent a single crystal or a polycrystalline material point whose meso-scale mechanical response is obtained by the mean-field Taylor-type homogenization scheme. This new spectral UMAT has been found to improve the accuracy and convergence characteristics of the SCPFEM simulations, and is demonstrated in this work with selected case studies. This work establishes the necessary foundations to advance the implementation of the SCPFEM framework to carry out computationally efficient simulations of complex metal forming operations such as deep drawing.

Outline of this thesis is as follows, Chapter 2 details the background of crystal plasticity framework, spectral DFT databases, spectral crystal plasticity framework and its coupling with finite element method. Chapter 3 describes the limitations of first generation DFT database and details the steps involved in development of new and improved second generation spectral DFT database for Face Centered Cubic (FCC) material. In Chapter 4, the new spectral DFT database is critically evaluated by application to crystal plasticity based forming limit diagram predictions. This chapter details all the numerical aspects of SCP-FLD numerical tool and comparative results. Chapter 5 discusses the details to implement new DFT database in finite elements by integrating it with UMAT in ABAQUS to perform computationally efficient SCPFEM simulations. All the improvements made to SCPFEM numerical framework have been

discussed along with key results from selected case studies. Chapter 6 discusses the conclusions drawn from this research work and scope for future work.

CHAPTER 2. BACKGROUND

2.1 Framework for Crystal Plasticity

Crystal plasticity theories allow physics-based formulations of the constitutive equations that not only provide better predictions of the anisotropic plastic response but also capture the details of microstructure evolution such as the formation of crystallographic texture. A distribution of all orientations of crystals with respect to the sample frame in a polycrystalline aggregate is referred to as crystallographic texture. Crystallographic texture is widely recognized as an important detail of the microstructure in polycrystalline materials that is known to have a strong influence on their macro scale anisotropic elastic-plastic properties. The high computational time required to solve the highly nonlinear, numerically stiff, crystal plasticity constitutive equations makes the application of these theories impractical in simulating large scale applications. In this section, we first review briefly the details of the single crystal viscoplastic constitutive equations (Asaro and Needleman, 1985) used to generate the DFT database. In crystal plasticity (CP) models, plastic deformation is assumed to be produced only by slip on specified crystallographic slip systems. The resulting plastic flow rule is expressed as

$$\mathbf{D}^{\boldsymbol{p}} = \sum_{\alpha} \dot{\gamma}^{\alpha}\, \mathbf{P}^{\alpha}\ , \quad \mathbf{P}^{\alpha} = 0.5(\mathbf{m}^{\alpha} \otimes \mathbf{n}^{\alpha} + \mathbf{n}^{\alpha} \otimes \mathbf{m}^{\alpha}) \tag{2.1}$$

$$\dot{\gamma}^{\alpha} = \dot{\gamma}_0 \left|\frac{\tau^{\alpha}}{s^{\alpha}}\right|^{\frac{1}{m}} sgn(\tau^{\alpha}),\ \ \tau^{\alpha} = \boldsymbol{\sigma}' \cdot \mathbf{P}^{\alpha} \tag{2.2}$$

where $\mathbf{D}^{\boldsymbol{p}}$ is the applied isochoric plastic stretching tensor, $\boldsymbol{\sigma}'$ is the deviatoric part of the Cauchy stress tensor, $\dot{\gamma}^{\alpha}$ is the shearing rate on slip system α, τ^{α} is the resolved shear

stress on slip system α, s^{α} is the slip resistance on slip system α, $\dot{\gamma}_0$ is the reference value of the shearing rate, m is the strain rate sensitivity parameter, and $\mathbf{m}^{\alpha}$ and $\mathbf{n}^{\alpha}$ denote the slip direction and the slip plane normal of the slip system α, respectively. For cubic metals, the evolution of the slip resistance can be described by a simple saturation-type law expressed as

$$\dot{s}^{\alpha} = h_0 \left(1 - \frac{s^{\alpha}}{s^{s}}\right)^{a} \sum_{\beta} |\dot{\gamma}^{\beta}| \tag{2.3}$$

where h_0, s^s and a denote the slip hardening parameters. The lattice spin tensor $\mathbf{W}^*$ (and the related lattice rotation tensor, $\mathbf{R}^*$) in the crystalline region are expressed as

$$\mathbf{W}^* = \dot{\mathbf{R}}^* \mathbf{R}^{*\mathrm{T}} = \mathbf{W} - \mathbf{W}^{p}, \qquad \mathbf{W}^{\boldsymbol{p}} = \sum_{\alpha} 0.5 \dot{\gamma}^{\alpha} (\mathbf{m}^{\alpha} \otimes \mathbf{n}^{\alpha} - \mathbf{n}^{\alpha} \otimes \mathbf{m}^{\alpha}) \tag{2.4}$$

where $\mathbf{W}$ is the applied spin tensor, and $\mathbf{W}^{\boldsymbol{p}}$ is the plastic spin tensor.

Sophisticated numerical approaches have been presented in literature (Kalidindi et al., 1992) for the fully-implicit time-integration of the crystal plasticity equations presented in Eqs. (2.1)-(2.4). However, these schemes incur high computational cost because of the very low values of the strain rate sensitivity parameter, m. Typically, the value of m is measured to be around 0.01 for plastic deformation in metals at low homologous temperatures (Asaro and Needleman, 1985).

2.2 Spectral DFT database for Crystal Plasticity computations

Spectral analysis is the process of identifying embedded frequencies in data. Real situations data is generally available at discrete set of points in space rather than on a continuous domain. For discrete data, the computational basis of spectral analysis is

discrete Fourier transforms (DFTs). DFTs transform time- or space-based data into frequency-based data (Adams et al., 2012). Suppose we have a function, f, defined on discrete grid of points, x_n, where n takes values from 0 to $N-1$. Let the value of function at x_n be f_n; then the discrete Fourier transform (DFT) of f can be written as

$$F_k = \sum_{n=0}^{N-1} f_n e^{-2\pi i k n/N} \tag{2.5}$$

F_k are the Fourier coefficients of function f. One-to-one mapping between the signals in spatial domain and spatial frequency domains holds for DFT. Thus the inverse discrete Fourier transform (IDFT) to transform from frequency space back to real space can be written as

$$f_n = \frac{1}{N} \sum_{k=0}^{N-1} F_k e^{2\pi i k n/N} \tag{2.6}$$

From DFT and IDFT equations it can be seen that if one knows frequency response F_k, any value f_n can be recovered individually as there is no dependence between the values of f_n in IDFT expression (this holds for vice versa as well).

The crystal plasticity framework demands significant computational resources. The numerically stiff behavior of the crystal plasticity constitutive equations is a direct consequence of the fact that most metals have a very weak dependence on strain rate at room temperature, demanding the use of a small value for the strain rate sensitivity parameter in the flow rule (Eq. (2.2)). Consequently, one typically needs several iterations to arrive at an acceptable solution. Additionally, the constitutive equations need to be solved several times in most crystal plasticity simulations. For example, the implementation of the crystal plasticity equations in a finite element tool requires solving

the set of stiff constitutive equations for every crystal orientation at every integration point at every trial strain increment in the simulations. Consequently, the use of crystal plasticity models for simulating practical engineering problems requires extremely high computational effort. The main idea behind the DFT database approach (Knezevic et al., 2008, 2009; Alharbi and Kalidindi, 2015) for speeding up the crystal plasticity computations is to capture the solutions in an efficient database of DTFs that can be used for all subsequent crystal plasticity computations. In other words, once this database is built, one would use the database directly instead of explicitly solving Eqs. (2.1)-(2.4). The viability of such a database approach has been demonstrated in prior work (Knezevic et al., 2008, 2009; Knezevic and Savage, 2014; Alharbi and Kalidindi, 2015), and essentially involved establishing compact DFT-based representations for three functions: (i) $\boldsymbol{\sigma}'(\mathrm{g}, \mathbf{L^p})$, (ii) $\mathbf{W}^{\boldsymbol{p}}(\mathrm{g}, \mathbf{L^p})$, and (iii) $\sum_\alpha |\dot{\gamma}^\alpha|(\mathrm{g}, \mathbf{L^p})$, where g denotes the crystal lattice orientation (represented using Bunge–Euler angles (Bunge, 1993)) and $\mathbf{L^p}$ is the traceless applied plastic velocity gradient tensor.

The central challenge in establishing the functions mentioned above comes from the large unwieldy space of $\mathbf{L^p}$ (i.e., the set of all possible values assigned to $\mathbf{L^p}$). A suitable parameterization was devised following the work of Van Houtte (1994). This parameterization is expressed as

$$\mathbf{L^p} = \dot{\varepsilon}\mathbf{D}_0 + \mathbf{W},\ \mathbf{D}_0 = \sum_{j=1}^{3} \mathrm{D_j}\, \mathbf{e}_j^{\mathrm{p}} \otimes \mathbf{e}_j^{\mathrm{p}},\quad \dot{\varepsilon} = \frac{1}{2}||\mathbf{L^p} + (\mathbf{L^p})^{\mathbf{T}}|| \tag{2.7}$$

$$\mathrm{D}_1 = \sqrt{\frac{2}{3}}\cos\left(\theta - \frac{\pi}{3}\right),\ \ \mathrm{D}_2 = \sqrt{\frac{2}{3}}\cos\left(\theta + \frac{\pi}{3}\right),\quad \mathrm{D}_3 = -\sqrt{\frac{2}{3}}\cos(\theta) \tag{2.8}$$

where $\left\{\mathbf{e}_{\mathrm{j}}^{\mathrm{p}},\ \mathrm{j}=1,2,3\right\}$ denote the principal frame of the unit traceless $\mathbf{D}_0$. In the DFT database approach, all of the crystal plasticity calculations are performed in this principal frame, and subsequently converted back to the sample reference frame. As a result of the strategies described above, the functions of interest for crystal plasticity computations can be expressed as $\boldsymbol{\sigma}'(\mathrm{g}^{\mathrm{p}},\theta,\dot{\varepsilon})$, $\mathbf{W}^{\boldsymbol{p}}(\mathrm{g}^{\mathrm{p}},\ \theta,\ \dot{\varepsilon})$, and $\sum_{\alpha}|\dot{\gamma}^{\alpha}|(\mathrm{g}^{\mathrm{p}},\theta,\dot{\varepsilon})$, where g^{p} denote the crystal orientation with respect to $\left\{\mathrm{e}_{\mathrm{j}}^{\mathrm{p}}\right\}$ reference frame and is most conveniently described by a set of three Bunge–Euler angles denoted as $(\varphi_1,\Phi,\varphi_2)$. The dependence on $\dot{\varepsilon}$ in the desired functions can be inferred from Eqs. (2.1)-(2.4) and built directly into the DFT-based expressions for these functions. Therefore, we will focus now mainly on the variables g^{p} and θ. For the most general case, the orientation space (i.e., the complete set of all possible orientations) can be described as $(\varphi_1\epsilon\,[0,2\pi),\Phi\epsilon\,[0,2\pi),\varphi_2\epsilon\,[0,2\pi))$. Although the crystal and sample symmetries generally identify a significantly smaller domain as the fundamental zone (i.e., the set of all distinct crystal orientations), it is most convenient to stay with the full orientation space as it is naturally periodic and therefore ideally suited for obtaining compact DFT representations for the functions of interest. For the variable θ, we identify its periodic domain also as $\theta\,\epsilon\,[0,2\pi)$. The identification of these periodic domains allows us to represent the functions of interest as DFTs computed using function values obtained on a uniform 4-D (four-dimensional) grid defined on $(\varphi_1,\Phi,\varphi_2,\theta)$. This does entail a significant computational cost for building the database. However, the main benefit of the DFT database approach is that building the database constitutes a one-time cost. In other words, there would be no need to rebuild this database as long as Eqs. (2.1)-(2.4) remain the same. If we select the slip systems of fcc single crystals for $\mathbf{m}^{\alpha}$ and $\mathbf{n}^{\alpha}$ in these equations then the built database is expected to

produce crystal plasticity solutions based on Eqs. (2.1)-(2.4) for any fcc metal. Furthermore, the functions $\boldsymbol{\sigma}'(\mathrm{g^p}, \theta, \dot{\varepsilon})$, $\mathbf{W^p}(\mathrm{g^p}, \theta, \dot{\varepsilon})$, and $\sum_\alpha |\dot{\gamma}^\alpha|(\mathrm{g^p}, \theta, \dot{\varepsilon})$ are insensitive to the values of the slip hardening parameters h_0, s^s and a as well as to the initial value of the slip resistance (s_0). Therefore, the database built using the strategies described above is expected to be applicable in a very broad range of crystal plasticity computations.

In DFT representations of functions, one establishes a rigorous one-to-one map between the discretized values of the function samples on a uniform grid and the Fourier coefficients obtained using a set of discrete frequencies (the number of discrete function values and the number of discrete frequencies utilized are kept the same to produce a one-to-one map between these fully equivalent representations). For the present case, the DFT representations of interest are expressed as (Knezevic et al., 2008, 2009; Alharbi and Kalidindi, 2015):

$$\mathbf{W}^{\boldsymbol{p}}_{\alpha\beta\gamma\delta} = \dot{\varepsilon}\frac{1}{N_{\varphi_1} N_{\varphi} N_{\varphi_2} N_{\theta}} \sum_{k=0}^{N_{\varphi_1}-1} \sum_{l=0}^{N_{\varphi}-1} \sum_{m=0}^{N_{\varphi_2}-1} \sum_{n=0}^{N_{\theta}-1} \mathbf{B}_{klmn}\, e^{\frac{2\pi i k\alpha}{N_{\varphi_1}}} e^{\frac{2\pi i l\beta}{N_{\varphi}}} e^{\frac{2\pi i m\gamma}{N_{\varphi_2}}} e^{\frac{2\pi i n\delta}{N_{\theta}}} \tag{2.9}$$

$$\boldsymbol{\sigma}'_{\alpha\beta\gamma\delta} = s\,\dot{\varepsilon}^m \frac{1}{N_{\varphi_1} N_{\varphi} N_{\varphi_2} N_{\theta}} \sum_{k=0}^{N_{\varphi_1}-1} \sum_{l=0}^{N_{\varphi}-1} \sum_{m=0}^{N_{\varphi_2}-1} \sum_{n=0}^{N_{\theta}-1} \mathbf{C}_{klmn}\, e^{\frac{2\pi i k\alpha}{N_{\varphi_1}}} e^{\frac{2\pi i l\beta}{N_{\varphi}}} e^{\frac{2\pi i m\gamma}{N_{\varphi_2}}} e^{\frac{2\pi i n\delta}{N_{\theta}}} \tag{2.10}$$

$$\left(\sum_\alpha |\dot{\gamma}^\alpha|\right)_{\alpha\beta\gamma\delta} = \dot{\varepsilon}\frac{1}{N_{\varphi_1} N_{\varphi} N_{\varphi_2} N_{\theta}} \sum_{k=0}^{N_{\varphi_1}-1} \sum_{l=0}^{N_{\varphi}-1} \sum_{m=0}^{N_{\varphi_2}-1} \sum_{n=0}^{N_{\theta}-1} \mathrm{G}_{klmn}\, e^{\frac{2\pi i k\alpha}{N_{\varphi_1}}} e^{\frac{2\pi i l\beta}{N_{\varphi}}} e^{\frac{2\pi i m\gamma}{N_{\varphi_2}}} e^{\frac{2\pi i n\delta}{N_{\theta}}} \tag{2.11}$$

In Eqs. (2.9)-(2.11), α, β, γ and δ enumerate the grid points in the orientation space (domain of g^p expressed as $(\varphi_1, \Phi, \varphi_2)$) and the θ space (describing the deformation mode), respectively, while $N_{\varphi_1}, N_{\varphi}, N_{\varphi_2}$ and N_{θ} represent the corresponding total number of grid points for each variable involved. Note that the variables α, β, γ and δ take non-negative integer values following the standard practice in DFT representations. $\mathbf{B}_{klmn}$, $\mathbf{C}_{klmn}$, G_{klmn} denote the DFTs and constitute the spectral databases needed for facilitating the fast crystal plasticity solutions described here. Eqs. (2.9) and (2.10) are to be applied to each tensor component involved, i.e., three independent components of $\mathbf{W}^{\boldsymbol{p}}$ and five independent components of $\boldsymbol{\sigma}'$, respectively. For computing the desired DFT database, the values of the functions of interest were first computed on a uniform 4-D grid of $(\varphi_1, \Phi, \varphi_2, \theta)$ using Eqns. (2.1)-(2.4) and previously established numerical approaches (Kalidindi et al., 1992). In first generation database, this was accomplished using a regular three-degree grid in each of the angular variables involved which means that 4-D grid was of size 120 x 120 x 120 x 120. These computed values on the grid points of interest were then used to compute the DFT databases.

In applying the DFT databases for estimating the function values for new inputs (i.e., any new values of $(\varphi_1, \Phi, \varphi_2, \theta)$ that were not used in computing the DFTs), the trignometric interpolation scheme presented by Zecevic et al. (2015a) is the preferred option. Given a set of crystal orientations, an initial value of slip resistance per crystal orientation, constitutive parameters and an imposed value of the strain rate tensor, we can use Eqs. (2.9)-(2.11) which are simply series evaluations to compute required microscale quantities (i.e. grain scale stress, grain spin, and shearing rates on slip systems). The deformation process can be simulated after applying strain increment steps in stand-alone

SCP framework. The spin tensor of individual crystals is used for their reorientation. The updated set of crystal orientations enters the next strain increment. Total shear rate is used to update the slip resistance for the next strain increment. For a polycrystalline response i.e. macroscale quantities (homogenized stress–strain response and texture) we use the Taylor model, in which the applied strain rate tensor at the grain level is assumed to be the same as the one applied at the polycrystal level. The macroscopic stress for the polycrystal is then obtained by volume averaging the stresses inside the polycrystal. One uses only a small number of DFTs (called dominant DFTs) that exhibit the highest magnitudes among the full set of DFTs. In fact, Knezevic et al. (2009) have demonstrated that as few as 200 DFTs dominate the representations shown in Eqs. (2.9)-(2.11). It was found that the loss in accuracy with retaining only the dominant DFTs is not very significant. The main advantage of this strategy is that the use of a small number of dominant DFTs speeds up crystal plasticity calculations by about two orders of magnitude when compared with the conventional computations with only a slight trade-off in accuracy (Knezevic et al., 2009). More specifically, it was shown that the plane strain compression simulation of polycrystalline aggregate of 1000 discrete crystal orientations took 108 s on a regular Pentium 4 desktop PC using the conventional crystal plasticity algorithms (solving explicitly Eqs. (2.1)-(2.4)), but only 2.3 s using a database of dominant DFTs (500 for stress and shearing rate, and 3000 for lattice spin). Knezevic and Savage (2014) demonstrated speed ups exceeding three orders of magnitude compared to the conventional numerical schemes by using GPUs. Spectral DFT database can also be coupled with FE framework details of which are presented next.

2.3 Implementation of Spectral DFT database in Finite Element Models

The use of the DFT database in the Taylor-type model (Knezevic et al., 2009) was based on the assumption of a uniform deformation gradient in all of the grains in the polycrystalline aggregate. However, this assumption can be relaxed in a CPFEM framework that numerically solves the governing equilibrium equations while satisfying the material constitutive laws based on crystal plasticity theories (Kalidindi et al., 1992; Kalidindi and Anand, 1994; Raabe et al., 2005; Roters et al., 2010). The DFT databases have also been used to speed-up CPFEM computations in a new framework called the SCPFEM (Spectral CPFEM) framework (Alharbi and Kalidindi, 2015; Zecevic et al., 2015a, 2015b). In this framework, the DFT databases were integrated with the commercial finite element package ABAQUS through a user defined constitutive behavior of the material implemented in a UMAT subroutine (ABAQUS, 2010). The UMAT is called for each integration point of the FE mesh, at each trial time increment in the FE simulation. For each call to the UMAT, the total deformation gradient tensors at the beginning of the time step ($\mathbf{F}(\mathrm{t})$) and at the end of the time increment ($\mathbf{F}(\mathrm{t}+\Delta\mathrm{t})$), material parameters (including the elastic constants (C_{11}, C_{12}, C_{44}) and the slip hardening parameters in Eq. (2.3)) along with a number of other relevant variables (including the current crystal orientation and the current value of the slip resistance) are provided as inputs, while the stress tensor ($\boldsymbol{\sigma}$) and the updated state variables at the end of the time increment as well as the Jacobian ($\frac{\partial \Delta \boldsymbol{\sigma}}{\partial \Delta \boldsymbol{\varepsilon}}$) are returned as outputs. The desired function of the UMAT is depicted schematically in Figure 2.1. If the updated stress field does not satisfy the weak form of the equilibrium equations in the overall polycrystalline being modelled, the Jacobian is used for obtaining an improved guess for the displacement field at the end of the specified time increment (the deformation gradient tensor provided as

input to the UMAT is computed from this field). This procedure is repeated until convergence is achieved at each time increment. As an extension to the SCPFEM framework, one can easily consider multiple grains at each integration point, if a Taylor-type model is invoked.

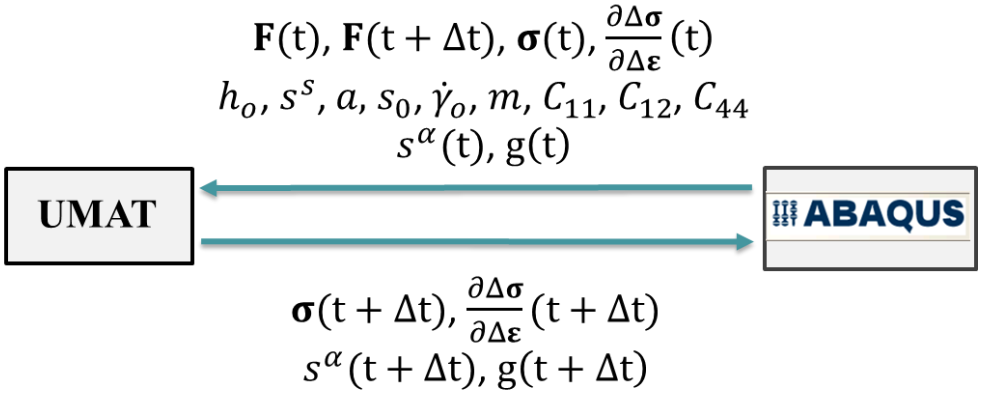

Figure 2.1: Schematic depiction of the information exchange between ABAQUS and UMAT in the SCPFEM framework.

The implementation of the SCPFEM framework in ABAQUS involved two main tasks (Alharbi and Kalidindi, 2015). First, the crystal plasticity computations using spectral databases were extended from rigid-viscoplastic to elastic-viscoplastic deformation (ABAQUS provides the total deformation gradient at each integration point as an input to the UMAT and expects to be returned the full stress tensor, not just the deviatoric stress tensor). Second, the fourth-rank Jacobian (defined as the derivative of the stress tensor with respect to the increment in strain tensor) needed to be computed efficiently to facilitate fast convergence of equilibrium iterations in the implicit finite element code ABAQUS. The spectral crystal plasticity approach described in section 2.2 can be expanded to include elasticity using the following constitutive relations

$$\boldsymbol{\sigma}^{\boldsymbol{\nabla}*} = \widetilde{\boldsymbol{\mathcal{L}}}\,\mathbf{D}^{*} \tag{2.12}$$

where $\mathbf{D}^{*}$ is the elastic stretching tensor, $\widetilde{\boldsymbol{\mathcal{L}}}$ is the 4$^{\text{th}}$-rank elasticity tensor in the current (deformed) configuration, and $\boldsymbol{\sigma}^{\boldsymbol{\nabla}*}$ is the Jaumann rate of the Cauchy stress based on the lattice spin and is defined as

$$\boldsymbol{\sigma}^{\boldsymbol{\nabla}*} = \dot{\boldsymbol{\sigma}} - \mathbf{W}^{*}\boldsymbol{\sigma} + \boldsymbol{\sigma}\mathbf{W}^{*} \tag{2.13}$$

In order to use the above relations, the total stretching tensor $\mathbf{D}$ (symmetric part of the velocity gradient tensor) needs to be decomposed into elastic and plastic parts. This decomposition must be accomplished such that the deviatoric stresses computed from both the crystal plasticity DFT databases (based on Eq. (2.10)), denoted here as $\boldsymbol{\sigma}'^{\mathrm{DFT}}(\mathbf{D}^{p})$) and the above Jaumann rate relations (denoted as $\boldsymbol{\sigma}'^{\mathrm{Jmn}}(\mathbf{D}^{*}, \mathbf{W}^{*}, \Delta\mathrm{t})$) are equal to each other within an acceptable tolerance. The trace of the stretching tensor contributes exclusively to the elastic deformation, and as a consequence, only the deviatoric stretching tensor ($\mathbf{D}'$) need to be decomposed into elastic and plastic parts. An iterative protocol to address this problem was developed and demonstrated by Alharbi and Kalidindi (2015).

The computation of the Jacobian needed for the UMAT in ABAQUS is defined as

$$\boldsymbol{\mathcal{J}} = \frac{\partial \Delta\boldsymbol{\sigma}}{\partial \Delta\boldsymbol{\varepsilon}} \equiv \frac{\partial \boldsymbol{\sigma}}{\partial \mathbf{E}_{t}} \tag{2.14}$$

where $\Delta\boldsymbol{\sigma}$ and $\Delta\boldsymbol{\varepsilon}$ are the increments in the stress and strain tensors in a given time increment, respectively, and $\mathbf{E}_{t}$ is the relative strain tensor in the same time increment. As already described, the Jacobian is used in the equilibrium iterations for revising the

estimated displacements. It should also be noted that the Jacobian plays an important role in the rate of convergence of the solution to the global equilibrium equations, but has no effect on the accuracy of the solution. An analytical expression to compute the Jacobian was developed by Alharbi and Kalidindi (2015), and is expressed as

$$\boldsymbol{\mathcal{J}} = \frac{\partial \boldsymbol{\sigma}}{\partial \mathbf{E}_t} = \frac{\partial \boldsymbol{\sigma}'}{\partial \mathbf{D}'}\frac{\partial \mathbf{D}'}{\partial \mathbf{E}_t} + \mathbf{I} \otimes \frac{\partial p}{\partial \mathbf{E}_t} \ , \ \ \frac{\partial \boldsymbol{\sigma}'}{\partial \mathbf{D}'} = \left[\mathbb{I} + \frac{\partial \boldsymbol{\sigma}'}{\partial \mathbf{D}^p}\frac{\partial \mathbf{D}^*}{\partial \boldsymbol{\sigma}'}\right]^{-\mathbf{1}} \frac{\partial \boldsymbol{\sigma}'}{\partial \mathbf{D}^p} \tag{2.15}$$

where p denotes the pressure, and $\mathbf{I}$ and $\mathbb{I}$ are the second-rank and fourth-rank identity tensors, respectively. The central challenge in the use of Eq. (2.15) comes from the computation of $\frac{\partial \boldsymbol{\sigma}'}{\partial \mathbf{D}^p}$; simple analytical expressions have been provided by Alharbi and Kalidindi (2015) for the rest of the terms in Eq. (2.15). Using a chain-rule expansion for $\frac{\partial \boldsymbol{\sigma}'}{\partial \mathbf{D}^p}$ results in (Alharbi and Kalidindi, 2015; Zecevic et al., 2015b)

$$\frac{\partial \boldsymbol{\sigma}'}{\partial \mathbf{D}^p} = \left[\left(\frac{\partial \boldsymbol{\sigma}'}{\partial \dot{\varepsilon}}\Big|_{\theta,s,\mathrm{g}^\mathrm{D}} \ \frac{\partial \dot{\varepsilon}}{\partial \mathbf{D}^p}\right) + \left(\frac{\partial \boldsymbol{\sigma}'}{\partial \theta}\Big|_{\dot{\varepsilon},s,\mathrm{g}^\mathrm{D}} \ \frac{\partial \theta}{\partial \mathbf{D}^p}\right) + \left(\frac{\partial \boldsymbol{\sigma}'}{\partial \mathrm{g}^\mathrm{D}}\Big|_{\dot{\varepsilon},\theta,s} \ \frac{\partial \mathrm{g}^\mathrm{D}}{\partial \mathbf{D}^p}\right) + \left(\frac{\partial \boldsymbol{\sigma}'}{\partial s}\Big|_{\dot{\varepsilon},\theta,\mathrm{g}^\mathrm{D}} \ \frac{\partial s}{\partial \mathbf{D}^p}\right)\right] \tag{2.16}$$

where $\mathrm{g}^\mathrm{D} = (\varphi_1^\mathrm{D}, \Phi^\mathrm{D}, \varphi_2^\mathrm{D})$ denotes a set of three Bunge-Euler angles used to transform the deviatoric stress tensor from the principle frame of $\mathbf{D}^p$ to the sample frame. It should be noted that g^D is different from g^p (described in section 2.2) which denotes the crystal orientation with respect to principle frame of $\mathbf{D}^p$. Alharbi and Kalidindi (2015) have shown that the terms in Eq. (2.16) can be directly evaluated using the DFT representations introduced in section 2.2. The term $\frac{\partial \mathrm{g}^\mathrm{D}}{\partial \mathbf{D}^p}$ in Eq. (2.16) is responsible for creating some of the instability issues in Jacobian calculation and will be discussed in

more detail later. This term also incurs the most computational cost. The strategy used for evaluating this term leverages the spectral decomposition of $\mathbf{D}^p$ as

$$\mathbf{D}^p \, \mathbf{N}^{(i)} = \lambda^{(i)} \, \mathbf{N}^{(i)} \tag{2.17}$$

where $\mathbf{N}^{(i)}$ denote the eigenvector of $\mathbf{D}^p$ corresponding to the eigenvalue $\lambda^{(i)}$ (Alharbi and Kalidindi, 2015). The spectral decomposition also implies that

$$\mathbf{D}^p \, \mathbf{N}^{(i)} \cdot \mathbf{N}^{(j)} = 0 \qquad \text{for } i \neq j \tag{2.18}$$

It was demonstrated that SCPFEM framework can speed up the computational time by about 40 times compared to the conventional CPFEM simulations (Alharbi and Kalidindi, 2015). The demonstrated simulations generally included plane strain compression and simple shear deformations on a polycrystalline RVE considering one crystal at each integration point.

CHAPTER 3. GENERATION OF A NEW DFT DATABASE (SECOND GENERATION)

Although the first generation DFT database has been used successfully in various example applications of crystal plasticity computations (cf., Knezevic et al., 2008, 2009; Kalidindi et al., 2009; Alharbi et al., 2010; Knezevic and Savage, 2014; Alharbi and Kalidindi, 2015; Zecevic et al., 2015a, 2015b), it exhibited certain inaccuracies in the estimated values of the functions involved for certain new inputs. These inaccuracies have led to erroneous estimates of the anisotropic stress-strain responses for polycrystalline aggregates as well as in the estimations of the jacobians required for successful implementation of these databases in FE models. In this work, the origins of these inaccuracies were carefully tracked to certain biases introduced inadvertently in the design of the first generation DFT databases. In this work, these issues were addressed and much more accurate second generation DFT database was built. These improvements to the database approach are described next.

3.1 Biases in first generation DFT database

In the first generation DFT database generated and used in prior work (Knezevic et al., 2009; Alharbi and Kalidindi, 2015), the DFTs were generated for only five of the independent components of the deviatoric stress tensor, namely σ'_{11}, σ'_{22}, σ'_{12}, σ'_{13}, and σ'_{23}. The sixth stress component was computed using $\sigma'_{33} = -(\sigma'_{11} + \sigma'_{22})$; this ensures that the trace of the computed deviatoric stress tensor is zero. The arbitrary selection of two of the diagonal components from the full list of three components of the deviatoric

tensor introduced an unintended bias in the computation of the third component. This is because the use of only the dominant DFTs for new input values introduces an error in the computation of each term. However, when the computed values of two terms are used to compute the third term indirectly, the errors can add up to produce a significantly higher error in the third computed term. A detailed investigation was conducted to verify this hypothesis. The investigations have shown that the error in the computed values of σ'_{33} from the first generation DFT database was indeed significantly higher than the corresponding errors in the computation of the other components of the deviatoric stress tensor. More specifically, it was observed that the errors were higher for certain deformation modes such as uniaxial tension and equibiaxial tension. These observations have therefore confirmed the basic hypothesis. In the new DFT database, it was decided to establish the DFT representations shown in Eq. (2.10) separately for all six components of the deviatoric stress tensor, and a simple correction is to be made to the computed deviatoric stress tensor from the DFT database to ensure that it is traceless (described in more detail later).

For computing the value of deformation mode angle θ for any given $\mathbf{D}_0$ (see Eqs. (2.7) and (2.8)), one would first compute the set of eigen values (D_1, D_2, D_3) and then solve for θ that satisfies all of the requirements in Eq. (2.8). A second unintended bias was introduced into the original framework in the protocols related to the eigenvalues of $\mathbf{D}_0$. Some of the numerical instabilities found in the SCP-FLD and SCPFEM implementation were traced to lack of standardization in the assignment of $D_1, D_2, \text{and } D_3$ to the eigen values of $\mathbf{D}_0$. It should be noted that for a given $\mathbf{D}_0$, there are six distinct selections for the values of the set of variables (D_1, D_2, D_3). Each different

assignment will produce a different value of θ. It was further observed that the numerical instabilities in the SCPFEM implementation were particularly severe for the situation when two of the three eigen values of $\mathbf{D}_0$ were equal to each other. These issues arose mainly because the parameterization presented in Eqs. (2.7) and (2.8) has certain inherent symmetries. It is important to recognize that the relations for $D_1, D_2,$ and D_3 presented in Eq. (2.8) can be interchanged without losing any accuracy. It is also important to note that these symmetries would indeed be captured accurately in the DFT representations used in the original framework. In other words, although it was possible to identify six different but equally valid values of θ for a given $\mathbf{D}_0$, the DFT representations used in the original framework would produce the same values for all the functions involved for all six selections. Therefore, this bias did not affect directly the estimations of the function values from the DFT representations shown in Eqs. (2.9)-(2.11). However, computational instabilities were mainly noted in the computations of jacobians in the implementation of the databases in FEM simulations (i.e., SCPFEM framework (Alharbi and Kalidindi, 2015)). The instabilities were most severely noted for the situations when two of the eigen values of $\mathbf{D}_0$ were equal to each other. It is believed that this is because the computation of the jacobians needed evaluations of the function derivatives, which were derived analytically and evaluated when needed. The numerical values of the derivatives were observed to show significant variations with the different selections of the equivalent values of θ, and produce numerical instabilities in the iterations performed to satisfy global equilibrium in the SCPFEM framework.

3.2 New DFT database

Specific strategies were designed and implemented to address the biases identified above in the first generation DFT database, while also increasing the overall accuracy of the DFT database for various intended applications. A new spectral DFT database (second generation) was generated. In order to address the first bias described earlier, DFT representations shown in Eq. (2.10) were generated independently for all six components of the deviatoric stress (i.e., including σ'_{33}). An important consequence of this change is that the estimated $\boldsymbol{\sigma}'$ from the truncated DFT representations (this happens because we use only the dominant DFT terms for new estimations) is no longer traceless. It was noted that the error is relatively small, and could be easily corrected by subtracting the hydrostatic component of the estimated $\boldsymbol{\sigma}'$ from itself. This new strategy was found to produce significantly improved estimations of $\boldsymbol{\sigma}'$ from the DFT representations shown in Eq. (2.10).

The second bias described in the previous section was addressed by standardizing the assignment of the eigenvalues of $\mathbf{D}_0$ to the set $\{D_1, D_2, D_3\}$. In this work, this was accomplished by simply sorting the eigen values in a descending order, i.e., setting $D_1 \geq D_2 \geq D_3$. This standardization produces a unique value of θ for any selected $\mathbf{D}_0$. Figure 3.1 shows the plots of D_i implied in Eq. (2.8). It is seen from Figure 3.1 that the strategy identified above would consistently produce $\theta \in [0^\circ, 60^\circ]$. It is also seen from Figure 3.1 that $[0^\circ, 120^\circ)$ serves as a periodic domain for any function over θ, with mirror symmetry about $\theta = 60^\circ$. Figure 3.1 also identifies the locations of deformation modes of plane strain compression (PSC), uniaxial tension (UT) and equi-biaxial tension (EBT), after implementing the strategy described above. Table 3.1 shows the corresponding applied $\mathbf{D}_0$ for these three deformation modes. As a specific example, consider the solid

circles corresponding to PSC for which $\theta = 30^{\circ}$. The two other deformation modes identified in Figure 3.1 corresponding to $\theta = 60^{\circ}$ (corresponding UT) and $\theta = 0^{\circ}$ (corresponding to EBT) exhibit two equal eigen values. As noted earlier, these deformation modes generally produce significant challenges in the equilibrium iterations in the SCPFEM simulations.

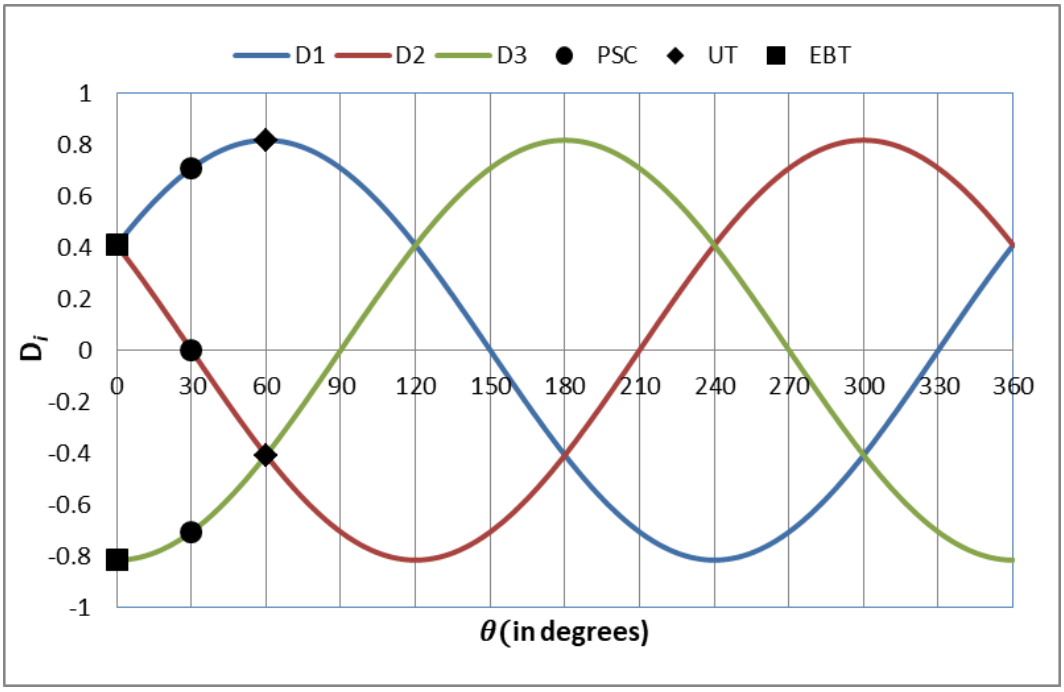

Figure 3.1: Variation of D_i with θ (as per equation (2.8)) with the locations for plane strain compression (PSC), uniaxial tension (UT) and equi-biaxial tension (EBT) identified.

Table 3.1: $\mathbf{D}_0$ for deformation modes of PSC, UT and EBT used in this work

Deformation mode (unit, traceless)	Plane strain compression (PSC)	Uniaxial tension (UT)	Equi-biaxial tension (EBT)
$\mathbf{D}_0$	$\frac{1}{\sqrt{2}}\begin{bmatrix}1 & 0 & 0\\ 0 & 0 & 0\\ 0 & 0 & -1\end{bmatrix}$	$\frac{\sqrt{2}}{\sqrt{3}}\begin{bmatrix}1 & 0 & 0\\ 0 & -0.5 & 0\\ 0 & 0 & -0.5\end{bmatrix}$	$\frac{1}{\sqrt{6}}\begin{bmatrix}1 & 0 & 0\\ 0 & 1 & 0\\ 0 & 0 & -2\end{bmatrix}$

In order to generate the DFT databases defined in Eqs. (2.9)-(2.11), we need to sample the corresponding functions (for the deviatoric stress components, plastic spin components, and total shear rate) on a uniform 4-D grid (defined by $(\varphi_1, \Phi, \varphi_2, \theta)$) in their periodic domains by performing a conventional CP model (described earlier in section 2.1) computation using previously established protocols (Kalidindi et al., 1992; Knezevic et al., 2009). The number of computations to be performed will depend on the resolution of the sampling grid. Although, finer grids will generally result in higher accuracy, they will also increase the (one-time) computational cost of generating the database. Furthermore, below a certain level of discretization, one would expect that there would be no information in the frequency spectrum of the function of the interest. Multiple trials have shown that the crystal plasticity spectral databases produced with the one-degree grid discretization provide excellent results. Note that this discretization level is significantly higher than the three-degree discretization used in the first generation DFT database (Knezevic et al., 2009; Alharbi and Kalidindi, 2015). Although this increases the computation cost of establishing the database, it should be remembered that the database only needs to be built once.

The periodic domain for the independent variables involved in the DFT representations shown in Eqs. (2.9)-(2.11) can be identified as $(\varphi_1 \epsilon\, [0,2\pi), \Phi \epsilon\, [0,2\pi), \varphi_2 \epsilon\, [0,2\pi), \theta\, \epsilon\, [0, 2\pi/3\,)$. Thus, a one-degree discretization in this 4-D space would require a large number of CP computations. Following the strategies described previously (Knezevic et al., 2009), it is possible to reduce the total number of required CP computations by taking advantage of the symmetry relations for cubic crystals (Adams et al., 2013) and the mirror symmetry evident within the periodic

domain of θ (see Figure 3.1). Therefore, CP computations (solving Eqs. (2.1)-(2.4)) are done only for orientations in FZ3 (three times the fundamental zone of orientations for cubic crystals (Kalidindi et al., 2009)); symmetry relations are used to assign the values of the functions for the remaining grid points. For a one-degree grid spacing, mid-point of the bin is chosen to be grid point. Therefore, CP computations were performed on one degree intervals over the space ($\varphi_1 \epsilon\, [0.5, 359.5], \Phi \epsilon\, [0.5,\ 89.5], \varphi_2 \epsilon\, [0.5, 89.5], \theta\, \epsilon\, [0.5, 59.5]$), resulting in a total 360 x 90 x 90 x 60 ≈ 2x10^8 solutions to Eqs. (2.1)-(2.4). The results of these computations were then used to populate the solutions over the full periodic domain of the input variables identified earlier.

Since all of these CP computations are completely unrelated to each other, this large set of computations was accomplished using parallel computing on clusters. Furthermore, for these computations, the slip hardening rate parameter, h_o, was set to zero (i.e., non-hardening), the initial slip resistance, s_o, was assigned as 100 MPa (this is an arbitrary choice that has no consequence because the stress values are suitably normalized by this factor before computing the DFTs in Eq. (2.10)), the reference value of the shearing rate, $\dot{\gamma}_o$, was taken as 0.001/sec (this is a fairly standard practice in CP computations), the rate-sensitivity parameter, m, was taken as 0.01 (reflects the measured values of rate-sensitivity for most metals at low homologous temperatures), and the norm of the imposed strain rate, $\dot{\varepsilon}$, was set to 0.001/sec. The strategies described above are designed to produce a highly re-usable DFT database that can be utilized to estimate most of the future CP solutions needed on fcc metals that deform plastically by slip on the twelve $\{111\}\langle 1\bar{1}0\rangle$ slip systems.

The first step in the generation of the DFT database is the execution of the complete set of $2x10^8$ CP computations described above. For each CP computation, one selects an input in the 4-D grid of the reduced space ($\varphi_1 \epsilon [0.5, 359.5], \Phi \epsilon [0.5, 89.5], \varphi_2 \epsilon [0.5, 89.5], \theta \epsilon [0.5, 59.5]$). One then defines the appropriate deformation mode using the selected θ (see Eqs. (2.7) and (2.8)) and solves Eqs. (2.1)-(2.4) using previously established computational procedures (Kalidindi et al., 1992; Knezevic et al., 2009). For each set of inputs in the 4-D grid, a total of ten solution values are collected into a suitable array. These solution values correspond to the functions to be captured in the DFT representations in Eqs. (2.9)-(2.11) and include three components of the plastic spin tensor, $\mathbf{W}^{\boldsymbol{p}}$, six components the deviatoric stress tensor, $\boldsymbol{\sigma}'$, and the total shear rate, $\sum_\alpha |\dot{\gamma}^\alpha|$. These values are then used to populate the full periodic input domain needed to perform the DFT operations correctly. Since the full periodic domain is sixteen times larger, this process entails identifying the fifteen other equivalent locations where each solution should be copied. This is accomplished by making use of the known symmetries in both the representation of the crystal orientations (Kalidindi et al., 2009; Adams et al., 2013) as well as the representation of the deformation mode using θ (see Figure 3.1). The first set are further broken into two subsets of relationships: (i) A total of eight relationships are used to identify equivalent grain orientations between FZ3 and the standard Euler space of orientations (Kalidindi et al., 2009). These can be summarized as equivalencies between $(\varphi_1, \Phi, \varphi_2)$, $(\varphi_1, \Phi, \varphi_2 + \pi/2)$, $(\varphi_1 + \pi, \pi - \Phi, \pi - \varphi_2)$, $(\varphi_1 + \pi, \pi - \Phi, \pi/2 - \varphi_2)$, $(\varphi_1 + \pi, \pi - \Phi, 2\pi - \varphi_2)$, $(\varphi_1, \Phi, \varphi_2 + 3\pi/2)$, $(\varphi_1, \Phi, \varphi_2 + \pi)$, and $(\varphi_1 + \pi, \pi - \Phi, 3\pi/2 - \varphi_2)$. (ii) The equivalence of $(\varphi_1, \Phi, \varphi_2)$ and $(\varphi_1 + \pi, 2\pi - \Phi, \varphi_2 + \pi)$ arising from the definition of Euler angles. The next set of

equivalencies come from the mirror symmetry in the definition of the θ-space (see Figure 3.1). Application of symmetries results in ten arrays, each of size 360 x 360 x 360 x 120. The DFTs for all ten variables are computed using *fftn* function in Matlab (MATLAB, 2018). At the end of this computation, one would have ten 4-D arrays of complex-valued DFTs. The computation of this full set of DFTs required ~70 CPU hours on a 2 GHz clock speed machine with a memory (RAM) of ~128 GB. It should be noted that the storage of the complete set of the DFTs obtained would require substantial storage resources, estimated to be ~ 40 GB. However, the strategy is to store only the dominant DFTs (i.e., those whose magnitudes are the largest). Furthermore, advantage of the fact is taken that about half of the DFTs are complex conjugates of the other half for all real-valued functions. As a consequence, only half of the dominant DFTs need to be stored, and the complex conjugates can be easily reconstructed when needed (this strategy was utilized in the first generation database by Knezevic et al., 2009). Employing these strategies dramatically reduces the storage resources needed for using the database approach. As an example, the reduced database for one output variable containing a vector of 50000 DFTs requires only ~ 700 KB storage space. It will be seen later that one often needs to store a much smaller database for most practical applications.

Suitable interpolation techniques are needed for obtaining crystal plasticity results for any new set of inputs $(\varphi_1, \Phi, \varphi_2, \theta)$. In the first generation framework (Knezevic et al., 2009; Alharbi and Kalidindi, 2015) a spectral interpolation technique was used. However, the work of Zecevic et al. (2015a) has demonstrated the benefits of a trigonometric interpolation scheme. The central advantage of this scheme is that the main functions of crystal plasticity solutions can be recovered as continuous functions of

orientation and deformation mode from the spectral DFT database using Inverse Discrete Fourier Transform (IDFTs) representations. These are expressed as

$$\mathbf{W}^{p}(g^{p},\theta)=\dot{\varepsilon}\frac{1}{N_{\varphi_1}N_{\varphi}N_{\varphi_2}N_{\theta}}\left[\sum_{k=-\frac{N_{\varphi_1}}{2}+1}^{\frac{N_{\varphi_1}}{2}}\sum_{l=-\frac{N_{\varphi}}{2}+1}^{\frac{N_{\varphi}}{2}}\sum_{m=-\frac{N_{\varphi_2}}{2}+1}^{\frac{N_{\varphi_2}}{2}}\sum_{n=-\frac{N_{\theta}}{2}+1}^{\frac{N_{\theta}}{2}}\mathbf{B}_{klmn}\,e^{\frac{2\pi ik\varphi_1}{L_{\varphi_1}}}e^{\frac{2\pi il\varphi}{L_{\varphi}}}e^{\frac{2\pi im\varphi_2}{L_{\varphi_2}}}e^{\frac{2\pi in\theta}{L_{\theta}}}\right] \tag{3.1}$$

$$\boldsymbol{\sigma}'(g^{p},\theta)=s\dot{\varepsilon}^{m}\frac{1}{N_{\varphi_1}N_{\varphi}N_{\varphi_2}N_{\theta}}\left[\sum_{k=-\frac{N_{\varphi_1}}{2}+1}^{\frac{N_{\varphi_1}}{2}}\sum_{l=-\frac{N_{\varphi}}{2}+1}^{\frac{N_{\varphi}}{2}}\sum_{m=-\frac{N_{\varphi_2}}{2}+1}^{\frac{N_{\varphi_2}}{2}}\sum_{n=-\frac{N_{\theta}}{2}+1}^{\frac{N_{\theta}}{2}}\mathbf{C}_{klmn}\,e^{\frac{2\pi ik\varphi_1}{L_{\varphi_1}}}e^{\frac{2\pi il\varphi}{L_{\varphi}}}e^{\frac{2\pi im\varphi_2}{L_{\varphi_2}}}e^{\frac{2\pi in\theta}{L_{\theta}}}\right] \tag{3.2}$$

$$\sum_{\alpha}|\dot{\gamma}^{\alpha}|\,(g^{p},\theta)=\dot{\varepsilon}\frac{1}{N_{\varphi_1}N_{\varphi}N_{\varphi_2}N_{\theta}}\left[\sum_{k=-\frac{N_{\varphi_1}}{2}+1}^{\frac{N_{\varphi_1}}{2}}\sum_{l=-\frac{N_{\varphi}}{2}+1}^{\frac{N_{\varphi}}{2}}\sum_{m=-\frac{N_{\varphi_2}}{2}+1}^{\frac{N_{\varphi_2}}{2}}\sum_{n=-\frac{N_{\theta}}{2}+1}^{\frac{N_{\theta}}{2}}\mathrm{G}_{klmn}\,e^{\frac{2\pi ik\varphi_1}{L_{\varphi_1}}}e^{\frac{2\pi il\varphi}{L_{\varphi}}}e^{\frac{2\pi im\varphi_2}{L_{\varphi_2}}}e^{\frac{2\pi in\theta}{L_{\theta}}}\right] \tag{3.3}$$

For the one-degree grid used in this work, $N_{\varphi_1}=N_{\varphi}=N_{\varphi_2}=360$, $N_{\theta}=120$, $L_{\varphi_1}=L_{\varphi}=L_{\varphi_2}=360$, and $L_{\theta}=120$. As discussed earlier, in employing Eqs. (3.1)-(3.3), the strategy will be to utilize only the dominant DFTs among the full set of ($\mathbf{B}_{klmn}$, $\mathbf{C}_{klmn}$, G_{klmn}). In other words, the contributions from the non-dominant DFTs are ignored. Figure 3.2 demonstrates the plots of magnitude of dominant DFTs after they are sorted in descending order of magnitude for (a) $\sigma'_{11}(g^{p},\theta)$, (b) $\sum_{\alpha}|\dot{\gamma}^{\alpha}|\,(g^{p},\theta)$, and (c) $\mathrm{W}_{12}^{p}(g^{p},\theta)$. It can be observed that magnitude of DFTs decay exponentially after the first few hundreds of DFTs, and as a result the non-dominant DFTs do not contribute much to the magnitude of functions of interest. Omitting these non-dominant DFTs would result in major computational savings with only minimal loss in accuracy. For the second generation DFT database built in this work, based on multiple trials with different orientations and deformation modes, it was concluded that the use of 500 dominant DFTs

for $\mathbf{C}_{klmn}$ and G_{klmn}, and 2000 dominant DFTs for $\mathbf{B}_{klmn}$ produced sufficiently accurate estimations of the functions identified in Eqs. (3.1)-(3.3) for all inputs in their 4-D input domain. It should be noted that the use of the finer one degree grid in the second generation DFT database built here produced 27 times more DFTs (in the full set of DFTs) compared to the first generation database. However, the number of dominant DFTs selected from the second generation database presented here is actually slightly less than the number of dominant DFTs selected for the first generation DFT database. It will be shown later that the smaller number of dominant DFTs selected for the second generation database actually produce significantly more accurate estimations of the function values compared to the first generation database. This is largely because of the improvements made to the protocols (as described earlier), and confirms that the spectral representations obtained using these protocols are quite stable. Furthermore, it should be recognized that the number of dominant DFTs selected here represents a compromise between computational time and accuracy.

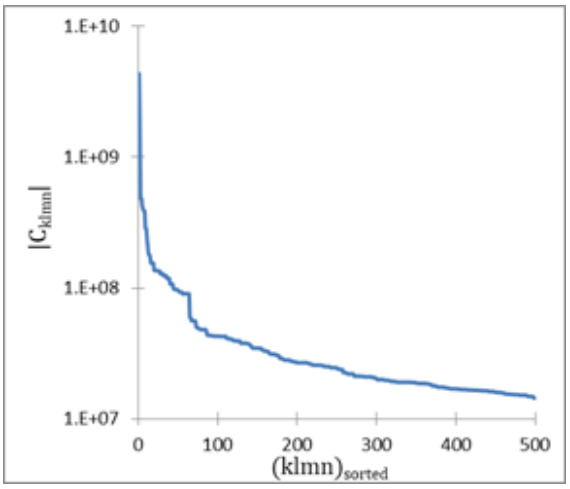

(a)

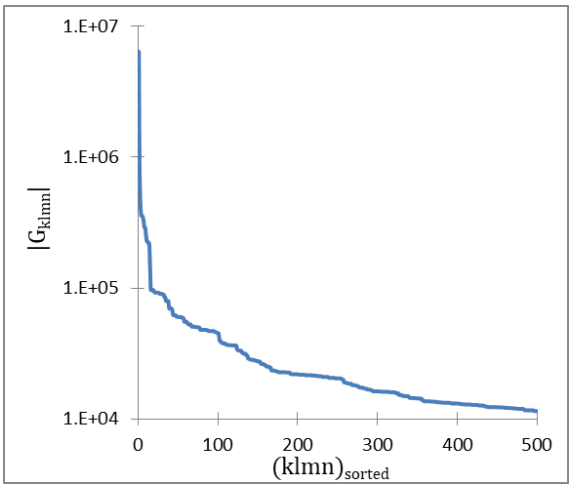

(b)

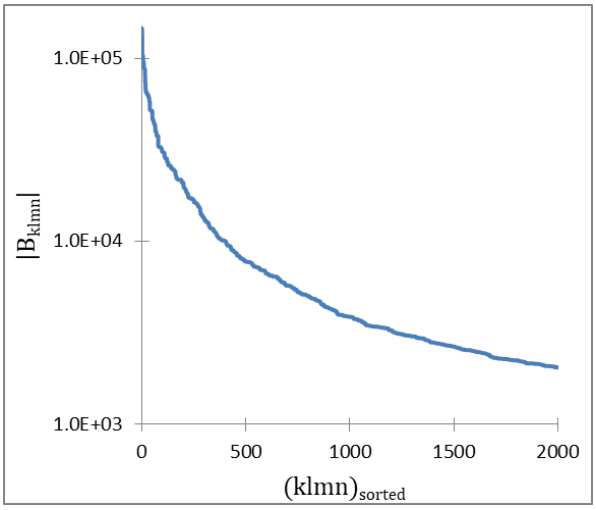

(c)

Figure 3.2: Variation of the magnitude of the dominant DFTs (after sorting the full set of DFTs in the descending order of magnitude) for (a) $\sigma'_{11}(g^p, \theta)$, (b) $\sum_\alpha |\dot{\gamma}^\alpha| (g^p, \theta)$, and (c) $W_{12}^p(g^p, \theta)$.

The predicted stress-strain responses and final textures predicted using the first and second generation DFT databases are compared against the direct rigid-viscoplastic CP predictions obtained using a Taylor-type model (Kalidindi et al., 1992) for EBT, UT and PSC (see Table 3.1) in Figure 3.3. These simulations utilized the hardening parameters correspond to oxygen-free high conductivity (OFHC) copper: h_0 = 180 MPa, s_s = 148 MPa, a = 2.25, s_0 = 16 MPa and m = 0.01 (Kalidindi et al., 1992). The polycrystal was assumed to comprise of 1000 equal-volume fcc single crystals exhibiting a random initial texture. Clearly, the predictions of the stress-strain evolutions shown in Figure 3.3 (a), (d) and (g) for EBT, UT and PSC, respectively, demonstrate the improved accuracy of the second generation DFT database compared to the first generation DFT

database. Deformed textures shown as pole figures predicted by the direct CP simulations are compared against the predictions obtained using the second generation DFT database developed in work. These comparisons are presented in Figure 3.3(b) and (c) for EBT, Figure 3.3(e) and (f) for UT, and Figure 3.3(h) and (i) for PSC. The predictions from the DFT database only show a small loss of accuracy. However, as with the first generation DFT database, the computational savings from the DFT database approach are roughly two orders of magnitude when compared to the computational cost of the direct CP simulations. The main advance with the second generation database presented here is that we are still maintaining the same computational savings as the first generation DFT database, but are producing significantly more accurate estimations for CP computations.

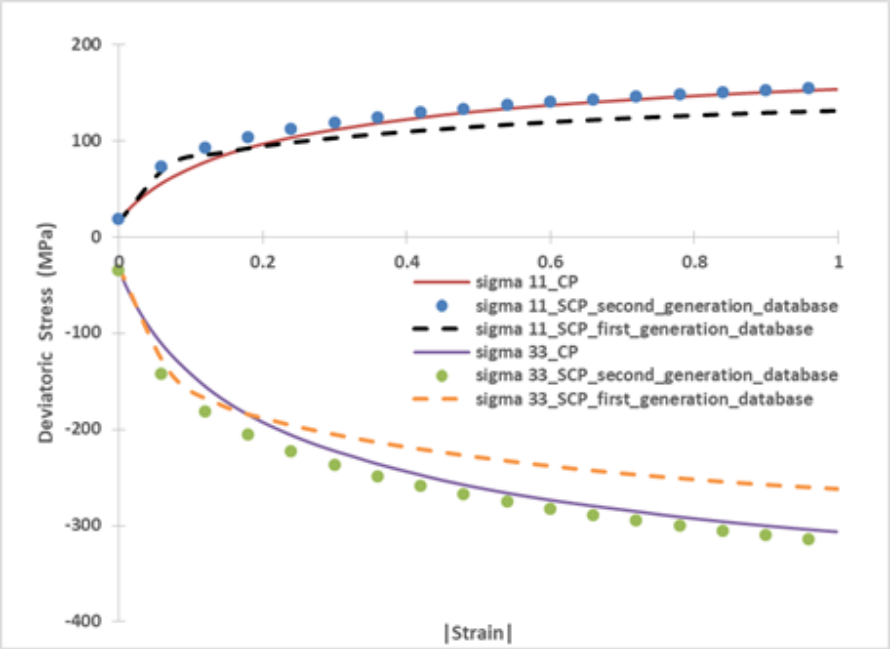

(a)

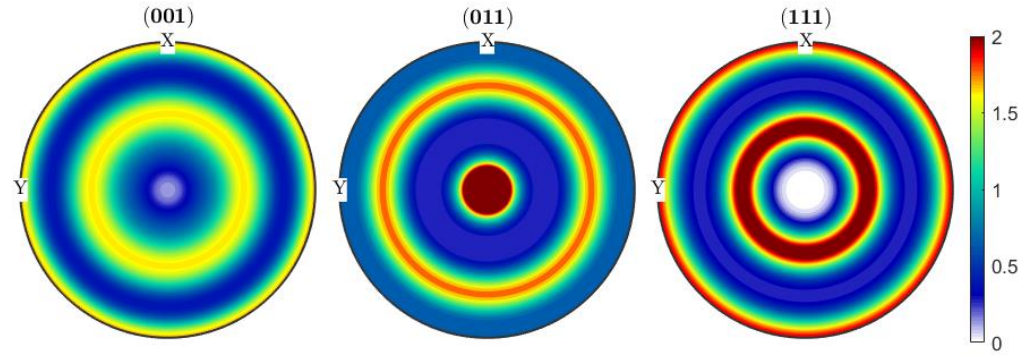
(001)
(011)
(111)
X
Y
2
1.5
1
0.5
0

(b)

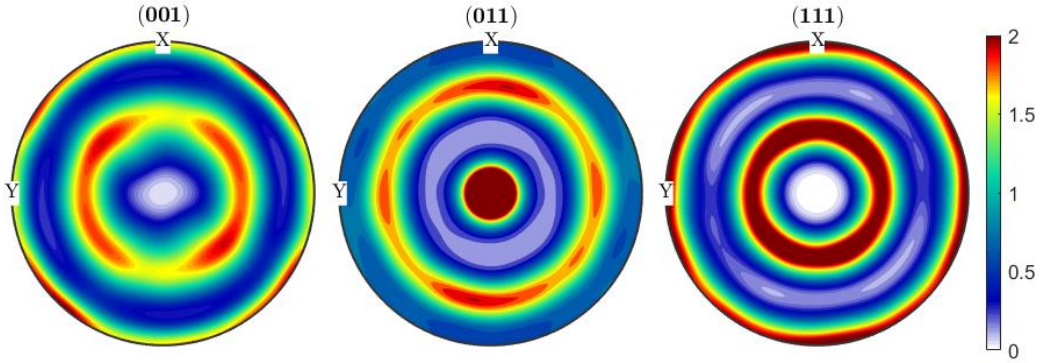
(001)
(011)
(111)
X
Y
2
1.5
1
0.5
0

(c)

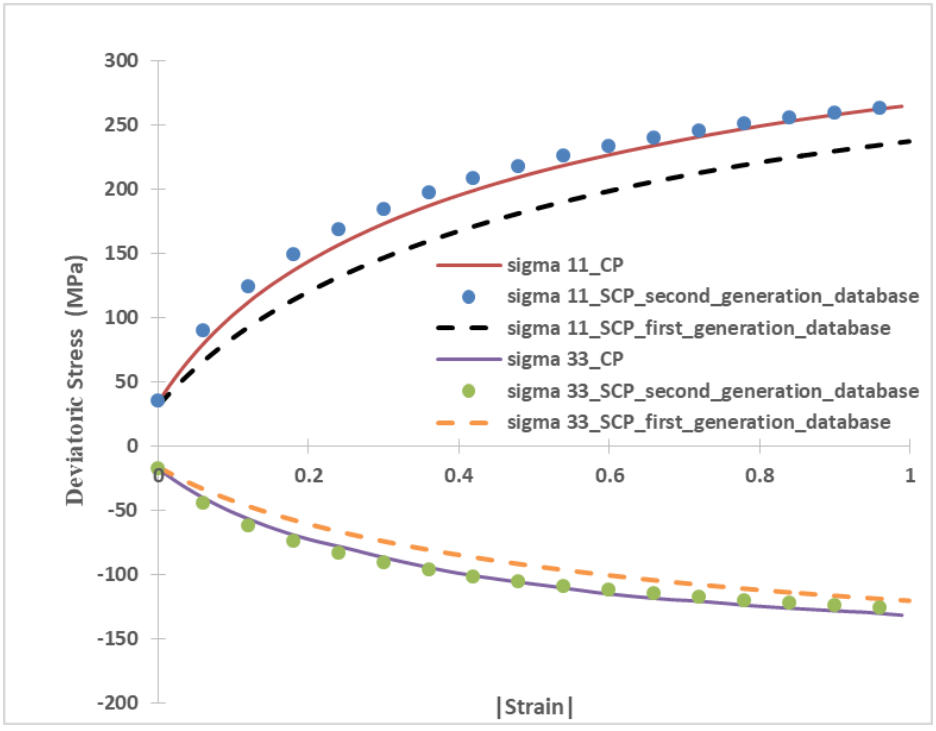
Deviatoric Stress (MPa)
|Strain|
300
250
200
150
100
50
0
-50
-100
-150
-200
0
0.2
0.4
0.6
0.8
1
sigma 11_CP
sigma 11_SCP_second_generation_database
sigma 11_SCP_first_generation_database
sigma 33_CP
sigma 33_SCP_second_generation_database
sigma 33_SCP_first_generation_database

(d)

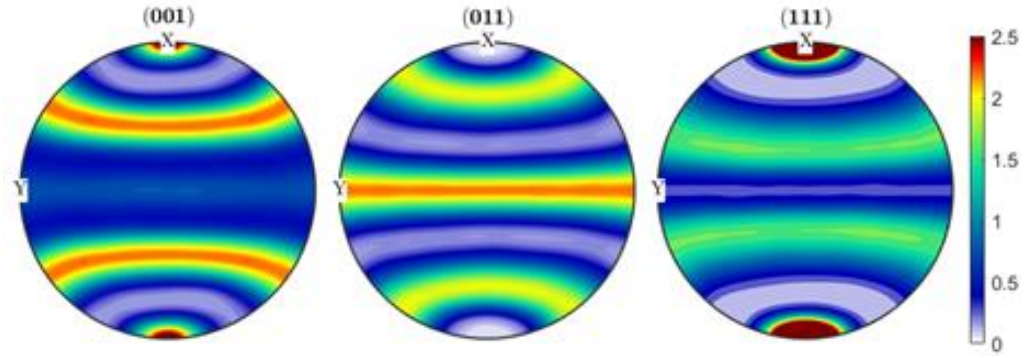
(001)
(011)
(111)
X
Y
2.5
2
1.5
1
0.5
0

(e)

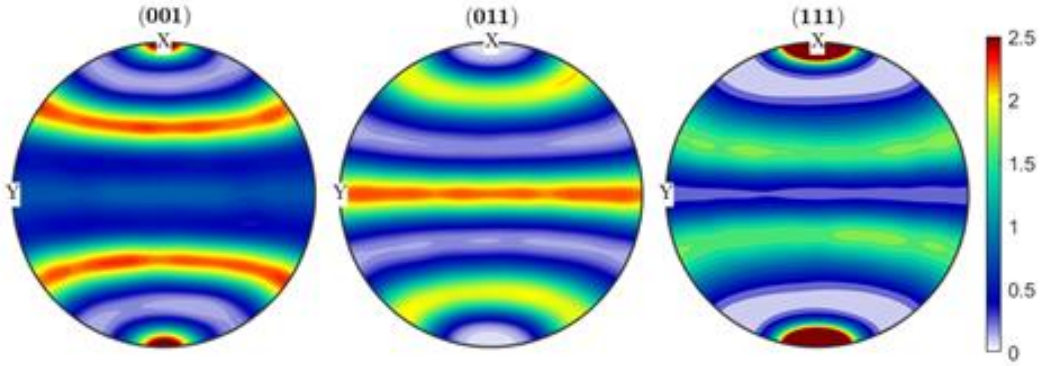
(001)
(011)
(111)
X
Y
2.5
2
1.5
1
0.5
0

(f)

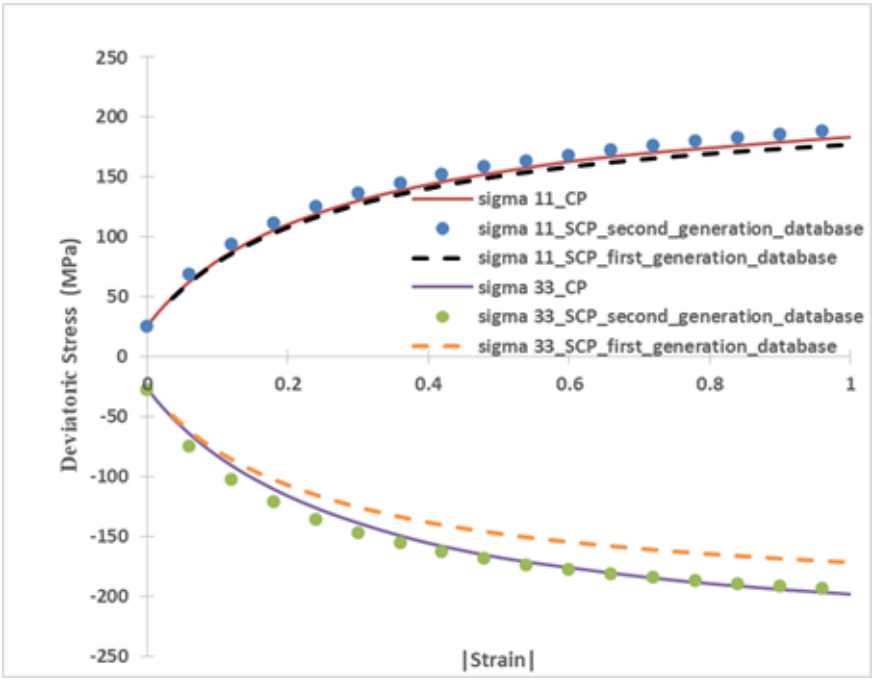
Deviatoric Stress (MPa)
|Strain|
250
200
150
100
50
0
-50
-100
-150
-200
-250
0
0.2
0.4
0.6
0.8
1
sigma 11_CP
sigma 11_SCP_second_generation_database
sigma 11_SCP_first_generation_database
sigma 33_CP
sigma 33_SCP_second_generation_database
sigma 33_SCP_first_generation_database

(g)

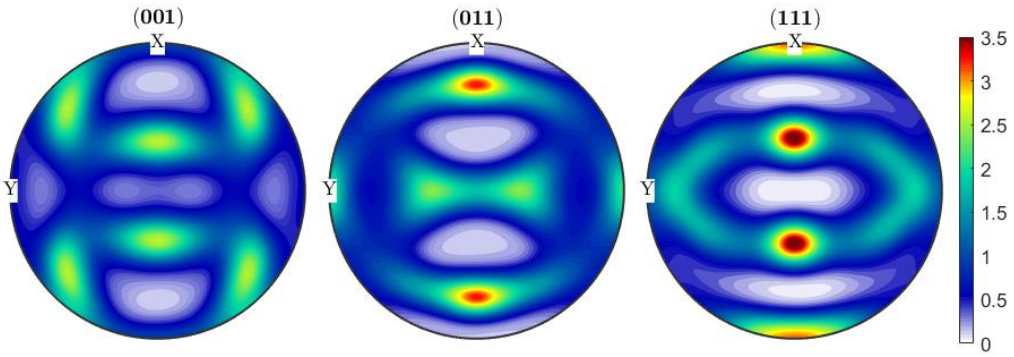

(h)

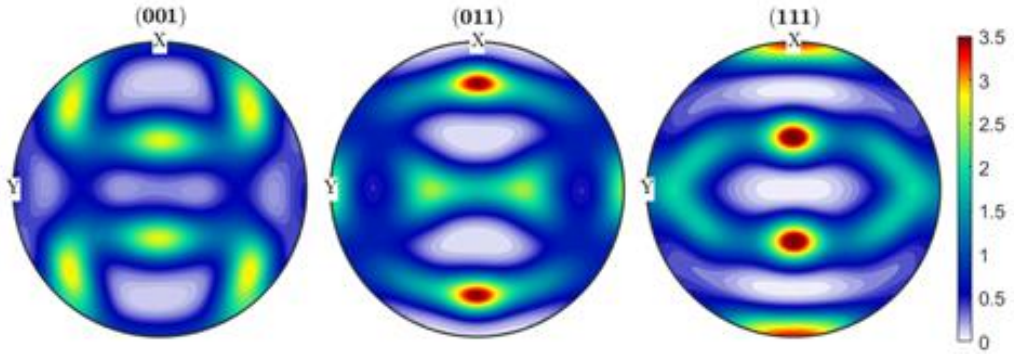

(i)

Figure 3.3: Comparison of CP predictions of stress-strain responses and final textures from the first and second generation DFT databases against the corresponding predictions from conventional CP Taylor-type models for EBT ((a)-(c)), UT ((d)-(f)) and PSC ((g)-(i)) simulation of OFHC Copper. (a), (d), (g) show comparisons for two different components of deviatoric stress vs. strain curves, (b), (e), (h) show pole figures of deformed texture from the conventional CP computations, and (c), (f), (i) show pole figures of deformed texture obtained using the second generation DFT database developed in this work.

CHAPTER 4. CRITICAL EVALUATION OF NEW SPECTRAL DFT DATABASE BY APPLICATION TO CRYSTAL PLASTICITY BASED FORMING LIMIT DIAGRAM PREDICTIONS

4.1 Introduction

Reliable prediction of the onset of localized necking in thin metal sheets represents a challenging task in the design and manufacturing of sheet metal structural components. During biaxial stretching of sheet metals, the deformation evolves homogeneously at the beginning of the loading. This homogeneous deformation stage is generally followed by diffuse necking, which is characterized by a progressive strain concentration under a smoothly decreasing load. Then, the load abruptly drops with the development of localized necking, which corresponds to the ultimate deformation state that a stretched metal sheet can undergo before failure. For the prediction of localized necking, the well-known forming limit diagram (FLD) concept is most commonly used. This concept was initially introduced by Keeler and Backofen (1963). Given that the experimental characterization of FLD has proven to be both difficult and expensive, considerable effort has been expended in prior literature (Considère, 1885; Swift, 1952; Hill, 1952; Marciniak and Kuczynski, 1967; Hutchinson and Neale, 1978b) to develop accurate theoretical and/or numerical tools capable of predicting them. Such approaches require the selection of a suitable constitutive framework, for the description of the material state evolution, together with an instability criterion, for the prediction of the onset of plastic flow localization. These are summarized below:

4.1.1 Localization criteria

Various analytical as well as numerical criteria have been developed in the literature to predict the onset of plastic strain localization in metals and alloys. These include the imperfection method, initially proposed by Marciniak and Kuczynski (Marciniak and Kuczynski, 1967) and subsequently improved by Hutchinson and Neale (Hutchinson and Neale, 1978b), the bifurcation theory developed by Rice and co-workers (Rudnicki and Rice, 1975; Stören and Rice, 1975; Rice, 1976) and the linear perturbation approach (Molinari and Clifton, 1987; Dudzinski and Molinari, 1991). The imperfection approach, which has been extensively used in the literature, is usually referred to as the M–K analysis. It assumes the preexistence of an initial imperfection, which can be of material type (plastic properties) or of geometric nature, in the form of a narrow band across the sheet thickness. This imperfection affects the plastic flow and thus influences the development of localized necking. In the course of loading, the plastic deformation concentrates more and more in the band, ultimately leading to localized thinning in this weakened zone of the sheet. Thanks to its pragmatic character and its extreme flexibility, the initial geometric imperfection approach is widely applied in current literature. This approach is also used here.

4.1.2 Constitutive description

The important role of the material constitutive behavior in the FLD prediction has already been established in prior literature. Accordingly, a wide range of phenomenological constitutive models have been coupled with several localization criteria to investigate the effect on the predicted FLDs of various mechanical features,

such as plastic anisotropy (Neale and Chater, 1980; Cao et al., 2000; Kuroda and Tvergaard, 2000; Wu et al., 2004; Zhang and Wang, 2012), strain-rate sensitivity (Ghosh, 1977; Hutchinson and Neale, 1978c; Neale and Chater, 1980; Khan and Baig, 2011; Manopulo et al., 2015), temperature (Khan and Baig, 2011; Manopulo et al., 2015) and damage-induced softening (Haddag et al., 2009; Abed-Meraim et al., 2014; Mansouri et al., 2014). However, a major shortcoming in the phenomenological constitutive models is their inability to consider accurately many of the salient microstructural aspects of the material behavior, such as crystallographic texture (Hosford and Caddell, 1993; Raabe et al., 2005). These limitations represent the main motivation behind the use of crystal plasticity models for the FLD predictions. Recently, several multiscale models using crystal plasticity constitutive descriptions have been coupled with the M–K analysis in order to predict localized necking and the associated FLDs. It should be noted that the constitutive equations at the single crystal scale can be classified into two main families: rate-dependent (cf. Wu et al., 1997, 1998, 2004; Boudeau et al., 1998; McGinty and McDowell, 2004; Inal et al., 2005; Neil and Agnew, 2009; Signorelli et al., 2009; Lévesque et al., 2010; Serenelli et al., 2011; Wang et al., 2011; Kim et al., 2013; Schwindt et al., 2015) and rate-independent approaches (cf. Knockaert et al., 2002; Yoshida and Kuroda, 2012; Akpama et al., 2017). Elasticity may be considered or disregarded in both approaches. For the work in this chapter, a rigid-viscoplastic framework was adopted to model the mechanical behavior at the single crystal scale. Elasticity is ignored in the constitutive modeling because strain localization occurs at relatively large strains. Furthermore, the deformation follows monotonic strain paths (without elastic unloading) prior to localized necking. Also, in this contribution, attention

has been restricted to face-centered cubic (FCC) crystals. The overall mechanical behavior of the polycrystalline aggregate was computed using the Taylor-type scale-transition scheme (Taylor, 1938). This particular approach has been shown to provide good predictions for medium to high stacking fault energy cubic materials (Asaro and Needleman, 1985; Mathur and Dawson, 1989; Bronkhorst et al., 1992). As explained above, a major advantage of this micromechanical modeling approach compared to the phenomenological one lies in its capability of naturally correlating the microstructure of the polycrystalline metal alloys with their formability. Despite this important benefit, the numerical prediction of FLDs for rigid-viscoplastic materials using the multiscale approach has not been often undertaken for polycrystalline aggregates composed of a large number of single crystals (one typically needs a few thousand single crystals to faithfully represent the polycrystalline aggregate of interest). The main factor limiting the application of the crystal plasticity models in predicting FLDs can be attributed to the considerable computational cost involved. Even when the constitutive equations are developed and implemented efficiently, the time integration of the highly nonlinear single crystal model generally demands high computational resources. Thus, the spectral DFT database approach discussed in section 2.2 is successfully used to speed up the conventional crystal plasticity computations for this application. This chapter discusses the first application of the DFT spectral database strategy to predict localized necking and the associated FLDs of thin metal sheets, represented as spectral crystal plasticity forming limit diagram (SCP-FLD). The new DFT database (second generation) described in chapter 3 is used in this work to speed up FLD predictions which will be discussed in this chapter. This new tool is presented and validated in this work by comparing the

predicted SCP-FLDs with the predictions from conventional methods, referred to as CP-FLD (e.g., Wu et al. 1997, 1998, 2004). It was demonstrated that the strategy proposed here leads to major savings of computational cost (96% reduction in the computational cost for FLD predictions) and these results along with many of the details presented in this chapter were published recently (Gupta et al., 2018).

The rest of the details in this chapter will be presented in the following major parts: theoretical framework, which is the basis of the developed numerical tool, is presented in section 4.2. Details of the rigid-viscoplastic crystal plasticity constitutive framework are first summarized followed by the equations governing the M–K approach. The numerical aspects, related to the equations developed in section 4.2, are detailed in section 4.3. The conventional method and the DFT approach (discussed in section 2.2 and chapter 3), required to solve the constitutive equations at the single crystal scale, are summarized. The set of equations governing the M–K approach are formulated as a nonlinear mathematical system and solved using the Newton–Raphson iterative scheme and this is detailed in section 4.3. Comparisons of the predicted FLDs from the new tool (based on the DFT approach) and the conventional approach are presented and discussed in section 4.4 and the conclusions of this chapter are discussed in section 4.5.

4.2 Theoretical framework

4.2.1 Crystal plasticity framework for FLD predictions

The mechanical behavior of the sheet is assumed to be described by a rigid-viscoplastic model. Furthermore, the plastic deformation is assumed to be only due to the slip on the crystallographic slip systems. Rigid-viscoplastic crystal plasticity framework

has been briefly described in section 2.1 and here some more details are given specifically related to using this framework for FLD prediction and corresponding formulation has been described which leads to convenient and computationally efficient integration of this framework for FLD prediction. Some equations are reiterated from section 2.1 for the sake of completeness and using the notations described in this chapter which will be used in subsequent equations for numerical aspects related to M-K approach. The velocity gradient, **L**, at the single crystal scale can be expressed as

$$\mathbf{L} = \mathbf{W}^{*} + \mathbf{L}^{\mathrm{P}} \quad ; \quad \mathbf{L}^{\mathrm{P}} = \sum_{\alpha=1}^{N_s} \dot{\gamma}^{\alpha}\, \vec{\mathbf{m}}^{\alpha} \otimes \vec{\mathbf{n}}^{\alpha} \tag{4.1}$$

where $\mathbf{W}^{*}$ is the lattice spin tensor, $\mathbf{L}^{\mathrm{P}}$ is the plastic velocity gradient tensor, $\dot{\gamma}^{\alpha}$ is the slip rate on the crystallographic system α, N_s is the total number of slip systems (equal to 12 for the FCC single crystals), and $\vec{\mathbf{n}}^{\alpha}$ and $\vec{\mathbf{m}}^{\alpha}$ are unit vectors that define respectively the normal to the slip plane and the slip direction for the slip system α in the current configuration. The slip direction $\vec{\mathbf{m}}^{\alpha}$ and the normal to the slip plane $\vec{\mathbf{n}}^{\alpha}$ are related to their counterparts $\vec{\mathbf{m}}_0^{\alpha}$ and $\vec{\mathbf{n}}_0^{\alpha}$, expressed in the isoclinic relaxed configuration by $\vec{\mathbf{m}}^{\alpha} = \mathbf{R}.\vec{\mathbf{m}}_0^{\alpha}$ and $\vec{\mathbf{n}}^{\alpha} = \mathbf{R}.\vec{\mathbf{n}}_0^{\alpha}$ where $\mathbf{R}$ is the lattice rotation tensor. Vectors $\vec{\mathbf{m}}_0^{\alpha}$ and $\vec{\mathbf{n}}_0^{\alpha}$ are assumed to be constant in the isoclinic configuration and are enumerated in Table 4.1.

Table 4.1: The numbering of the slip systems of an FCC single crystal

α	1	2	3	4	5	6
$\sqrt{2}\vec{\mathbf{m}}_0^\alpha$	$[1\,\bar{1}\,0]$	$[1\,0\,\bar{1}]$	$[0\,1\,\bar{1}]$	$[1\,0\,1]$	$[1\,\bar{1}\,0]$	$[0\,1\,1]$
$\sqrt{3}\vec{\mathbf{n}}_0^\alpha$	$(1\,1\,1)$	$(1\,1\,1)$	$(1\,1\,1)$	$(1\,1\,\bar{1})$	$(1\,1\,\bar{1})$	$(1\,1\,\bar{1})$
α	7	8	9	10	11	12
$\sqrt{2}\vec{\mathbf{m}}_0^\alpha$	$[1\,0\,\bar{1}]$	$[0\,1\,1]$	$[1\,1\,0]$	$[0\,1\,\bar{1}]$	$[1\,1\,0]$	$[1\,0\,1]$
$\sqrt{3}\vec{\mathbf{n}}_0^\alpha$	$(1\,\bar{1}\,1)$	$(1\,\bar{1}\,1)$	$(1\,\bar{1}\,1)$	$(\bar{1}\,1\,1)$	$(\bar{1}\,1\,1)$	$(\bar{1}\,1\,1)$

The evolution of the slip rate $\dot{\gamma}^\alpha$ is defined by a power law as follows:

$$\forall \alpha = 1, \dots, N_s : \ \dot{\gamma}^\alpha = \dot{\gamma}_0 \left|\frac{\tau^\alpha}{s^\alpha}\right|^{\frac{1}{m}} \operatorname{sgn}(\tau^\alpha) \ ; \ \tau^\alpha = \mathbf{S}\colon \mathbf{P}^{\boldsymbol{\alpha}} \tag{4.2}$$

where $\mathbf{S}$ (represented using $\boldsymbol{\sigma}'$ in other chapters) is used to denote the deviatoric part of the Cauchy stress tensor $\boldsymbol{\sigma}$ in this chapter for ease of notation in further equations that follows, while τ^α, s^α and $\mathbf{P}^{\boldsymbol{\alpha}}$ are the resolved shear stress, the slip resistance, and the symmetric part of the Schmid tensor $\vec{\mathbf{m}}^\alpha \otimes \vec{\mathbf{n}}^\alpha$, respectively, associated with slip system α. $\dot{\gamma}_0$ and m represent the reference value of the slip rates and the strain-rate sensitivity parameter, respectively.

In order to use a vector notation, which is more suitable for an efficient numerical implementation, τ^{α} can be expressed as (equivalent to Eq. (4.2) and noting that $\mathbf{S}$ and $\mathbf{P}^{\boldsymbol{\alpha}}$ are both traceless)

$$\forall \alpha = 1, \dots, N_s : \tau^{\alpha} = \mathbf{S}_{\mathrm{v}}.\widetilde{\mathbf{P}}_{\mathrm{v}}^{\alpha} \tag{4.3}$$

where $\mathbf{S}_{\mathrm{v}}$ denotes the vector storage of tensor $\mathbf{S}$ as $\{S_{11}, S_{22}, S_{12}, S_{23}, S_{13}\}$, while $\widetilde{\mathbf{P}}_{\mathrm{v}}^{\alpha}$ is obtained from the components of $\mathbf{P}^{\boldsymbol{\alpha}}$ as follows:

$$\forall \alpha = 1, \dots, N_s : \widetilde{\mathbf{P}}_{\mathrm{v}}^{\alpha} = \{2P_{11}^{\alpha} + P_{22}^{\alpha}, P_{11}^{\alpha} + 2P_{22}^{\alpha}, 2P_{12}^{\alpha}, 2P_{23}^{\alpha}, 2P_{13}^{\alpha}\} \tag{4.4}$$

The combination of Eqs. (4.1) and (4.2) allows us to obtain the following relation between the strain rate tensor $\mathbf{D}$ (the symmetric part of $\mathbf{L}$) and tensor $\mathbf{S}$:

$$\mathbf{D} = \dot{\gamma}_0 \sum_{\alpha=1}^{N_s} \left| \frac{\mathbf{S}:\mathbf{P}^{\boldsymbol{\alpha}}}{s^{\alpha}} \right|^{\frac{1}{m}} \mathrm{sgn}(\mathbf{S}:\mathbf{P}^{\boldsymbol{\alpha}}) \mathbf{P}^{\boldsymbol{\alpha}} \tag{4.5}$$

which is equivalent to

$$\mathbf{D}_{\mathrm{v}} = \dot{\gamma}_0 \sum_{\alpha=1}^{N_s} \left| \frac{\mathbf{S}_{\mathrm{v}}.\widetilde{\mathbf{P}}_{\mathrm{v}}^{\alpha}}{s^{\alpha}} \right|^{\frac{1}{m}} \mathrm{sgn}(\mathbf{S}_{\mathrm{v}}.\widetilde{\mathbf{P}}_{\mathrm{v}}^{\alpha}) \mathbf{P}_{\mathrm{v}}^{\alpha} \tag{4.6}$$

From Eq. (4.6), a condensed matrix (5x5 matrix) form, $\mathbf{M}$, for the microscopic tangent compliance can be defined as

$$\mathbf{M} = \frac{\partial \mathbf{D}_{\mathrm{v}}}{\partial \mathbf{S}_{\mathrm{v}}} = \frac{\dot{\gamma}_0}{m} \sum_{\alpha=1}^{N_s} \frac{\mathbf{P}_{\mathrm{v}}^{\alpha} \otimes \widetilde{\mathbf{P}}_{\mathrm{v}}^{\alpha}}{s^{\alpha}} \left| \frac{\mathbf{S}_{\mathrm{v}}.\widetilde{\mathbf{P}}_{\mathrm{v}}^{\alpha}}{s^{\alpha}} \right|^{\frac{1-m}{m}} \tag{4.7}$$

Matrix $\mathbf{M}$ is used for CP-FLD instead of the traditional fourth-order tensor form of the tangent compliance. This choice greatly improves the computational efficiency of the

simulations. The lattice spin tensor $\mathbf{W}^*$ and the related lattice rotation tensor $\mathbf{R}$ are defined as

$$\mathbf{W}^* = \dot{\mathbf{R}}\mathbf{R}^{\mathrm{T}} = \mathbf{W} - \mathbf{W}^{\mathrm{p}} \; ; \;\; \mathbf{W}^{\mathrm{p}} = \sum_{\alpha=1}^{N_s} \dot{\gamma}^{\alpha} \, \mathbf{A}^{\alpha} \tag{4.8}$$

where $\mathbf{W}$ is the applied spin tensor (the skew-symmetric part of $\mathbf{L}$), $\mathbf{W}^{\mathrm{p}}$ is the plastic spin tensor, and $\mathbf{A}^{\alpha}$ is the skew-symmetric part of $\vec{\mathbf{m}}^{\alpha} \otimes \vec{\mathbf{n}}^{\alpha}$. The evolution of the slip resistance s^{α} in terms of the slip rates is described by an isotropic saturation-type law

$$\forall \alpha = 1, \dots, N_s \colon \dot{s}^{\alpha} = \; h_0 \left(1 - \frac{s^{\alpha}}{s^{s}}\right)^{a} \left(\sum_{\beta=1}^{N_s} \left|\dot{\gamma}^{\beta}\right|\right) \tag{4.9}$$

where h_0, s^s and a are hardening parameters.

The full-constraints Taylor model is used to determine the overall mechanical behavior of the polycrystalline aggregate from the mechanical behavior of its microscopic constituents (the single crystals). This model is based on the assumption of a uniform velocity gradient over all the crystals that compose the polycrystalline aggregate. Accordingly, the macroscopic velocity gradient $\bar{\mathbf{L}}$ is assumed to be equal to its microscopic counterparts $\mathbf{L}$ (relating to individual grains). By assuming that the microscopic Cauchy stress tensor $\boldsymbol{\sigma}$ is homogeneous over each grain (or single crystal), the deviatoric part of the macroscopic Cauchy stress tensor $\bar{\mathbf{S}}$ can be related to its microscopic counterpart $\mathbf{S}^i$, corresponding to grain i, by

$$\bar{\mathbf{S}} = \sum_{i=1}^{N_g} \vartheta^i \mathbf{S}^i \tag{4.10}$$

where ϑ^i is the volume fraction corresponding to grain i, and N_g is the total number of grains that form the polycrystalline aggregate. Analogous to the treatment at the microscopic scale, the condensed form of the macroscopic tangent compliance $\bar{\mathbf{M}}$ can be defined as follows:

$$\bar{\mathbf{M}} = \frac{\partial \bar{\mathbf{D}}_{\mathrm{v}}}{\partial \bar{\mathbf{S}}_{\mathrm{v}}} \tag{4.11}$$

where $\bar{\mathbf{D}}_{\mathrm{v}}$ denotes the vector storage of the macroscopic strain rate tensor $\bar{\mathbf{D}}$ (the symmetric part of $\bar{\mathbf{L}}$), and $\bar{\mathbf{S}}_{\mathrm{v}}$ denotes the vector storage of $\bar{\mathbf{S}}$.

Making use of Eqs. (4.7), (4.10) and (4.11), $\bar{\mathbf{M}}$ can be related to the microscopic tangent compliance $\mathbf{M}$ by the following relation:

$$\bar{\mathbf{M}} = \left[\sum_{i=1}^{N_g} \vartheta^i (\mathbf{M}^i)^{-1}\right]^{-1} \tag{4.12}$$

4.2.2 Imperfection approach

4.2.2.1 Generic form for the Cauchy stress and the velocity gradient tensors

Consistent with prior literature (Hutchinson et al., 1978a), and because the sheets are assumed to be thin, the generalized plane stress assumption is adopted in the M–K analysis. This plane stress condition is generally expressed in terms of the out-of-plane components of the macroscopic Cauchy stress tensor $\bar{\boldsymbol{\sigma}}$ by

$$\bar{\sigma}_{13} = \bar{\sigma}_{23} = \bar{\sigma}_{33} = 0 \tag{4.13}$$

Accordingly, $\bar{\boldsymbol{\sigma}}$ can be expressed in the following generic form:

$$\bar{\boldsymbol{\sigma}} = \begin{pmatrix} \bar{\sigma}_{11} & \bar{\sigma}_{12} & 0 \\ \bar{\sigma}_{12} & \bar{\sigma}_{22} & 0 \\ 0 & 0 & 0 \end{pmatrix} \tag{4.14}$$

In the current work, we restrict our attention to the prediction of localized necking in polycrystals with orthotropic crystallographic texture. The consideration of orthotropic texture in conjunction with the plane stress state implies that the out-of-plane components of the macroscopic velocity gradient $\bar{\mathbf{L}}$ are equal to zero (Knockaert et al., 2000; Signorelli et al., 2009; Yoshida and Kuroda, 2012; Tadano et al., 2013)

$$\bar{L}_{13} = \bar{L}_{31} = \bar{L}_{23} = \bar{L}_{32} = 0 \tag{4.15}$$

Furthermore, due to the rigid-viscoplastic behavior considered, the incompressibility condition implies that

$$\bar{L}_{33} = -(\bar{L}_{11} + \bar{L}_{22}) \tag{4.16}$$

By combining Eqs. (4.15) and (4.16), the relevant form of $\bar{\mathbf{L}}$ applicable to our study can be expressed as

$$\bar{\mathbf{L}} = \begin{pmatrix} \bar{L}_{11} & \bar{L}_{12} & 0 \\ \bar{L}_{21} & \bar{L}_{22} & 0 \\ 0 & 0 & -(\bar{L}_{11} + \bar{L}_{22}) \end{pmatrix} \tag{4.17}$$

4.2.2.2 Formulation of the imperfection approach

The M–K analysis is based on the assumption of a preexisting initial geometric imperfection in the form of a narrow band across the width of the metal sheet, as illustrated in Figure 4.1. The width of this band is assumed to be very small and its exact value does not mater, since it is not a relevant parameter in this classical necking

modeling approach. Indeed, in this conventional initial imperfection approach, only the relative thickness of the groove is of importance, which is updated all along the computations. Accordingly, the groove shown in Figure 4.1 is plotted with a large width only to clearly illustrate the concept of the initial imperfection approach. Quantities outside and inside the band are designated by superscripts H and B, respectively.

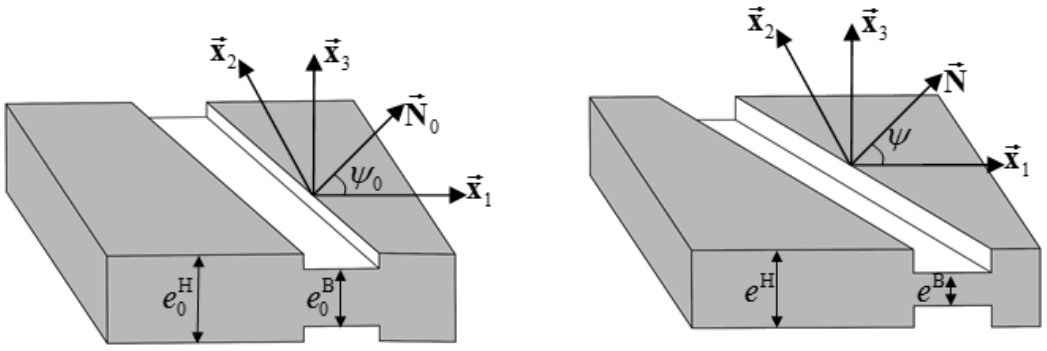

(a) (b)

Figure 4.1: M–K analysis for a metal sheet: (a) Initial geometry of the sheet; (b) Current geometry of the sheet.

For the FLD prediction, the sheet is submitted to in-plane biaxial loading along the axes $\vec{\mathbf{x}}_1$ (which can be selected to be aligned with the rolling direction of the sheet) and $\vec{\mathbf{x}}_2$ (which can be aligned with the transverse direction of the sheet), as shown in Figure 4.1. Furthermore, the sheet is assumed to be very thin, which justifies the adoption of the assumption of plane stress. Hutchinson et al. (1978a) have proven the validity of such an assumption in the case of thin sheets. As a consequence of this classical assumption, the band remains normal to the plane of the sheet during the deformation, and the outer surfaces (in the thickness direction) remain in the plane ($\vec{\mathbf{x}}_1$, $\vec{\mathbf{x}}_2$). The

loading is prescribed so that the strain-path ratio remains constant in the homogeneous zone all along the deformation

$$\frac{\bar{L}^{\mathrm{H}}_{22}}{\bar{L}^{\mathrm{H}}_{11}} = \rho = \text{constant} \tag{4.18}$$

The incompressibility of the sheet implies that the macroscopic velocity gradient in the homogeneous zone has the following form:

$$\bar{\mathbf{L}}^{\mathrm{H}} = \begin{pmatrix} \bar{L}^{\mathrm{H}}_{11} & 0 & 0 \\ 0 & \rho\bar{L}^{\mathrm{H}}_{11} & 0 \\ 0 & 0 & -(1+\rho)\bar{L}^{\mathrm{H}}_{11} \end{pmatrix} \tag{4.19}$$

To determine the complete FLD, the strain-path ratio ρ is varied between -1/2 (uniaxial tensile state) and 1 (equibiaxial tensile state).

The M–K approach is also based on the assumption of the uniformity of deformation fields both outside and inside the band, which can be viewed as a conventional idealized modeling approach for the prediction of forming limit diagrams. This assumption has been adopted in all of the contributions in which the initial imperfection approach has been used in conjunction with crystal plasticity multiscale schemes (e.g., Inal et al., 2005; Knockaert et al., 2002; Neil and Agnew, 2009; Schwindt et al., 2015; Signorelli et al., 2009). It is recalled that the initial imperfection approach is used to predict the incipience of localized necking, which is material type instability and, as such, independent of the geometric characteristics (in contrast to geometric or structural type instabilities). Consequently, all geometric or structural effects are purposely excluded when this approach is used, as well as the associated structural type instability phenomena (e.g., wrinkling, plastic buckling). In this approach, the band and

the safe zone are restricted to remain homogeneous and, to this end, a very small representative volume element (RVE) or a material point is taken to model the mechanical behavior of these zones. At the macroscopic scale, this RVE is viewed as a homogeneous medium where the macroscopic deformation field remains uniform during the loading (not the same for both zones). However, the behavior is strongly heterogeneous at the microscopic level. Based on this consideration, the current thickness e^{H} (resp. e^{B}) is related to the initial thickness e_0^{H} (resp. e_0^{B}) by the following relation:

$$e^{\mathrm{H}} = e_0^{\mathrm{H}} \exp(\bar{\varepsilon}_{33}^{\mathrm{H}}) \;\; ; \;\; e^{\mathrm{B}} = e_0^{\mathrm{B}} \exp(\bar{\varepsilon}_{33}^{\mathrm{B}}) \tag{4.20}$$

where $\bar{\varepsilon}_{33}^{\mathrm{H}}$ and $\bar{\varepsilon}_{33}^{\mathrm{B}}$ are the logarithmic strains outside and inside the band, respectively, along the direction of the normal to the sheet.

The above-mentioned quantities can be used to quantify the initial and current geometric imperfections through the computation of the ratios

$$f_0 = \frac{e_0^{\mathrm{B}}}{e_0^{\mathrm{H}}} \;\; ; \;\; f = \frac{e^{\mathrm{B}}}{e^{\mathrm{H}}} \tag{4.21}$$

Using Eqs. (4.20) and (4.21), the current imperfection ratio f can be expressed in terms of $\bar{\varepsilon}_{33}^{\mathrm{H}}$ and $\bar{\varepsilon}_{33}^{\mathrm{B}}$ as follows:

$$f = f_0 \exp(\bar{\varepsilon}_{33}^{\mathrm{B}} - \bar{\varepsilon}_{33}^{\mathrm{H}}) \tag{4.22}$$

The initial (resp. current) imperfection is also characterized by the orientation ψ_0 (resp. ψ) of the unit vector normal to the band, $\vec{\mathbf{N}}_0$ (resp. $\vec{\mathbf{N}}$), with respect to the rolling direction of the sheet. Both $\vec{\mathbf{N}}_0$ and $\vec{\mathbf{N}}$ are constrained to lie in the $\vec{\mathbf{x}}_1 - \vec{\mathbf{x}}_2$ plane and are equal to $(\cos\psi_0, \sin\psi_0)$ and $(\cos\psi, \sin\psi)$, respectively. The current orientation ψ of the band

can be expressed in terms of its initial value ψ_0, the logarithmic strain component $\bar{\varepsilon}_{11}^{\mathrm{H}}$, and the strain-path ratio ρ equal to $\bar{\varepsilon}_{22}^{\mathrm{H}}/\bar{\varepsilon}_{11}^{\mathrm{H}}$ (Hutchinson and Neale, 1978b)

$$\psi = \arctan[\tan(\psi_0)\exp(1-\rho)\bar{\varepsilon}_{11}^{\mathrm{H}}] \tag{4.23}$$

In addition to Eqs.(4.20)-(4.23), the M–K analysis is based on three other sets of equations:

- The kinematic compatibility condition between the band and the homogeneous zone (this condition is restricted to the in-plane components of the macroscopic velocity gradient)

$$\bar{\mathbf{L}}^{\mathrm{PSB}} = \bar{\mathbf{L}}^{\mathrm{PSH}} + \vec{\dot{\mathbf{C}}} \otimes \vec{\mathbf{N}} \tag{4.24}$$

where the notation $\blacksquare^{\mathrm{PS}}$ denotes the in-plane part, defined as $\begin{pmatrix} \blacksquare_{11} & \blacksquare_{12} \\ \blacksquare_{21} & \blacksquare_{22} \end{pmatrix}$, of tensor $\blacksquare$ (where $\blacksquare$ in Eq. (4.24) corresponds to tensors $\bar{\mathbf{L}}^{\mathrm{B}}$ and $\bar{\mathbf{L}}^{\mathrm{H}}$). In Eq. (4.24), $\vec{\dot{\mathbf{C}}}$ is a 2D vector representing the jump in the velocity gradient across the boundary between the band and the homogeneous zone. The fully three-dimensional form of the velocity gradient in the band is complemented starting from Eq. (4.24) by using the incompressibility assumption, which leads to the following expression for tensor $\bar{\mathbf{L}}^{\mathrm{B}}$:

$$\bar{\mathbf{L}}^{\mathrm{B}} = \begin{pmatrix} \bar{L}_{11}^{\mathrm{H}} + \dot{C}_1 N_1 & \dot{C}_1 N_2 & 0 \\ \dot{C}_2 N_1 & \rho\bar{L}_{11}^{\mathrm{H}} + \dot{C}_2 N_2 & 0 \\ 0 & 0 & -(1+\rho)\bar{L}_{11}^{\mathrm{H}} - \dot{C}_1 N_1 - \dot{C}_2 N_2 \end{pmatrix} \tag{4.25}$$

- The equilibrium equation across the interface between the band and the homogenous zone

$$e^{\mathrm{B}}\overline{\boldsymbol{\sigma}}^{\mathrm{PSB}}.\vec{\mathbf{N}} = e^{\mathrm{H}}\overline{\boldsymbol{\sigma}}^{\mathrm{PSH}}.\vec{\mathbf{N}} \tag{4.26}$$

- The constitutive equations developed in section 4.2.1 for the modeling of the mechanical behavior of polycrystalline aggregates representing both the band and the homogeneous zone.

For practical reasons related to the numerical integration, the equilibrium equation (4.26) is written in the following compact matrix form:

$$\mathbf{B}\overline{\boldsymbol{\sigma}}_{\mathrm{r}}^{\mathrm{B}} + \left(\frac{1}{f}\right)\mathbf{b} = \mathbf{0} \tag{4.27}$$

where f is the current imperfection ratio (see Eq. (4.21)), while $\mathbf{B}$, $\overline{\boldsymbol{\sigma}}_{\mathrm{r}}^{\mathrm{B}}$ and $\mathbf{b}$ are defined as

$$\mathbf{B} = \begin{bmatrix} N_1 & 0 & N_2 \\ 0 & N_2 & N_1 \end{bmatrix} \;;\; \overline{\boldsymbol{\sigma}}_{\mathrm{r}}^{\mathrm{B}} = \begin{bmatrix} \bar{\sigma}_{11}^{\mathrm{B}} \\ \bar{\sigma}_{22}^{\mathrm{B}} \\ \bar{\sigma}_{12}^{\mathrm{B}} \end{bmatrix} \;\;;\;\; \mathbf{b} = \begin{bmatrix} -(N_1\bar{\sigma}_{11}^{\mathrm{H}} + N_2\bar{\sigma}_{12}^{\mathrm{H}}) \\ -(N_1\bar{\sigma}_{12}^{\mathrm{H}} + N_2\bar{\sigma}_{22}^{\mathrm{H}}) \end{bmatrix} \tag{4.28}$$

4.3 Numerical aspects

The conventional integration of the crystal plasticity constitutive equations (CP model) for the single crystal presented in section 4.2.1 is done using an implicit/explicit algorithm (Gupta et al., 2018) which is very similar in spirit to that developed by Kalidindi et al. (1992). Crystal plasticity results from this model are used for CP-FLD prediction. New spectral DFT database (second generation) discussed in chapter 3 is also used in this work to obtain crystal plasticity results (described as spectral crystal plasticity Taylor-type model, SCP model) in a computationally efficient manner which are further used for SCP-FLD predictions. The deviatoric part of the macroscopic Cauchy

stress tensor $\bar{\mathbf{S}}$ is obtained either from CP or SCP model. Thereafter, the macroscopic Cauchy stress tensor $\bar{\boldsymbol{\sigma}}$ can be determined, under the plane stress condition, through the following relation:

$$\bar{\boldsymbol{\sigma}} = \bar{\mathbf{S}} - \bar{S}_{33}\mathbf{I}_2 \tag{4.29}$$

When the plane stress assumption is adopted, the 2D macroscopic Cauchy stress tensor $\bar{\boldsymbol{\sigma}}^{\mathrm{PS}}$ can be obtained from the components of the 3D Cauchy stress tensor $\bar{\boldsymbol{\sigma}}$ by the following relation:

$$\bar{\boldsymbol{\sigma}}^{\mathrm{PS}} = \begin{pmatrix} \bar{\sigma}_{11} & \bar{\sigma}_{12} \\ \bar{\sigma}_{12} & \bar{\sigma}_{22} \end{pmatrix} \tag{4.30}$$

Likewise, the macroscopic tangent compliance $\bar{\mathbf{M}}$ can be obtained using Eq. (4.12) from CP model during the integration of constitutive equations. This $\bar{\mathbf{M}}$ will be used to integrate the equations governing the imperfection approach below.

4.3.1 Algorithm for the FLD prediction

To predict the FLDs of sheet metals, the following algorithm is applied:

- For each strain-path ratio ρ varying from -1/2 to 1 ($\Delta\rho$ is typically set to 0.1):
    - For each time step $\mathrm{I}^{\Delta} = [t_n\,, t_{n+1}]$ (where t_{n+1} - t_n is equal to Δt) , use the CP model (when the conventional integration scheme is used such as described in Kalidindi et al. (1992)), or SCP model (when the DFT approach is employed as described in chapter 3), to integrate the constitutive equations of the polycrystal in the homogeneous zone. For this purpose, the 3D macroscopic velocity

gradient $\bar{\mathbf{L}}^{\mathrm{H}}$ given by Eq. (4.19) should be used as input for this time integration scheme, with the component $\bar{L}_{11}^{\mathrm{H}}$ fixed to one. Consequently, the components $\bar{L}_{22}^{\mathrm{H}}$ and $\bar{L}_{33}^{\mathrm{H}}$ are equal to ρ and $-(1+\rho)$, respectively. After using the CP/SCP model, the 2D macroscopic stress $\bar{\boldsymbol{\sigma}}^{\mathrm{PSH}}$ computed at t_{n+1} should be stored. The other out-of-plane components of $\bar{\boldsymbol{\sigma}}^{\mathrm{H}}$ ($\bar{\sigma}_{13}^{\mathrm{H}}$, $\bar{\sigma}_{23}^{\mathrm{H}}$ and $\bar{\sigma}_{33}^{\mathrm{H}}$) are equal to zero as a consequence of the plane stress conditions (see Eq.(4.14)). Tensor $\bar{\boldsymbol{\sigma}}^{\mathrm{PSH}}$ will be used in section 4.3.2 to determine the in-plane velocity gradient in the band $\bar{\mathbf{L}}^{\mathrm{PSB}}$, which fulfills both the compatibility and the equilibrium conditions at the interface between the homogeneous zone and the band. The computation in the homogeneous zone is stopped when $\bar{\varepsilon}_{11}^{\mathrm{H}}$ ($=\int_0^t \bar{L}_{11}^{\mathrm{H}} dt = t$) reaches a value of one.

- For each initial band inclination ψ_0 varying from 0° to 90° (with $\Delta\psi_0$ set to 1° or 1.5°).

  - For each time step $[t_n, t_{n+1}]$ (for convenience, the time steps used to integrate the mechanical behavior in the band are chosen to be the same as those taken for the integration of the mechanical behavior in the homogeneous zone):

    - Use the value of $\bar{\boldsymbol{\sigma}}^{\mathrm{PSH}}$ at t_{n+1} (determined in the previous step) to integrate the equations of the M–K analysis (see section 4.2.2.2). For the sake of clarity, the steps followed in this integration will be detailed in a separate section (section 4.3.2). The incremental integration scheme of section 4.3.2 is applied until the following condition is met:

$$\frac{\bar{L}_{33}^{\mathrm{B}}}{\bar{L}_{33}^{\mathrm{H}}} \geq 10 \tag{4.31}$$

The strain component $\bar{\varepsilon}_{11}^{\mathrm{H}}$, obtained once the criterion in Eq. (4.31) is satisfied, is considered as the critical strain $\bar{\varepsilon}_{11}^{*}$, which corresponds to the current band inclination ψ and strain-path ratio ρ.

The smallest critical strain $\bar{\varepsilon}_{11}^{*}$ predicted by the above algorithm, over all initial angles ψ_0, and the associated current angle ψ correspond, respectively, to the necking limit strain $\bar{\varepsilon}_{11}^{\mathrm{L}}$ and the necking band inclination ψ for the current strain-path ratio ρ.

4.3.2 Numerical integration of the equations governing the imperfection approach

The equations corresponding to the M–K approach, detailed in section 4.2.2.2, have been integrated in order to determine the velocity gradient in the band $\bar{\mathbf{L}}^{\mathrm{B}}$ over the loading increment I^{Δ}, and therefore to check whether the criterion in Eq. (4.31) is satisfied. To simplify the following numerical developments, the argument t_{n+1} is dropped in this section, with the implied understanding that all variables are evaluated at t_{n+1}, unless otherwise specified. As explained in the algorithm of section 4.3.1, tensor $\bar{\boldsymbol{\sigma}}^{\mathrm{PSH}}$ is known a priori. The equations governing the M-K analysis to be solved in this section are recalled:

- The compatibility condition given by Eq. (4.25).
- The equilibrium equation (4.27).
- The constitutive equations of the polycrystalline aggregate in the band.

The above set of equations will be solved by means of the Newton–Raphson iterative method.

As $\bar{L}_{11}^{\mathrm{H}}$ is set to 1 (see section 4.3.1), the macroscopic velocity gradient in the band $\bar{\mathbf{L}}^{\mathrm{B}}$, defined by Eq. (4.25), can be re-expressed as follows:

$$\bar{\mathbf{L}}^{\mathrm{B}} = \begin{pmatrix} 1 + \dot{C}_1 N_1 & \dot{C}_1 N_2 & 0 \\ \dot{C}_2 N_1 & \rho + \dot{C}_2 N_2 & 0 \\ 0 & 0 & -(1+\rho) - \dot{C}_1 N_1 - \dot{C}_2 N_2 \end{pmatrix} \tag{4.32}$$

On the other hand, as $\bar{\varepsilon}_{11}^{\mathrm{H}}$ is known and actually equal to t_{n+1} (since $\bar{L}_{11}^{\mathrm{H}}$ is fixed to 1), the current band orientation ψ (at t_{n+1}) is also known, as defined by Eq. (4.23). Consequently, the components N_1 and N_2 of $\vec{\mathbf{N}}$ are known at t_{n+1}. The computation of $\bar{\mathbf{L}}^{\mathrm{B}}$ is thus reduced to the computation of the components $\dot{C}_1$ and $\dot{C}_2$ of the jump vector. In turn, $\dot{C}_1$ and $\dot{C}_2$ can be determined by solving the equilibrium equation (4.27). The latter may be viewed as a system of two nonlinear equations, which is function of the unknown vector $\dot{\vec{\mathbf{C}}} = (\dot{C}_1, \dot{C}_2)$

$$\mathbf{E} \widehat{=} \mathbf{E}\left(\dot{\vec{\mathbf{C}}}\right) = \mathbf{B}.\bar{\boldsymbol{\sigma}}_{\mathrm{r}}^{\mathrm{B}} + \left(\frac{1}{f}\right)\mathbf{b} = \mathbf{0} \tag{4.33}$$

The classical Newton–Raphson method is then used to solve Eq. (4.33). In this process, and for the computation of the analytical expression of the Jacobian matrix $\frac{\partial \mathbf{E}}{\partial \dot{\vec{\mathbf{C}}}}$, let us introduce the reduced vectors $\bar{\boldsymbol{\sigma}}_{\mathrm{r}}^{\mathrm{B}}$ and $\bar{\mathbf{D}}_{\mathrm{r}}^{\mathrm{B}}$ as

$$\bar{\boldsymbol{\sigma}}_{\mathrm{r}}^{\mathrm{B}} = \begin{bmatrix} \bar{\sigma}_{11}^{B} \\ \bar{\sigma}_{22}^{B} \\ \bar{\sigma}_{12}^{B} \end{bmatrix} \; ; \; \bar{\mathbf{D}}_{\mathrm{r}}^{\mathrm{B}} = \begin{bmatrix} \bar{D}_{11}^{B} \\ \bar{D}_{22}^{B} \\ \bar{D}_{12}^{B} \end{bmatrix} \tag{4.34}$$

By introducing $\bar{\mathbf{D}}_{\mathrm{r}}^{\mathrm{B}}$, $\frac{\partial \mathbf{E}}{\partial \dot{\bar{\mathbf{C}}}}$ can be obtained by the following chain rule:

$$\frac{\partial \mathbf{E}}{\partial \dot{\bar{\mathbf{C}}}} = \frac{\partial \mathbf{E}}{\partial \bar{\mathbf{D}}_{\mathrm{r}}^{\mathrm{B}}} . \frac{\partial \bar{\mathbf{D}}_{\mathrm{r}}^{\mathrm{B}}}{\partial \dot{\bar{\mathbf{C}}}} \tag{4.35}$$

The partial derivative $\frac{\partial \bar{\mathbf{D}}_{\mathrm{r}}^{\mathrm{B}}}{\partial \dot{\bar{\mathbf{C}}}}$, introduced in Eq. (4.35), can be computed using Eq. (4.32)

$$\frac{\partial \bar{\mathbf{D}}_{\mathrm{r}}^{\mathrm{B}}}{\partial \dot{\bar{\mathbf{C}}}} = \begin{bmatrix} N_1 & 0 \\ 0 & N_2 \\ N_2/2 & N_1/2 \end{bmatrix} \tag{4.36}$$

Using Eq. (4.33), the matrix $\frac{\partial \mathbf{E}}{\partial \bar{\mathbf{D}}_{\mathrm{r}}^{\mathrm{B}}}$, introduced in Eq. (4.35), can be expressed as

$$\frac{\partial \mathbf{E}}{\partial \bar{\mathbf{D}}_{\mathrm{r}}^{\mathrm{B}}} = \mathbf{B} . \frac{\partial \bar{\boldsymbol{\sigma}}_{\mathrm{r}}^{\mathrm{B}}}{\partial \bar{\mathbf{D}}_{\mathrm{r}}^{\mathrm{B}}} + \mathbf{b} \otimes \frac{\partial (\frac{1}{f})}{\partial \bar{\mathbf{D}}_{\mathrm{r}}^{\mathrm{B}}} \tag{4.37}$$

While $\frac{\partial \bar{\boldsymbol{\sigma}}_{\mathrm{r}}^{\mathrm{B}}}{\partial \bar{\mathbf{D}}_{\mathrm{r}}^{\mathrm{B}}}$ can be extracted from the inverse of the macroscopic tangent compliance $\bar{\mathbf{M}}^{-1}$ (see Eq. (4.12)), as follows:

$$\frac{\partial \bar{\boldsymbol{\sigma}}_{\mathrm{r}}^{\mathrm{B}}}{\partial \bar{\mathbf{D}}_{\mathrm{r}}^{\mathrm{B}}} = \begin{bmatrix} 2\bar{M}_{11}^{-1} + \bar{M}_{21}^{-1} & 2\bar{M}_{12}^{-1} + \bar{M}_{22}^{-1} & 2\bar{M}_{13}^{-1} + \bar{M}_{23}^{-1} \\ \bar{M}_{11}^{-1} + 2\bar{M}_{21}^{-1} & \bar{M}_{12}^{-1} + 2\bar{M}_{22}^{-1} & \bar{M}_{13}^{-1} + 2\bar{M}_{23}^{-1} \\ \bar{M}_{31}^{-1} & \bar{M}_{32}^{-1} & \bar{M}_{33}^{-1} \end{bmatrix} \tag{4.38}$$

As to the imperfection ratio f, it can be determined from Eq. (4.22) as follows:

$$f = f_0 \exp(\bar{\varepsilon}_{33}^{\mathrm{B}}(t_n) + \Delta t \bar{L}_{33}^{\mathrm{B}} - \bar{\varepsilon}_{33}^{\mathrm{H}}) \tag{4.39}$$

Where $\bar{\varepsilon}_{33}^{\mathrm{B}}(t_n)$ is the 33 component of the logarithmic strain tensor in the band at t_n, and $\bar{\varepsilon}_{33}^{\mathrm{H}}$ is the 33 component of the logarithmic strain tensor in the homogeneous zone at t_{n+1}.

As $\bar{D}_{33}^{\mathrm{H}}$ is constant and equal to $-(1+\rho)$, $\bar{\varepsilon}_{33}^{\mathrm{H}}$ is simply equal to $-(1+\rho)t_{n+1}$. Finally, $\frac{\partial(\frac{1}{f})}{\partial \bar{\mathbf{D}}_{\mathrm{r}}^{\mathrm{B}}}$ can be expressed as follows:

$$\frac{\partial(1/f)}{\partial \bar{\mathbf{D}}_{\mathrm{r}}^{\mathrm{B}}} = \left[\frac{\partial(1/f)}{\partial \bar{D}_{33}^{\mathrm{B}}}\frac{\partial \bar{D}_{33}^{\mathrm{B}}}{\partial \bar{D}_{11}^{\mathrm{B}}} \quad \frac{\partial(1/f)}{\partial \bar{D}_{33}^{\mathrm{B}}}\frac{\partial \bar{D}_{33}^{\mathrm{B}}}{\partial \bar{D}_{22}^{\mathrm{B}}} \quad 0\right] \tag{4.40}$$

Using Eq. (4.39), $\frac{\partial(1/f)}{\partial \bar{D}_{33}^{\mathrm{B}}}$ reads

$$\frac{\partial(1/f)}{\partial \bar{D}_{33}^{\mathrm{B}}} = -\frac{\Delta t}{f} \tag{4.41}$$

The incompressibility condition leads to the following relations:

$$\frac{\partial \bar{D}_{33}^{\mathrm{B}}}{\partial \bar{D}_{11}^{\mathrm{B}}} = -1 \; ; \; \frac{\partial \bar{D}_{33}^{\mathrm{B}}}{\partial \bar{D}_{22}^{\mathrm{B}}} = -1 \tag{4.42}$$

The insertion of Eqs. (4.41) and (4.42) into Eq. (4.40) gives

$$\frac{\partial(1/f)}{\partial \bar{\mathbf{D}}_{\mathrm{r}}^{\mathrm{B}}} = \left[\frac{\Delta t}{f} \quad \frac{\Delta t}{f} \quad 0\right] \tag{4.43}$$

Substituting Eqs. (4.36)-(4.38), and (4.43) into Eq. (4.35) gives the analytical Jacobian matrix $\frac{\partial \mathbf{E}}{\partial \dot{\mathbf{C}}}$.

The Jacobian matrix $\frac{\partial \mathbf{E}}{\partial \dot{\mathbf{C}}}$ is analytically determined by using the above developments when the CP-FLD model is used. However, this matrix is evaluated numerically in the case of SCP-FLD model. This latter choice is adopted because the strain-rate sensitivity parameter m is set to small values (typically about 0.01), which leads to a very stiff set of crystal plasticity equations. In this case, the analytical Jacobian

matrix may become unstable even due to very small difference in stress values predicted from CP and SCP models, i.e., even a very small error in stress values may lead to a very big macroscopic tangent compliance $\bar{\mathbf{M}}$ leading to an unstable analytical Jacobian matrix. Therefore, the center difference approximation is used to numerically compute the components of the Jacobian matrix $\frac{\partial \mathbf{E}}{\partial \dot{\mathbf{C}}}$. For instance, the component $\frac{\partial E_1}{\partial \dot{C}_2}$ is computed by the following equation:

$$\frac{\partial E_1}{\partial \dot{C}_2} = \frac{E_1(\dot{C}_1, \dot{C}_2 + dh_2) - E_1(\dot{C}_1, \dot{C}_2 - dh_2)}{2dh_2} \tag{4.44}$$

As mentioned in the beginning of the current section, it is recalled that the band inclination ψ and the Cauchy stress tensor in the homogeneous zone $\bar{\boldsymbol{\sigma}}^{\mathrm{H}}$ are known at the end of the prescribed time increment $\mathrm{I}^{\Delta} = [t_n, t_{n+1}]$. The algorithm used for the integration of the M–K governing equations over I^{Δ} is defined by the following three main steps (Step $0 \rightarrow 2$). Subscript k refers to the current Newton–Raphson iteration:

- Step 0:

  - Set the iteration counter k to 0.

  - Set $\dot{C}_1^{(0)}$ and $\dot{C}_2^{(0)}$ to their converged values at the previous time increment.

For $k \geq 1$, do the following steps:

- Step 1:

  - Use Eq. (4.32) to compute $\bar{\mathbf{L}}^{\mathrm{B}(k-1)}$.

- Use either CP model (when the conventional integration scheme is used), or the SCP model (when the DFT approach is employed), to integrate the mechanical behavior of the polycrystalline aggregate representing the band. This allows the calculation of the macroscopic Cauchy stress tensor $\overline{\boldsymbol{\sigma}}^{\mathrm{B}(k-1)}$ and, in case of CP-FLD, also the macroscopic tangent compliance $\overline{\mathbf{M}}^{\mathrm{B}(k-1)}$.

- Calculate the current iteration $f^{(k-1)}$ of the imperfection factor:

$$f^{(k-1)} = f_0 \exp(\bar{\varepsilon}_{33}^{\mathrm{B}}(t_n) + \Delta t \bar{L}_{33}^{\mathrm{B}(k-1)} - \bar{\varepsilon}_{33}^{\mathrm{H}}) \tag{4.45}$$

- Introduce $\overline{\boldsymbol{\sigma}}^{\mathrm{H}}$, $f^{(k-1)}$ and $\overline{\boldsymbol{\sigma}}^{\mathrm{B}(k-1)}$ in Eq. (4.33) to compute the residual vector $\mathbf{E}(\dot{\mathbf{C}}^{(k-1)})$. Also, compute the Jacobian matrix $\frac{\partial \mathbf{E}(\dot{\mathbf{C}}^{(k-1)})}{\partial \dot{\mathbf{C}}}$, either analytically (for CP-FLD) by introducing $\overline{\mathbf{M}}^{\mathrm{B}(k-1)}$ in Eq. (4.35), or numerically (for SCP-FLD).

- If $\left\|\mathbf{E}(\dot{\mathbf{C}}^{(k-1)})\right\| \leq 10^{-3}$, then the iterative procedure used to determine the jump vector $\dot{\mathbf{C}}$ has converged. In such a case, exit the iterative process; else, go to Step 2.

- Step 2:

- Compute the new iteration $\dot{\mathbf{C}}^{(k)}$ as

$$\dot{\tilde{\mathbf{C}}}^{(k)} = \dot{\tilde{\mathbf{C}}}^{(k-1)} + \delta\dot{\tilde{\mathbf{C}}}^{(k-1)} \; ; \; \delta\dot{\tilde{\mathbf{C}}}^{(k-1)} = -\left[\frac{\partial \mathbf{E}(\dot{\mathbf{C}}^{(k-1)})}{\partial \dot{\tilde{\mathbf{C}}}}\right]^{-1} . \mathbf{E}(\dot{\tilde{\mathbf{C}}}^{(k-1)}) \tag{4.46}$$

- Set $k \leftarrow k+1$ and go to Step 1.

Unfortunately, the classical Newton–Raphson algorithm, defined by the previous three steps, sometimes confronts numerical difficulties. For example, when the initial guess is relatively far from the solution, the method might not converge or may converge very slowly. To avoid this shortcoming, a line search strategy leading to a global Newton–Raphson method can be applied. Further details on the implementation of this line search strategy into the Newton–Raphson iterations are provided in Akpama et al. (2016).

4.4 Numerical results

It is well known that the predicted FLD is dependent on strain-rate sensitivity, plastic anisotropy, temperature and damage-induced softening, as already discussed in section 4.1. In addition to these, it is also sensitive to the value of the initial imperfection factor f_0 (Wu et al., 1997; McGinty and McDowell, 2004). Hence, some numerical simulations are realized using CP-FLD for deciding the value of the imperfection factor to be used for comparison with SCP-FLD results. The hardening parameters used were the same as defined for results in Figure 3.3 for OFHC copper. The polycrystal for both homogeneous and band zones are made of 1000 single crystals possessing random initial texture. The time increment used in the different simulations of the current section is set to 10^{-3} s. Note that this time increment is much lower than that used for SCP model in chapter 3 for results in Figure 3.3, because stress values obtained from SCP model were also used to satisfy equilibrium equation between homogeneous and band zones for FLD prediction, which requires a smaller strain step for convergence of results. Figure 4.2 shows the predicted FLDs for three different values of f_0: 0.995, 0.99 and 0.98. The

results shown in Figure 4.2 are consistent with the trends shown in prior literature (Wu et al., 1997; McGinty and McDowell, 2004).

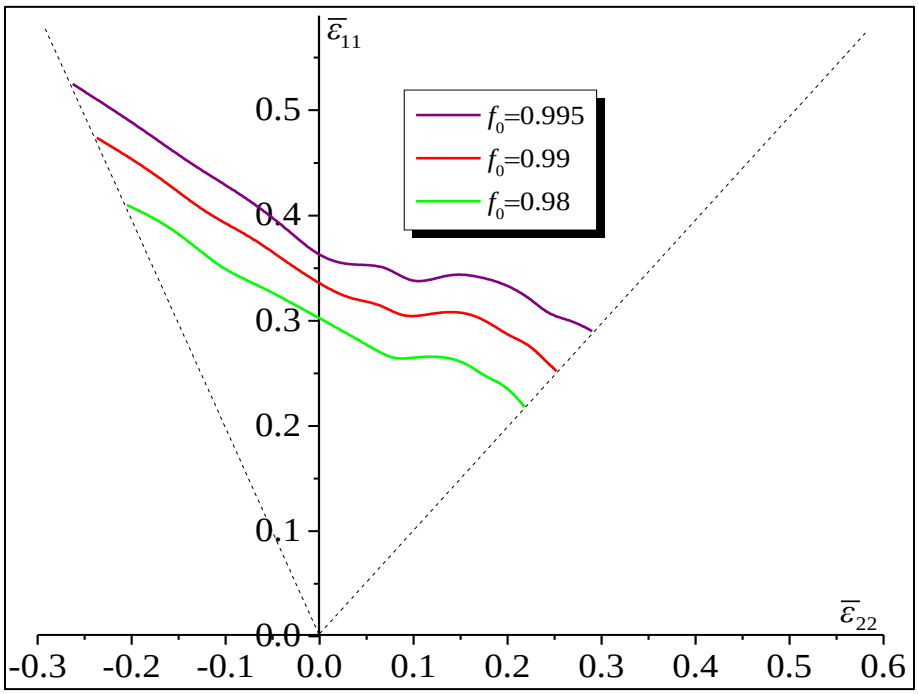

Figure 4.2: CP-FLD predictions for three different values of initial imperfection factor

The new spectral DFT database developed in Chapter 3 is used with the SCP model for the FLD predictions (SCP-FLD). These predictions are compared in Figure 4.3 and Figure 4.4 with the FLDs predicted using conventional crystal plasticity model (CP-FLD). The hardening parameters used in the different predictions of Figure 4.3 and Figure 4.4 are given in Table 4.2. For both simulations, the initial imperfection factor f_0 was fixed to 0.99. The polycrystals used in these simulations are made of 1000 FCC single crystals possessing random initial texture. The SCP parameters used for the FLD predictions are the same as the ones defined in chapter 3 for results in Figure 3.3, i.e., 500 dominant DFTs were chosen for deviatoric stress components and total shear rate, and

2000 dominant DFTs for plastic spin components. As has been demonstrated in Knezevic et al. (2008, 2009), stress–strain and texture predictions improve on using a higher number of dominant DFTs but that will also increase the computational cost. Therefore, the previous choice of number of dominant DFTs used (500 for deviatoric stress components and total shear rate, and 2000 for plastic spin components) seems to be a good compromise between accuracy and computational time in this work. If one needed to establish the FLDs for a very large number of candidate materials in designing a component, at the very least, the proposed methodology would serve to down select from the large list and perform more accurate (and expensive) computations on the shorter list. Different values of $\Delta\psi_0$ (the step size of the initial groove orientation) were tried. It was observed that when $\Delta\psi_0$ is equal to 1°, the SCP-FLD model allows obtaining the most optimized computations (with the minimum of CPU time and the maximum of accuracy). By analyzing Figure 4.3 and Figure 4.4, one can easily see that the results obtained by both models (namely the SCP-FLD and CP-FLD) match very well. It can also be seen from these two figures, that the shape of FLD is different for these two sets of hardening parameters.

Table 4.2: Hardening parameters used in the simulations of Figure 4.3 and Figure 4.4.

	h_0 (MPa)	s_s (MPa)	a	s_0 (MPa)	m
Figure 4.3	180	148	2.25	16	0.01
Figure 4.4	500	230	2.8	50	0.01

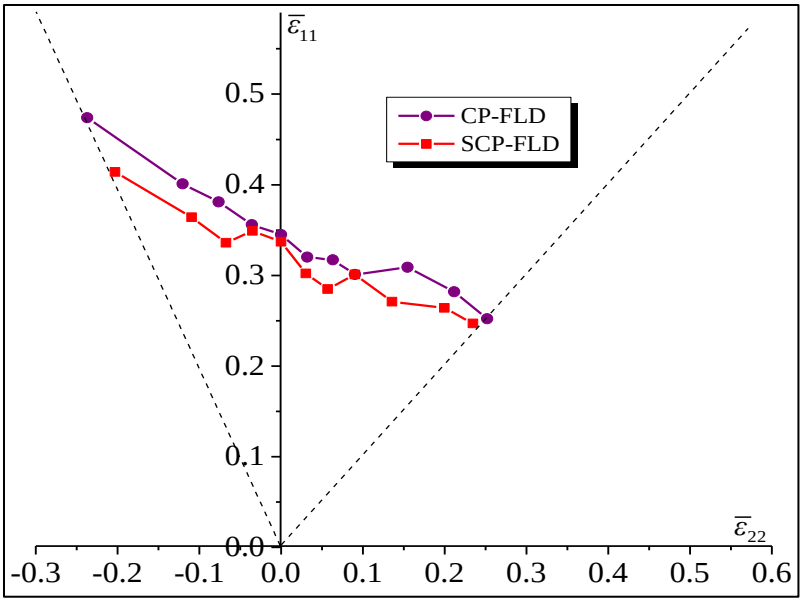

Figure 4.3: Predicted FLDs using conventional crystal plasticity model (CP-FLD) and spectral crystal plasticity model using DFT database (SCP-FLD) for the following hardening parameters: h_0 = 180 MPa, s_s = 148 MPa, a = 2.25, s_0 = 16 MPa and m = 0.01 and polycrystal consisting of 1000 single crystals.

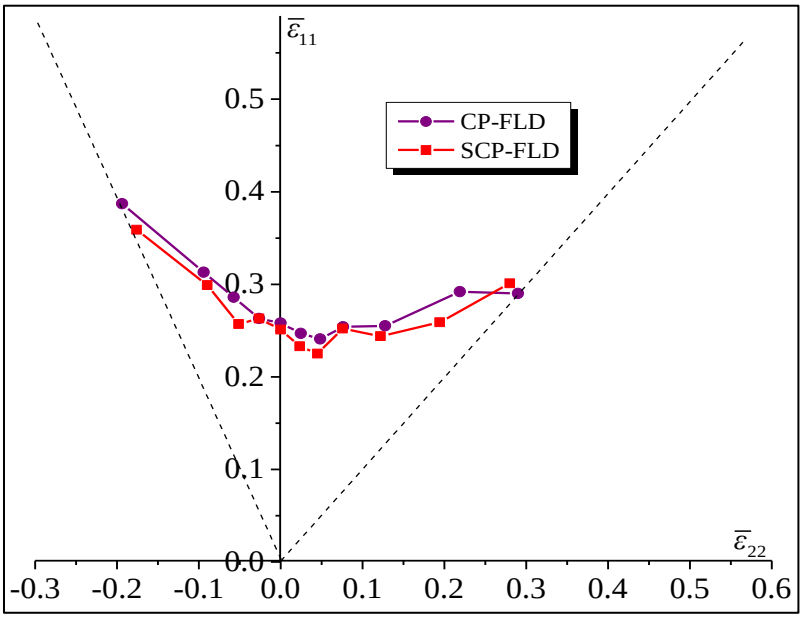

Figure 4.4: Predicted FLDs using conventional crystal plasticity model (CP-FLD) and spectral crystal plasticity model using DFT database (SCP-FLD) for the following hardening parameters: h_0 = 500 MPa, s_s = 230 MPa, a = 2.8, s_0 = 50 MPa and m = 0.01 and polycrystal consisting of 1000 single crystals.

In Figure 4.5(a), we compare the evolution of the critical strain $\bar{\varepsilon}_{11}^{*}$, as a function of the initial band orientation Ψ_0, as predicted by the conventional (CP-FLD) and the database (SCP-FLD) approaches for two different strain-path ratios: $\rho = -0.3$ and $\rho = 0.3$. The material parameters corresponding to Figure 4.5 are the same as those used to obtain the predictions of Figure 4.4. From Figure 4.5(a), a similar trend can be observed for the evolution of the critical strain in the predictions from the two approaches. As already described, the necking band orientation ψ corresponding to each strain-path ratio ρ is the one minimizing the critical strain $\bar{\varepsilon}_{11}^{*}$ (among all possible initial band orientations). The plots of the necking band orientation ψ versus the strain-path ratio ρ are displayed in Figure 4.5(b) for both CP-FLD and SCP-FLD computations. From Figure 4.5(b), one can conclude that for positive strain-path ratios, the two approaches give exactly the same results. For this range of strain paths, the necking band orientation ψ is always equal to 0°. However, for negative strain-path ratios, the SCP model gives the limit strain at a somewhat lower necking band angle compared to the CP model.

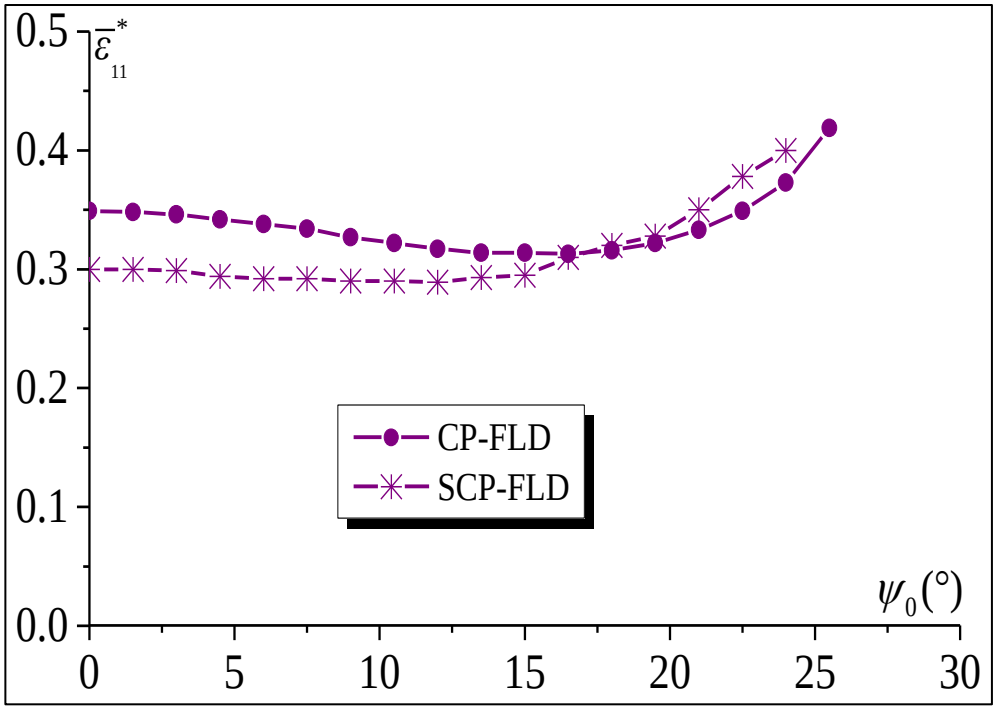

$\rho = -0.3$

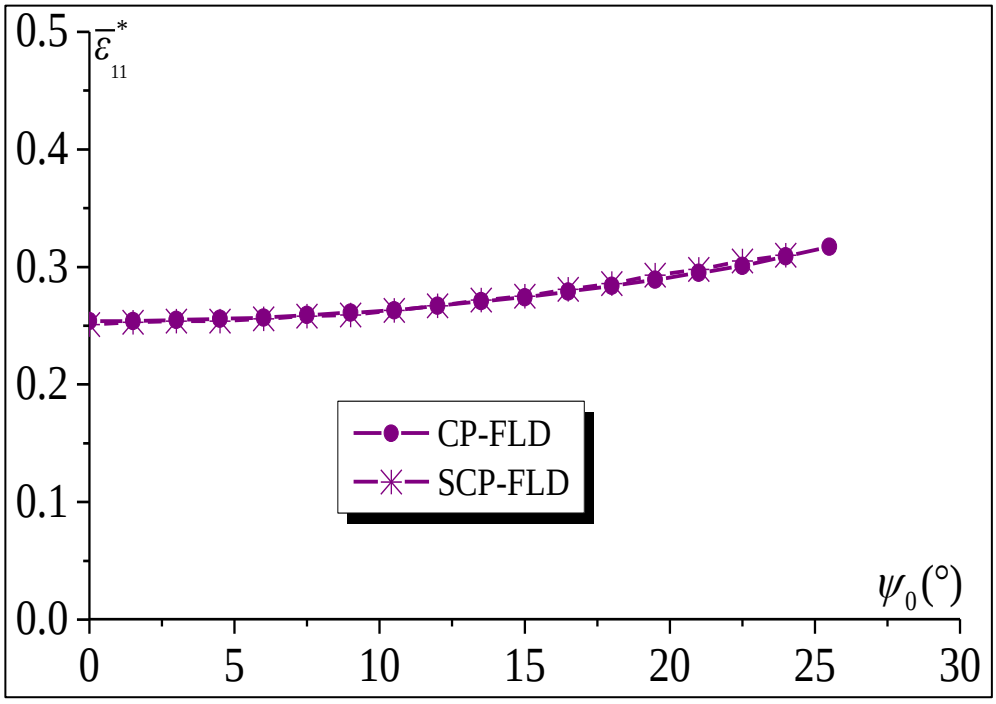

$\rho = 0.3$

(a)

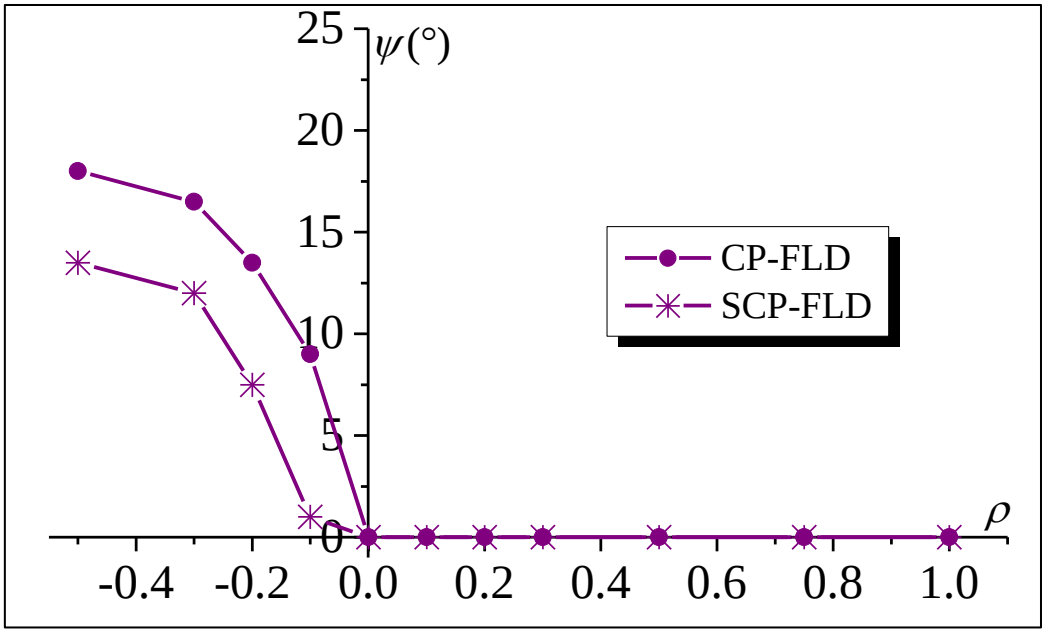

(b)

Figure 4.5: (a) Evolution of the critical strain $\bar{\varepsilon}_{11}^{*}$ versus the initial band orientation Ψ_0 as predicted by both CP-FLD and SCP-FLD models for two particular strain-path ratios ($\rho = -0.3$ and $\rho = 0.3$); (b) Evolution of the necking band orientation ψ as a function of the strain-path ratio ρ as predicted by both CP-FLD and SCP-FLD models.

The FLDs predicted in Figure 4.3 and Figure 4.4 correspond to a material with random initial texture. In general, a textured material exhibits more anisotropic behavior. Figure 4.6 presents a comparison of FLD predictions involving a textured material. The initial texture used in this calculation corresponds to the texture predicted by a Taylor-type model after a plane strain compression (PSC) to a true strain of -0.5. The hardening parameters of the material are taken the same as in Figure 4.4. The results from conventional CP-FLD computations reported in Figure 4.6(a) reveal that, in the negative range of strain-path ratios, the shape and the level of the FLD predicted for the textured material are almost the same as those with random initial texture. However, the two FLDs differ significantly in the positive range of strain-path ratios, especially in

the vicinity of equibiaxial stretching. This observation is consistent with other reports in the literature (Barlat, 1987; Wu et al., 2004; Yoshida et al., 2007; Signorelli et al., 2009). It has been found that the initial and induced plastic anisotropy mainly influence the yield surface shape and its evolution during plastic deformation. The yield surface shape has, in turn, a tremendous effect on the forming limit diagrams. For the biaxial stretching range, it has been demonstrated that a decrease in the sharpness of the yield locus in the equibiaxial stretching is a factor promoting larger limit strains (Neale and Chater, 1980). The good agreement between the CP-FLD and SCP-FLD in Figure 4.6(b) provides support for the claims made earlier that the databases developed here are indeed independent of the initial texture.

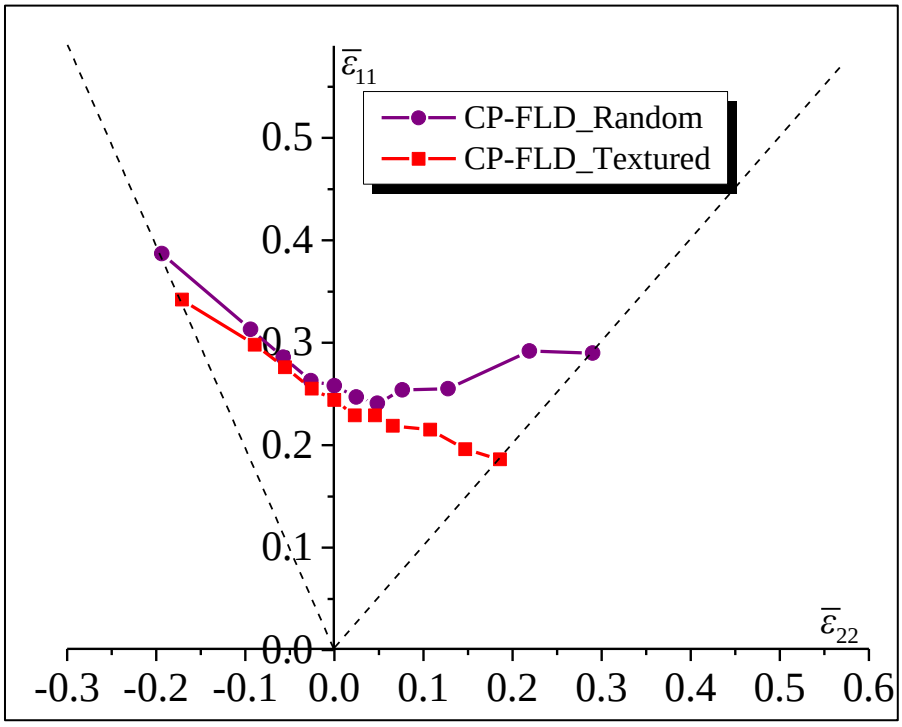

(a)

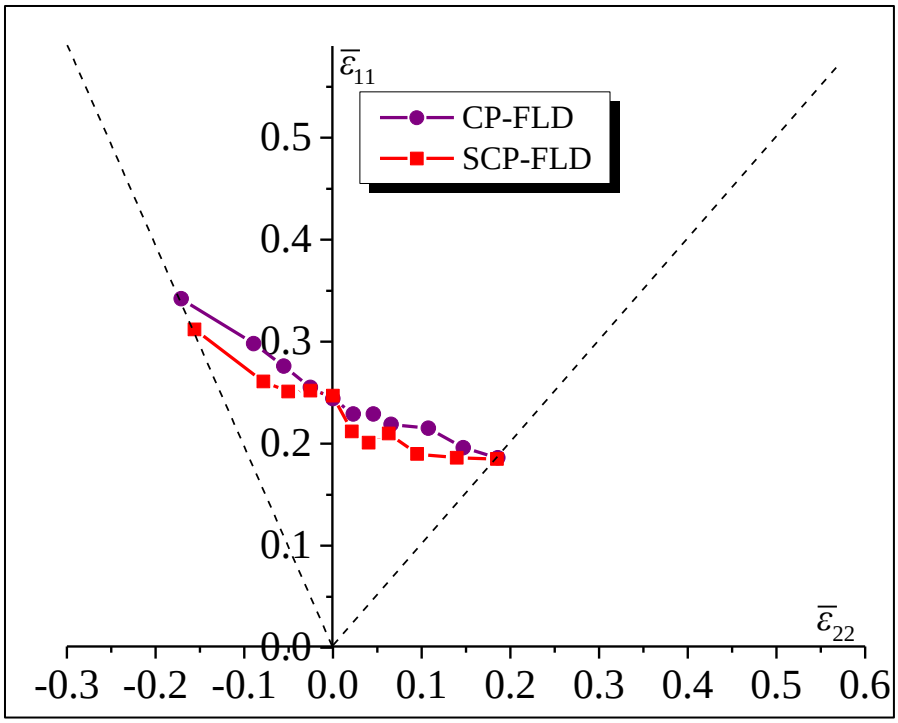

(b)

Figure 4.6: Impact of the initial texture: (a) Comparison of the CP-FLDs predicted with an initially random texture and a textured material (texture corresponding to plane strain compression to a true strain of -0.5 on the initially random texture using a Taylor-type model); (b) Comparison of the CP-FLD and SCP-FLD predictions for the textured material.

Since the accuracy of both CP-FLD and SCP-FLD models is nearly the same, we compare the CPU times required by these techniques to obtain the FLDs which is the main motivation behind this work. It was observed in chapter 3 that, compared to the CP model, the SCP model is two orders of magnitude faster with same degree of accuracy. The accuracy of the SCP model can be increased by using a larger number of dominant DFTs. It should be noted that even using a small number of dominant DFTs similar accuracy as of the CP model was achieved. Similar observation w.r.t. accuracy between CP-FLD and SCP-FLD is observed in Figure 4.3, Figure 4.4 and Figure 4.6(b). Various

parallelization techniques can be implemented in the conventional crystal plasticity code for FLD predictions. These might include solving single crystal equations in parallel for polycrystal or solving for different strain-path ratios (ρ) in parallel. Although these would reduce the required computational time, the requirement for computational resources increases. In present study, parallelization was implemented only for CP-FLD simulations in solving the single crystal equations. CP-FLD simulations were done on a cluster at Georgia Tech using 4 processors of clock speed 2.5 GHz each and 12 GB memory. The total CPU time (sum of time taken by each processor) for predicting FLD using CP model on an average was ~500 hours. As can be seen, parallelization was essential in this case to get the solutions in a reasonable timeframe. However, the SCP-FLD simulations were performed on the same cluster using a single processor of clock speed 2.5 GHz and 12 GB memory. The total CPU time for FLD prediction using SCP model on an average is ~20 hours. Thus, the computational time (CPU time) required for predicting FLD reduces dramatically when using SCP model, resulting in about 96% savings. Indeed, one can even predict the FLD using the proposed SCP-FLD approach on a normal desktop computer/laptop. This is a significant advantage compared to the high computational resources requirement for CP-FLD. On a normal desktop computer/laptop with Intel Core i3 processor of clock speed 3.6 GHz and 4 GB memory, the SCP-FLD simulation takes ~12 hours. The gain in computational speed between CP and SCP model in chapter 3 was observed as two orders of magnitude, which is slightly lower for FLD prediction using these two models. This lower than expected gain in the computational efficiency is due to the additional calculations involved in the FLD prediction, such as those requiring the solution of the equilibrium equation between homogeneous and band

zones using Newton–Raphson iteration and subroutine calls for calculating average polycrystal stress response using crystal plasticity thousands of times. Nevertheless, the SCP model is still able to predict FLD by using only 4% of the computational time required for predicting FLD by conventional crystal plasticity model.

The studies published in literature are generally not focused on reducing the computational time for FLD prediction; hence, it is difficult to find previous reports that mention the computational time for prediction of full FLD along with reporting all the details of material and simulation parameters to be able to make a fair comparison. Therefore, due to the absence of all relevant details, it is not possible to compare our approach in terms of computational time to other numerically efficient algorithms for predicting FLD, like the one discussed in Schwindt et al. (2015) where a robust numerical procedure based on direct MK-VPSC approach is proposed. Spectral database approach is aimed at reduced-order modeling of crystal plasticity theories for general applications (within some idealizations and approximations as discussed) and essentially retains all features of a crystal plasticity theory, while being fast in evaluations. Most other reduced-order models are narrower in their scope, i.e., specific to an application. Given the highly non-monotonic strain paths simulated in arriving at FLDs, the present case study presents the toughest validation of the DFT approach to date and proposes a computationally efficient SCP-FLD tool.

4.5 Conclusions

In this chapter, a highly computationally efficient tool for predicting Forming Limit Diagrams (FLDs) was developed based on rate-dependent crystal plasticity models

using the DFT-based spectral database. It was demonstrated that the SCP model is able to predict the FLD by using only 4% of the computational time compared to conventional crystal plasticity model leading to 96% savings in computational cost. Moreover, the SCP-FLD tool allows the prediction of full FLD, implementing polycrystalline anisotropy on a normal desktop/laptop containing fast processor (e.g., Intel Core i3) in about half a day time. Thus this computationally efficient tool leads to major savings of computational cost in FLD predictions. Interestingly, it has been demonstrated by (Knezevic and Savage, 2014 ; Mihaila et. al, 2014; Savage and Knezevic, 2015) that there can be a further gain in the computational speed of SCP compared to CP, if the computations are performed on a specialized computer hardware that utilizes graphics-processing units (GPU). Thus, there is clear potential to further speed up the SCP-FLD tool presented here.

CHAPTER 5. CRITICAL EVALUATION OF NEW SPECTRAL DFT DATABASE BY INTEGRATING WITH SPECTRAL CRYSTAL PLASTICITY FINITE ELEMENT FRAMEWORK

A new DFT database (second generation) free of the discovered biases was developed in chapter 3 and for the study presented in this chapter, it is integrated with a user material subroutine (UMAT) in the commercial FEM software ABAQUS (referred henceforth as spectral UMAT) along with some other improvements in SCPFEM framework which will be detailed in this chapter. Details of the implementation of first generation DFT database in Finite Element Models has already been summarized previously in section 2.3 based on prior work (Alharbi and Kalidindi, 2015). It was observed that biases in first generation DFT database cause inaccuracies in stress-strain predictions for some cases and also cause instabilities in the computation of the jacobians needed in the finite element computations leading to convergence issues while solving governing equilibrium equations. These issues currently hinder application of SCPFEM framework to the broader range of problems and strategies have been proposed in this chapter to address these hurdles. The new spectral UMAT after integrating new DFT database and implementing proposed improvements has been found to improve the accuracy and convergence characteristics of the SCPFEM simulations, and is demonstrated in this work with selected case studies. This work establishes the necessary foundations to advance the implementation of the SCPFEM framework for performing computationally efficient simulations of complex metal forming operations such as deep drawing.

5.1 Improvements to SCPFEM framework

In a general SCPFEM simulation, different material points in a heterogeneously deforming sample are expected to experience different deformation paths. Such simulations involve drastically different decompositions of the imposed stretching tensor into elastic and plastic components at the different integration points in the finite element mesh. As a result, a robust algorithm for fast and accurate decomposition is essential for the successful implementation of SCPFEM. As discussed in section 2.3, this task involves the additive decomposition of $\mathbf{D}'$ into elastic ($\mathbf{D}^{*\prime}$) and plastic ($\mathbf{D}^{\boldsymbol{p}}$) part, and the computation of a consistent deviatoric stress tensor. Building on the prior work of Alharbi and Kalidindi (2015), a new and an efficient computational strategy for addressing this task is presented here.

This new approach developed in this work employs different algorithms depending on whether the deformation step being considered is dominated by elasticity or plasticity. Therefore, the first step in addressing the decomposition of $\mathbf{D}'$ is the formulation of a suitable criterion for deciding if the deformation step being considered is dominantly elastic. This is accomplished by exploring the two extreme cases, i.e., the step is either purely elastic or purely plastic, and evaluating the relative changes in the magnitudes of the stress tensors. If one assumes that the imposed deformation step is fully elastic, the magnitude of the corresponding stress increment is given by $\left\|\boldsymbol{\sigma}'^{\mathrm{Jmn}}(\mathbf{D}^*, \mathbf{W}^*, \Delta t)|_{\mathbf{D}^*=\mathbf{D}'} - \boldsymbol{\sigma}'(t)\right\|$, where $\boldsymbol{\sigma}'^{\mathrm{Jmn}}(\mathbf{D}^*, \mathbf{W}^*, \Delta t)$ is the approximate trial stress computed using Jaumann rate relations (Eqs. (2.12) and (2.13)) and $\boldsymbol{\sigma}'(t)$ is deviatoric stress at previous time step. On the other hand, if one assumes the deformation

step was purely plastic, the magnitude of the corresponding stress increment is given by $\|\boldsymbol{\sigma}'^{\mathrm{DFT}}(\mathbf{D}^p)|_{\mathbf{D}^p=\mathbf{D}'} - \boldsymbol{\sigma}'(\mathrm{t})\|$, where $\boldsymbol{\sigma}'^{\mathrm{DFT}}(\mathbf{D}^p)$ denotes deviatoric stress computed from the DFT database using Eq. (3.2). In the present work, if the magnitude of the stress increment in the purely elastic case is less than one-half of the magnitude of the stress increment in the purely plastic case, the deformation being considered was deemed to be dominated by elasticity. In this case, the following simple iterative scheme produced excellent convergence characteristics: (i) guess $\mathbf{D}^{\boldsymbol{p}} = \mathbf{0}$, (ii) compute $\mathbf{D}^{*\prime}$ as $(\mathbf{D}' - \mathbf{D}^{\boldsymbol{p}})$, (iii) compute $\boldsymbol{\sigma}'(\mathrm{t}+\Delta\mathrm{t})$ from Eq. (2.12), and (iv) compute $\mathbf{D}^{\boldsymbol{p}}$ from Eq. (2.1) and go back to (ii). These iterations are repeated until changes in $\boldsymbol{\sigma}'(\mathrm{t}+\Delta\mathrm{t})$ were below acceptable errors. In the simulations presented in this chapter, these iterations typically converged within 2-3 iterations.

Next, the iterative scheme is described for the case when the criterion described above for a dominantly elastic deformation step is not met. For this situation, a modified Newton-Raphson (N-R) scheme with a line search method is used to obtain a consistent value of the stress tensor that satisfies both the elastic and plastic constitutive laws:

$$[\mathbf{D}^{\boldsymbol{p}}]_{n+1} = [\mathbf{D}^{\boldsymbol{p}}]_n - \lambda\ [\mathbf{J}]_n^{-1}[\mathbf{Err}]_n \tag{5.1}$$

$$\mathbf{J} = \frac{\partial \mathbf{Err}}{\partial \mathbf{D}^{\boldsymbol{p}}} = \frac{\partial \boldsymbol{\sigma}'^{\mathrm{DFT}}(\mathbf{D}^p)}{\partial \mathbf{D}^p} + \frac{\partial \boldsymbol{\sigma}'^{\mathrm{Jmn}}(\mathbf{D}^*,\mathbf{W}^*,\Delta\mathrm{t})}{\partial \mathbf{D}^*}\ ,\ \mathbf{Err} = \boldsymbol{\sigma}'^{\mathrm{DFT}}(\mathbf{D}^p) - \boldsymbol{\sigma}'^{\mathrm{Jmn}}(\mathbf{D}^*,\mathbf{W}^*,\Delta\mathrm{t}) \tag{5.2}$$

where, $\mathbf{J}$ describes the Jacobian for N-R scheme, $\mathbf{Err}$ is the error which needs to be minimized, λ controls the magnitude of the correction based on a line search algorithm (Akpama et al., 2016), and the subscripts n and $n+1$ refer to the iteration numbers. In the line search method, for each N-R iteration, sub-iterations are performed on the

optimal selection of λ corresponding to a minimum error. These sub-iterations use a bi-section method over the range $\lambda = [0, 1]$ to identify the optimal value. N-R iterations are performed until $\|\mathbf{Err}\|/s_0 < 10^{-4}$. It was observed that convergence is achieved mostly in 3-5 iterations, with slightly higher number of iterations for material responses in the elastic-plastic transition zone. The number of N-R iterations needed to obtain sufficiently accurate solutions is strongly controlled by the selection of the initial guess for the solution variable $\mathbf{D}^p$. $\mathbf{D}^p = 0$ can be chosen as starting guess but it does not converge fast for some cases. In this study, an iterative scheme was implemented for test cases to get best starting guess for $\mathbf{D}^p$ between 0 to $\mathbf{D}'$ described as, $\mathbf{D}^p = \lambda_1 \mathbf{D}'$; $\lambda_1^{j+1} = \frac{1}{2}\lambda_1^j$ where we start with $\lambda_1 = 1$ and keep halving it down and also keep track of number of iterations it takes for N-R scheme to converge for each starting guess. The starting guess which converges in minimum iterations can be chosen as best starting guess for main simulation. It was observed that initial guess of $\mathbf{D}^p = \mathbf{D}'/2$, gave the fastest convergence for many cases.

Next, we shift our attention to the computation of the jacobian needed to satisfy the equilibrium field equations in the finite element models. In prior work (Alharbi and Kalidindi, 2015), the DFT representations in Eqs. (2.9)-(2.11) were utilized in combination with a spectral interpolation scheme to compute the jacobian needed in SCPFEM computations (described earlier in section 2.3). As described in section 3.2, the new DFT database has been deployed using a trigonometric interpolation scheme for estimating the function values for new inputs (see Eqs. (3.1)-(3.3)). Since these provide analytical representations of the functions directly, they are easily amenable to taking derivatives. Therefore, the use of Eqs. (3.1)-(3.3) is expected to produce more direct

expressions for the computation of the jacobian, when compared to the spectral interpolation strategy used in prior work (Alharbi and Kalidindi, 2015). The improved DFT database developed in this work is also expected to improve the accuracy of the jacobian computations. Corrections, similar to those used for the prediction of $\boldsymbol{\sigma}'$, would need to be performed for the derivatives of $\boldsymbol{\sigma}'$ in Eq. (2.16). For example, in the computation of $\frac{\partial \boldsymbol{\sigma}'}{\partial \theta}$, the terms $\frac{\partial \sigma'_{11}}{\partial \theta}$, $\frac{\partial \sigma'_{22}}{\partial \theta}$, and $\frac{\partial \sigma'_{33}}{\partial \theta}$ are computed independently, but a correction is made to all these terms to ensure they add up to zero by subtracting one-third of the sum of the estimated values from each term.

In the prior implementations of SCPFEM, it was observed that the computation of the jacobian for deformations involving UT and EBT (see Table 3.1) produced unstable results and hindered convergence of the global equilibrium iterations. The numerical instability was tracked to the computation of the $\frac{\partial \mathrm{g}^{\mathrm{D}}}{\partial \mathbf{D}^{p}}$ term using Eq. (2.18). Present investigations have revealed that these numerical instabilities are caused by the fact that these deformation modes produce two equal eigenvalues (see Figure 3.1). In other words, the spectral decomposition expressed in Eq. (2.17) for these two deformation modes exhibit degeneracies in the identification of the eigen vectors (any two orthogonal unit vectors on a specific plane satisfy the spectral decomposition representation). Since this instability occurs only at two specific values of θ, namely 0^0 (EBT) and 60^0 (UT), in the present work, this was addressed by simply perturbing the value of θ in the computation of the jacobian for these two conditions. This is justified because the value of the jacobian controls only the convergence rate, and not the accuracy of the SCPFEM

solutions. As an example, for the case of UT, the jacobian was computed using a θ value of 59.5^0 instead of 60^0.

5.2 Case studies of SCPFEM framework

The accuracy and stability of SCPFEM framework described in section 5.1 is verified using select case studies of UT and PSC (see Table 3.1), and results of SCPFEM simulations are compared with results of classical CPFEM approach (Kalidindi et al., 1992). As already discussed, the UT and EBT simulations could not be successfully performed using the first generation DFT database because of numerical instabilities observed in the computation of the jacobian needed in the implicit FE codes. After implementing the improvements described in chapter 3 and section 5.1, we now demonstrate the applicability of the DFT database and the SCPFEM framework to UT. Additionally, we also demonstrate the applicability of the same database and the SCPFEM framework to the PSC case in order to establish the versatility of the database (i.e., its applicability to all deformation modes) and make suitable comparisons with the previous SCPFEM implementation (Alharbi and Kalidindi, 2015). The material properties (including slip hardening parameters) used for these case studies correspond to oxygen-free high conductivity (OFHC) copper: h_0 = 180 MPa, s_s = 148 MPa, a = 2.25, s_0 = 16 MPa and m = 0.01 (Kalidindi et al., 1992). The numbers of dominant DFTs used for SCPFEM simulations are 500 dominant DFTs for $\mathbf{C}_{klmn}$ and G_{klmn}, and 2000 dominant DFTs for $\mathbf{B}_{klmn}$. The FE models for these simulations are produced using cuboid-shaped three-dimensional eight-noded C3D8 solid elements in ABAQUS (ABAQUS, 2010).

For the UT case study, the FE model consisted of 40 elements. Each integration point in this mesh is initially associated with a single crystal orientation chosen randomly from a set of 320 crystal orientations representing a random texture. Deformation was applied up to axial true strain of 0.75. The initial and deformed meshes for this case study are shown in Figure 5.1(a) and (b), respectively. Figure 5.1(c) shows the comparison of predicted stress-strain responses from SCPFEM and CPFEM simulations. The final deformed textures from these simulations are presented in Figure 5.1(d) and (e) for CPFEM and SCPFEM, respectively. The predictions from SCPFEM simulations are in very close agreement to those of CPFEM for both the stress-strain response as well as the deformed texture. Thus, SCPFEM framework shows high accuracy for UT case study despite using minimal number of dominant DFTs. This high accuracy is attributed to the systematic removal of the various biases present in the first generation DFT database. We also compare the computational efficiency of SCPFEM framework with CPFEM. The SCPFEM simulation of the UT case study (runtime ~1 minute) was about 10 times faster compared to that of the CPFEM simulation (runtime ~10 minutes).

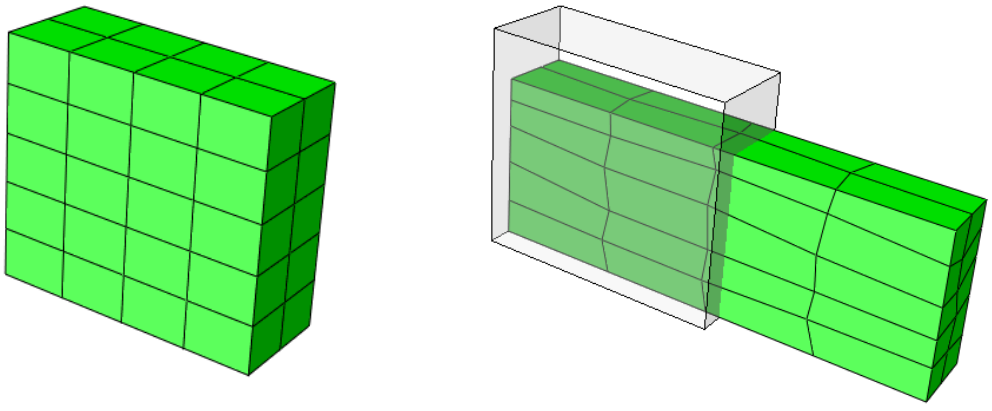

(a) (b)

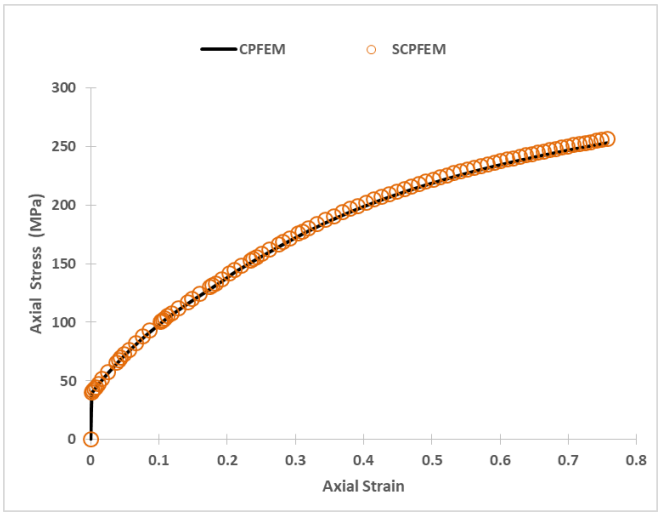
CPFEM
SCPFEM
Axial Stress (MPa)
300
250
200
150
100
50
0
0
0.1
0.2
0.3
0.4
0.5
0.6
0.7
0.8
Axial Strain

(c)

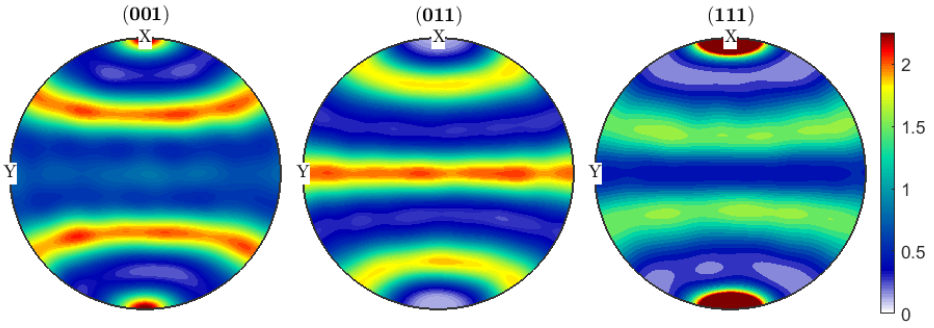
(001)
(011)
(111)
X
Y
2
1.5
1
0.5
0

(d)

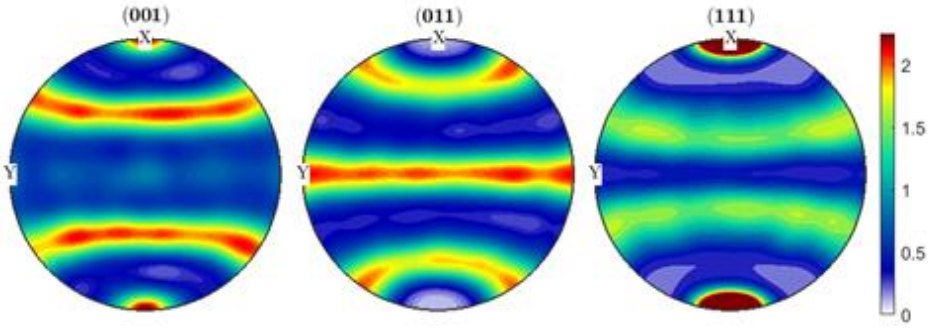
(001)
(011)
(111)
X
Y
2
1.5
1
0.5
0

(e)

Figure 5.1: Comparison of the predictions from SCPFEM and CPFEM simulations for the UT case study on polycrystalline OFHC copper: (a) initial mesh, (b) deformed mesh, (c) stress-strain curves, (d) deformed texture from CPFEM, and (e) deformed texture from SCPFEM.

For PSC case study, a bigger mesh size is considered to allow a more meaningful comparison of the accuracy and the computational efficiency between SCPFEM and CPFEM simulations. The FE model used for this case study consisted of 4000 elements and each integration point in this mesh is initially associated with a single crystal orientation chosen randomly from a set of 32000 crystal orientations representing a random texture. Deformation was applied up to axial true strain of 0.75. Figure 5.2(a) and (b) shows the initial and deformed meshes for this case study. Figure 5.2(c) shows the comparison of the predicted stress-strain responses between the SCPFEM and CPFEM simulations. The corresponding deformed textures are shown in Figure 5.2(d) and (e) for CPFEM and SCPFEM, respectively. It can be observed from Figure 5.2 that predictions from SCPFEM simulations are in very close agreement to the results of CPFEM computations with high accuracy for the PSC case study as well, using the same database that was used for the UT case study. In terms of computational efficiency, the SCPFEM simulation of PSC case study (runtime ~1.8 hours) was also about 10 times faster compared to CPFEM simulation (runtime ~18 hours). Therefore, it is seen that the SCPFEM simulations presented here produce substantial computational savings compared to the CPFEM simulations, without any significant loss of accuracy.

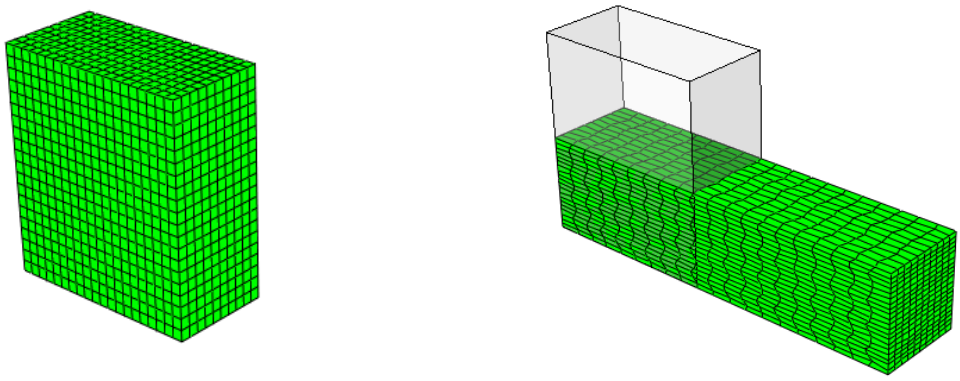

(a) (b)

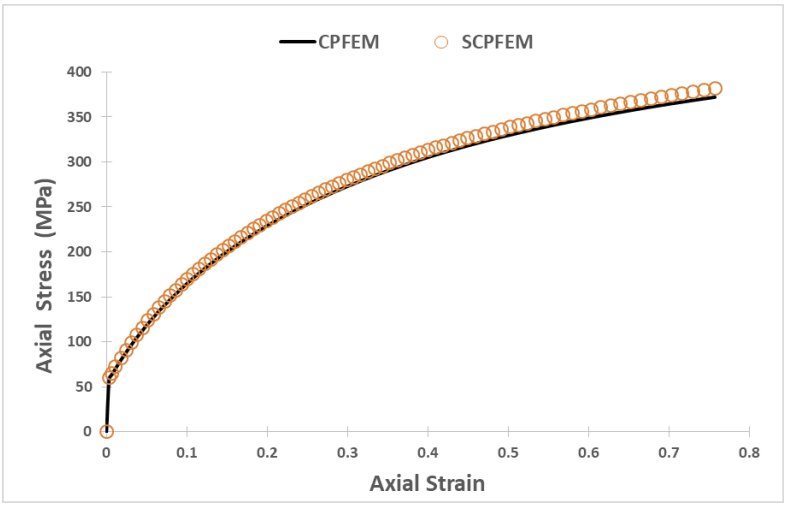
CPFEM
SCPFEM
Axial Stress (MPa)
Axial Strain
0
50
100
150
200
250
300
350
400
0
0.1
0.2
0.3
0.4
0.5
0.6
0.7
0.8

(c)

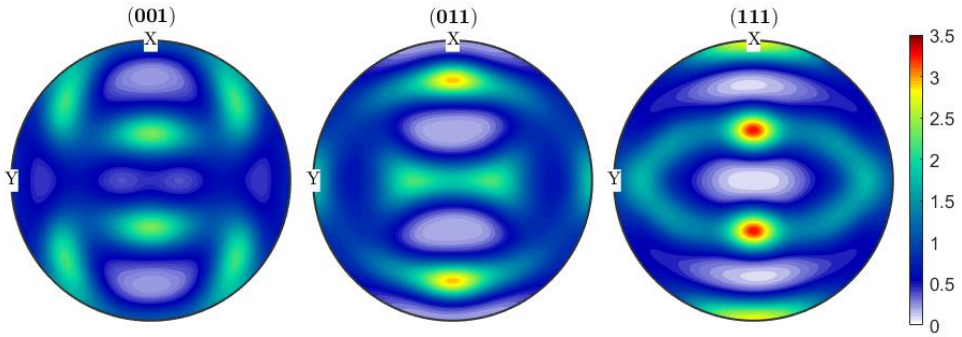
(001)
(011)
(111)
X
Y
3.5
3
2.5
2
1.5
1
0.5
0

(d)

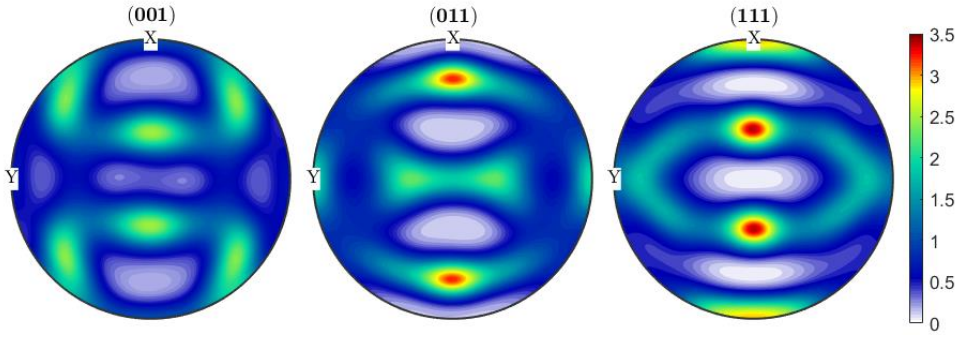

(e)

Figure 5.2: Comparison of predictions from SCPFEM and CPFEM simulations for the PSC case study on polycrystalline OFHC copper: (a) initial mesh, (b) deformed mesh, (c) stress-strain responses, (d) deformed texture from CPFEM, and (e) deformed texture from SCPFEM.

It should be noted that the prior implementations of SCPFEM framework (Alharbi and Kalidindi, 2015) have reported a speed-up of 40 times compared to the CPFEM simulations. However, this was obtained using only 150 DFTs for $\mathbf{C}_{klmn}$, G_{klmn}, and $\mathbf{B}_{klmn}$. Prior work also reported that the speed-up reduced to about 15 times, when 500 DFTs were used for $\mathbf{C}_{klmn}$, G_{klmn}, and $\mathbf{B}_{klmn}$. Obviously, as one uses more numbers of DFTs, one obtains more accurate results. Therefore, the SCPFEM framework presents the user tremendous new opportunities for making suitable trade-offs between accuracy and computational cost. In other words, one might decide to perform a larger number of low-cost (lower accuracy) simulations in the preliminary stages of their work, and then move to a smaller number of the more accurate computations as needed in their work. In the case studies presented in this work, it was decided to use larger numbers of DFTs (i.e.,

500 DFTs for $\mathbf{C}_{klmn}$ and G_{klmn}, and 2000 DFTs for $\mathbf{B}_{klmn}$). Consequently, the SCPFEM computations produced only a speed-up of 10 compared to CPFEM computations. It has also been shown in literature that significant computational efficiency can be further achieved by performing these computations on CPU-GPU architecture (Knezevic and Kalidindi, 2017).

5.3 Conclusions

In this chapter, the improved SCPFEM framework for speeding up the conventional CPFEM computations is presented by integrating new DFT database (second generation) and its efficiency is demonstrated using select case studies. After integrating the new DFT database and implementing the strategies described in this chapter related to improvement in SCPFEM framework, more accurate and stable jacobian was obtained and these strategies were also able to address the convergence issues while solving global equilibrium iterations in SCPFEM simulations. Main improvements to SCPFEM framework include, new and efficient computational strategy for decomposition of deviatoric stretching tensor and for computation of accurate stresses, and improvements to the computation of the jacobian. Results of SCPFEM simulations for both UT and PSC match very well with CPFEM and speed up of about 10 times was observed which can always be increased by using lower number of dominant DFTs and by compromising slightly on accuracy or by performing these computations on CPU-GPU architecture. This work establishes the necessary foundations to advance the implementation of the SCPFEM framework for more complex metal forming operations by providing capability to perform multiscale simulations at fraction of computational cost of conventional crystal plasticity models.

CHAPTER 6. CONCLUSIONS AND FUTURE WORK

In spectral approach to crystal plasticity framework, important variables of interest from crystal plasticity computations can be accessed directly from precomputed spectral database based on discrete Fourier transform (DFT). The generation of databases requires one-time high computational cost, and once generated they can be used for wide variety of applications. In this thesis work, new spectral DFT database (second generation) was developed by addressing the biases in first generation DFT database to generate more accurate results so that spectral DFT database and framework can be used for more complex applications of crystal plasticity simulations. Advantage of using database approach is that it leads to development of computationally efficient tools with almost similar accuracy to conventional crystal plasticity models. The tasks completed in this thesis as described in different chapters include: (1) development of new and more accurate second generation DFT database (chapter 3), (2) critical evaluation of new spectral DFT database and framework by application to crystal plasticity based forming limit diagram predictions (chapter 4), and (3) critical evaluation of new DFT database by integrating with spectral crystal plasticity finite element framework (chapter 5). Biases in first generation DFT database were identified and solution strategies were proposed and implemented to correct them. Significant improvements in the accuracy of the crystal plasticity Taylor-type computations using DFT approach (SCP model) were obtained on using new spectral DFT database especially for the cases of UT and EBT without compromising on computational efficiency. It was also demonstrated that the SCP model is able to predict the FLD by using only 4% of the computational time compared to

conventional crystal plasticity model leading to 96% savings in computational cost with very good accuracy compared to conventional method (CP-FLD). Since the computations of FLDs involve simulation of highly non-monotonic strain paths, therefore the case study presented in chapter 4 provides the toughest validation of the DFT approach to date and proposes a computationally efficient SCP-FLD tool. Significant advancements were also made to SCPFEM framework by integrating new DFT database into spectral UMAT and implementing other improvements. Main improvements to SCPFEM framework include, new and efficient computational strategy for decomposition of deviatoric stretching tensor and for computation of accurate stresses, and improvements to the computation of the jacobian to achieve better convergence characteristics while solving equilibrium field equations. The accuracy and computational efficiency of SCPFEM framework was shown with select case studies of UT and PSC for the case of single crystal at each integration point. SCPFEM simulations in this study were observed to be 10 times faster compared to CPFEM simulation while achieving similar accuracy.

These highly computationally efficient spectral crystal plasticity based toolsets will be helpful in addressing some of the challenges currently faced by materials development community and manufacturing industry in accelerated insertion of new and improved materials into practice by providing capability to perform multi-scale simulations at fraction of computational cost of conventional crystal plasticity models. Second generation DFT database developed in this work has shown high level of accuracy therefore, for future work it can be applied for many more complex applications of crystal plasticity computations where first generation DFT database caused bottlenecks due to unintended biases in it. SCP-FLD tool can be made more computationally efficient

by performing the calculations on GPU architecture so it would be good to explore this for future work to fully realize potential of this tool. SCP-FLD tool has been presently validated for FCC material systems and although same tool can be used for numerical predictions of BCC systems as well with a new DFT database for BCC, but for increasing confidence in this tool to be used in practice it can be further validated for BCC and other material systems. It can also be used by manufacturing industries as it is developed for accurate and computationally efficient FLD predictions for FCC systems by providing very fast predictions. If one needed to establish the FLDs for a very large number of candidate materials in designing a component, at the very least, the proposed methodology would serve to down select from the large list and perform more accurate (and expensive) computations on the shorter list for selection of materials. For future work it would also be good to validate this tool against experimental FLD prediction for initial textured and non-textured anisotropic material to increase the confidence in this tool for industrial applications. This should be done so that it can replace current methods used to predict FLD in industries since it is a very important safety tool in designing sheet metal forming operations. SCPFEM framework would also be very beneficial for material scientists and manufacturing industries. Therefore, future research should be built on the advancements made in this work to advance the implementation of the SCPFEM framework for carrying out computationally efficient simulations of complex metal forming operations such as deep drawing where computational speed of crystal plasticity models is usually the bottleneck. The inaccuracy of stress-strain curves and convergence issues of equilibrium equations in SCPFEM framework related to instability in jacobian computations have been identified and solution strategies which were

provided were validated for select case studies. For future work these strategies should be validated for many more deformation modes before performing complex metal forming simulations such as deep drawing. Deep drawing involves large number of deformations modes and it should be made sure that SCPFEM framework gives accurate results without any numerical issues related to stability and accuracy of jacobian for all the deformation modes encountered during its simulation as well. SCPFEM simulations could also be performed on CPU-GPU architecture to increase its computational efficiency and future works should focus on this along with validating this tool for more deformation processes. As we increase the size of system (by using more number of elements in FE mesh or more number of crystals per RVE for each integration point) to perform complex metal forming operations using SCPFEM framework, in future the computational resources will very soon become bottleneck. Therefore, parallel implementation of SCPFEM framework on CPU-GPU architecture would be very beneficial and will be helpful in realizing the real potential of this tool. Future work on these toolsets would help in implementation of these numerical tools in practice for industries and their proper utilization can lead to accelerated insertion of new and improved materials into practice.

REFERENCES

ABAQUS (2010). Providence, RI, USA., © Dassault Systèmes Simulia Corp.

Abed-Meraim, F., Balan, T., Altmeyer, G., 2014. Investigation and comparative analysis of plastic instability criteria: application to forming limit diagrams. Int. J. Adv. Manuf. Tech. 71, 1247–1262.

Adams, B.L., Kalidindi, S.R., Fullwood, D., 2013. Microstructure-sensitive Design for Performance Optimization, Butterworth-Heinemann.

Akpama, H.K., Ben Bettaieb, M., Abed-Meraim, F., 2016. Numerical integration of rate - independent BCC single crystal plasticity models: comparative study of two classes of numerical algorithms. Int. J. Num. Meth. Eng. 108, 363–422.

Akpama, H.K., Ben Bettaieb, M., Abed-Meraim, F., 2017. Localized necking predictions based on rate-independent self-consistent polycrystal plasticity: Bifurcation analysis versus imperfection approach. Int. J. Plast. 91, 205–237.

Alharbi, H.F., Knezevic, M., Kalidindi, S.R., 2010. Spectral Approaches for the Fast Computation of Yield Surfaces and First-Order Plastic Property Closures for Polycrystalline Materials with Cubic-Triclinic Textures. Computers, Materials and Continua. 15 (2), 153-172.

Alharbi, H.F., Kalidindi, S.R., 2015. Crystal plasticity finite element simulations using a database of discrete Fourier transforms. Int. J. Plast. 66, 71–84.

Anand L., 2004. Single-crystal elasto-viscoplasticity: application to texture evolution in polycrystalline metals at large strains. Comput. Methods Appl. Mech. Eng. 193, 5359–83.

Asaro, R.J., Needleman, A., 1985. Texture development and strain hardening in rate dependent polycrystals. Acta Metall. 33, 923–953.

Bachu, V., Kalidindi, S.R., 1998. On the accuracy of the predictions of texture evolution by the finite element technique for fcc polycrystals. Materials Science and Engineering a-Structural Materials Properties Microstructure and Processing 257(1): 108-117.

Barlat, F., 1987. Crystallographic texture, anisotropic yield surfaces and forming limits of sheet metals. Mater. Sci. Eng. 91, 55–72.

Barlat, F., 2007. Constitutive modeling for metals. Advanced methods in material forming: 1-18.

Beaudoin, A.J., Dawson, P.R., Mathur, K.K., Kocks, U.F., 1995. A hybrid finite element formulation for polycrystal plasticity with consideration of macrostructural and microstructural linking. Int. J. Plast. 11, 501–521.

Boudeau, N., Gelin, J.C., Salhi, S., 1998. Computational prediction of the localized necking in sheet forming based on microstructural material aspects. Comput. Mater. Sci. 11, 45–64.

Bronkhorst, C.A., Kalidindi, S.R., Anand, L., 1992. Polycrystalline plasticity and the evolution of crystallographic texture in FCC metals. Philos. Trans. Phys. Sci. Eng. 341 443–477.

Brown, S.B., Kim, K.H., Anand, L., 1989. An internal variable constitutive model for hot working of metals. Int. J. Plast. 5(2): 95-130

Bunge, H., Esling, C., 1984. Texture Development by Plastic Deformation. Scripta Metall. 18, 191–195.

Bunge, H.-J., 1993. Texture Analysis in Materials Science. Mathematical Methods, Cuvillier Verlag, Göttingen.

Callister, W.D.J., 2007. Materials science and engineering : an introduction, John Wiley and Sons.

Cao, J., Yao, H., Karafillis, A., Boyce, M.C., 2000. Prediction of localized thinning in sheet metal using a general anisotropic yield criterion. Int. J. Plast. 16, 1105–1129.

Chockalingam, K., Tonks, M.R., Hales, J.D., Gaston, D.R., Millett, P.C., Zhang, L., 2013. Crystal plasticity with Jacobian-Free Newton–Krylov. Computational Mechanics: 1-11.

Considère, A., 1885. Mémoire sur l'emploi du fer et de l'acier dans les constructions. Ann. Ponts et Chaussées 9, 574–775.

Dudzinski, D., Molinari, A., 1991. Perturbation analysis of thermoviscoplastic instabilities in biaxial loading. Int. J. Solids Struct. 27 (5), 601–628.

Eghtesad, A., Barrett, T.J., Germaschewski, K., Lebensohn, R.A., McCabe, R.J., Knezevic, M., 2018a. OpenMP and MPI implementations of an elasto-viscoplastic fast Fourier transform-based micromechanical solver for fast crystal plasticity modelling. Advances in Engineering Software 126, 46–60.

Eghtesad, A., Zecevic, M., Lebensohn, R.A., McCabe, R.J., Knezevic, M., 2018b. Spectral database constitutive representation within a spectral micromechanical solver for computationally efficient polycrystal plasticity modelling. Comput Mech 61:89–104.

El Houdaigui, F., Forest, S., Gourgues, A.F., Jeulin, D., 2005. On the size of the representative volume element for isotropic elastic polycrystalline copper. In: Bai Y, editor. IUTAM symposium on mechanical behavior and micro-mechanics of nanostructured materials. Beijing, China: Springer, 171–80.

Ghosh, A.K., 1977. Tensile instability and necking in materials with strain hardening and strain-rate hardening. Acta Metall. 25, 1413–1424.

Grennerat, F., Montagnat, M., Castelnau, O., Vacher, P., Moulinec, H., Suquet, P., Duval, P., 2012. Experimental characterization of the intragranular strain field in columnar ice during transient creep. Acta Mater. 60, 3655–3666.

Gupta, A., Bettaieb, M.B., Abed-Meraim, F., Kalidindi, S.R., 2018. Computationally efficient predictions of crystal-plasticity based forming limit diagrams using a spectral database. Int. J. Plas. (103): 168-187.

Haddag, B., Abed-Meraim, F., Balan, T., 2009. Strain localization analysis using a large deformation anisotropic elastic–plastic model coupled with damage. Int. J. Plast. 25, 1970–1995.

Hill, R., 1952. On discontinuous plastic states, with special reference to localized necking in thin sheets. J. Mech. Phys. Solids 1, 19–30.

Hosford, W.F., Caddell, R.M., 1993. Metal Forming: Mechanics and Metallurgy, second ed. Prentice Hall, Englewood Cliffs, NJ.

Hutchinson, J. W., 1976. Bounds and Self-Consistent Estimates for Creep of Polycrystalline Materials. Proceedings of the Royal Society of London. A. Mathematical and Physical Sciences 348(1652): 101-127.

Hutchinson, J.W., Neale, K.W., Needleman, A., 1978a. Sheet necking – I. Validity of plane stress assumptions of the long-wavelength approximation. In: Koistinen, D.P., Wang, N.M. (Eds.), Mechanics of Sheet Metal Forming. Plenum, pp. 111–126.

Hutchinson, J.W., Neale, K.W., 1978b. Sheet necking – II. Time-independent behavior. In: Koistinen, D.P., Wang, N.M. (Eds.), Mechanics of Sheet Metal Forming. Plenum, pp. 127–153.

Hutchinson, J.W., Neale, K.W., 1978c. Sheet necking – III. Strain-rate effects. In: Koistinen, D.P., Wang, N.M. (Eds.), Mechanics of Sheet Metal Forming. Plenum, pp. 269–285.

Inal, K., Neale, K.W., Aboutajeddine, A., 2005. Forming limit comparisons for FCC and BCC sheets. Int. J. Plast. 1255–1266.

Kalidindi, S.R., Bronkhorst, C.A., Anand, L., 1992. Crystallographic texture evolution in bulk deformation processing of FCC metals. J. Mech. Phys. Solids 40, 537–569.

Kalidindi, S.R., Anand, L., 1994. Macroscopic shape change and evolution of crystallographic texture in pre-textured FCC metals. Journal of the Mechanics and Physics of Solids, 42(3): 459-490.

Kalidindi, S. R., Schoenfeld, S.E., 2000. On the prediction of yield surfaces by the crystal plasticity models for fcc polycrystals. Materials Science and Engineering a-Structural Materials Properties Microstructure and Processing 293(1-2): 120-129.

Kalidindi, S.R., Bhattacharyya, A., Doherty, R.D., 2004. Detailed analysis of grain-scale plastic deformation in columnar polycrystalline aluminum using orientation image mapping and crystal plasticicty models. Proc. R. Soc. A 460: 1935-1956.

Kalidindi, S.R., Duvvuru, H.K., 2005. Spectral methods for capturing crystallographic texture evolution during large plastic strains in metals. Acta Mater. 53 (13), 3613–3623.

Kalidindi, S.R., Duvvuru, H.K., Knezevic, M., 2006. Spectral calibration of crystal plasticity models. Acta Mater. 54 (7), 1795–1804.

Kalidindi, S.R., Knezevic, M., Niezgoda, S., Shaffer, J., 2009. Representation of the orientation distribution function and computation of first-order elastic properties closures using discrete Fourier transforms. Acta Mater. 57, 3916–3923.

Kalidindi, S.R., Gupta, A.,Popova, E., 2018. Computationally efficient crystal plasticity simulations using spectral databases. Handbook of Materials Modeling, 2nd ed., Springer, 1-26.

Keeler, S.P., Backofen, W.A., 1963. Plastic instability and fracture in sheets stretched over rigid punches. Trans. ASM 56, 25–48.

Khan, A.S., Baig, M., 2011. Anisotropic responses, constitutive modeling and the effects of strain-rate and temperature on the formability of an aluminum alloy. Int. J. Plast. 27, 522–538.

Kim, J.H., Lee, M.-G., Kim, D., Barlat, F., 2013. Numerical procedures for predicting localization in sheet metals using crystal plasticity. Comput. Mater. Sci. 72, 107–115.

Knezevic, M., Kalidindi, S.R., Fullwood, D., 2008. Computationally efficient database and spectral interpolation for fully plastic Taylor-type crystal plasticity calculations of face-centered cubic polycrystals. Int. J. Plast. 24, 1264–1276.

Knezevic, M., Kalidindi, S.R., Mishra, R.K., 2008. Delineation of first-order closures for plastic properties requiring explicit consideration of strain hardening and crystallographic texture evolution. Int. J. Plas. 24(2): 327-342.

Knezevic, M., Al-Harbi, H.F., Kalidindi, S.R., 2009. Crystal plasticity simulations using discrete Fourier transforms. Acta Mater. 57, 1777–1784.

Knezevic, M., Savage, D.J., 2014. A high-performance computational framework for fast crystal plasticity simulations. Comput. Mater. Sci. 83, 101–106.

Knezevic, M., Kalidindi, S.R., 2017. Crystal Plasticity Modeling of Microstructure Evolution and Mechanical Fields During Processing of Metals Using Spectral Databases. JOM, DOI:10.1007/s11837-017-2289-7.

Knockaert, R., Chastel, Y., Massoni, E., 2000. Rate-independent crystalline and polycrystalline plasticity, application to FCC materials. Int. J. Plast. 16, 179–198.

Knockaert, R., Chastel, Y., Massoni, E., 2002. Forming limits predictions using rate-independent polycrystalline plasticity. Int. J. Plast. 18, 231–247.

Kocks, U.F., Tomé, C., Wenk, H.R., 1998. Texture and Anisotropy, Cambridge University Press, Cambridge, UK.

Kocks, U.F., Mecking, H., 2003. Physics and phenomenology of strain hardening: the FCC case. Progress in Materials Science 48(3): 171-273.

Kuroda, M., Tvergaard, V., 2000. Forming limit diagrams for anisotropic metal sheets with different yield criteria. Int. J. Solids Struct. 37, 5037–5059.

Lebensohn, R., 2001. N-site modeling of a 3D viscoplastic polycrystal using fast Fourier transform. Acta Mater. 49, 2723–2737.

Lebensohn, R.A., Liu, Y., Castañeda, P.P., 2004. On the accuracy of the self-consistent approximation for polycrystals: comparison with full-field numerical simulations. Acta Materialia 52(18): 5347-5361.

Lebensohn, R.A., Tome, C.N., Castaneda, P.P., 2007. Self-consistent modelling of the mechanical behaviour of viscoplastic polycrystals incorporating intragranular field fluctuations. Philosophical Magazine, 87(28): 4287-4322.

Lebensohn, R., Brenner, R., Castelnau, O., Rollett, A., 2008. Orientation image-based micromechanical modelling of subgrain texture evolution in polycrystalline copper. Acta Mater. 56, 3914–3926.

Lévesque, L., Inal, K., Neale, K.W., Mishra, R.K., 2010. Numerical modeling of formability of extruded magnesium alloy tubes. Int. J. Plast. 26, 65–83.

Li, D.S., Garmestani, H., Schoenfeld, S., 2003. Evolution of crystal orientation distribution coefficients during plastic deformation. Scr. Mater. 49, 867–872.

Lubliner, J., 2008. Plasticity theory, Courier Corporation.

Manopulo, N., Hora, P., Peters, P., Gorji, M., Barlat, F., 2015. An extended Modified Maximum Force Criterion for the prediction of localized necking under non-proportional loading. Int. J. Plast. 75, 189–203.

Mansouri, L.Z., Chalal, H., Abed-Meraim, F. 2014. Ductility limit prediction using a GTN damage model coupled with localization bifurcation analysis, Mech. Mater., 76, 64–92.

Marciniak, Z., Kuczynski, K., 1967. Limit strains in processes of stretch-forming sheet metal. Int. J. Mech. Sci. 9 (9), 609–620.

Marciniak, Z., Kuczynski, K., Pokora, T., 1973. Influence of Plastic Properties of a Material on Forming Limit Diagram for Sheet-Metal in Tension." Int. J. Mech. Sci. 15(10): 789-800.

Marciniak, Z., Kuczynski, K., 1979. Forming Limit Curve for Bending Processes. Int. J. Mech. Sci. 21(10): 609-621.

Marciniac, Z., Duncan, J.L., Hu, S.L., 2002. Mechanics of Sheet Metal Forming. Butterworth-Heinemann.

MATLAB, 2018. 9.7.0.1190202 (R2019b), Natick, Massachusetts: The MathWorks Inc.

Mathur, K., Dawson, P.R., 1989. On modelling the development of crystallographic texture in bulk forming processes. Int. J. Plast. 5, 67–94.

McDowell, D.L., Kalidindi, S.R., 2016. The materials innovation ecosystem: A key enabler for the Materials Genome Initiative. MRS Bulletin, 41(04), 326-337.

McGinty, R.D., McDowell, D.L., 2004. Application of Multiscale Crystal Plasticity Models to Forming Limit Diagrams. J. Eng. Mater. Technol. 126(3), 285–291.

Mihaila, B., Knezevic, M., Cardenas, A., 2014. Three orders of magnitude improved efficiency with high-performance spectral crystal plasticity on GPU platforms. Int. J. Numer. Methods Eng. 97, 785–798.

Molinari, A., Clifton, R., 1987. Analytical characterization of shear localization in thermo-visco-plastic solids. J. Appl. Mech. 54, 806–812.

Molinari, A., Canova, G.R., Ahzi, S., 1987. A self consistent approach of the large deformation polycrystal viscoplasticity. Acta Metallurgica 35(12): 2983-2994.

Neale, K.W., Chater, E., 1980. Limit strain predictions for strain-rate sensitive anisotropic sheets. Int. J. Mech. Sci. 22, 563–574.

Needleman, A., Asaro, R.J., Lemonds, J., Peirce, D., 1985. Finite element analysis of crystalline solids. Computer Methods in Applied Mechanics and Engineering, 52(1-3): 689-708.

Neil, C.J., Agnew, S.R., 2009. Crystal plasticity-based forming limit prediction for non-cubic metals: Application to Mg alloy AZ31B. Int. J. Plast. 25, 379–398.

Pablo, J.J., Jackson, N.E., Webb, M.A., Chen, L.Q., Moore, J.E., Morgan, D., Jacobs, R., et al., 2019. New frontiers for the materials genome initiative. NPJ Compu. Mat., 5:41.

Pan, J., Rice, J.R., 1983. Rate sensitivity of plastic flow and implications for yield-surface vertices. Int. J. Sol. Struc. 19(11): 973-987.

Raabe, D., Wang, Y., Roters, F., 2005. Crystal plasticity simulation study on the influence of texture on earing in steel. Comput. Mater. Sci. 34, 221–234.

Reimann, D., Nidadavolu, K., Hassan, H., Vajragupta, N., Glasmachers, T., Junker, P., Hartmaier, A., 2019. Modeling Macroscopic Material Behavior With Machine Learning Algorithms Trained by Micromechanical Simulation. Frontiers in Materials, 6(181), 1-19.

Rice, J.R., 1976. The localization of plastic deformation. In: 14th International Congress of Theoretical and Applied Mechanics, 207–220.

Roters, F., Eisenlohr,P., Hantcherli, L., Tjahjanto, D.D., Bieler, T.R., Raabe, D., 2010. Overview of constitutive laws, kinematics, homogenization and multiscale methods in crystal plasticity finite-element modeling: Theory, experiments, applications. Acta Materialia, 58(4): 1152-1211.

Rudnicki, J.W., Rice, J.R. 1975. Conditions for the localization of deformation in pressure-sensitive dilatant materials. J. Mech. Phys. Solids 23, 371–394.

Savage, D. J., Knezevic, M., 2015. Computer implementations of iterative and non-iterative crystal plasticity solvers on high performance graphics hardware. Comp. Mech. 56, 677–690.

Schwindt, C., Schlosser, F., Bertinetti, M.A., Signorelli, J.W., 2015. Experimental and Visco-Plastic Self-consistent evaluation of forming limit diagrams for anisotropic sheet metals: An efficient and robust implementation of the M-K model. Int. J. Plast. 73, 62–99.

Serenelli, M. J., Bertinetti, M. A., Signorelli, J. W., 2011. Study of limit strains for FCC and BCC sheet metal using polycrystal plasticity. Int. J. Solids Struct. 48(7), 1109-1119.

Signorelli, J.W., Bertinetti, M.A., Turner, P.A., 2009. Predictions of forming limit diagrams using a rate-dependent polycrystal self-consistent plasticity model. Int. J. Plast. 25, 1–25.

Stören, S., Rice, J.R., 1975. Localized necking in thin sheets. J. Mech. Phys. Solids 23 (6), 421–441.

Swift, H.W., 1952. Plastic instability under plane stress. J. Mech. Phys. Solids 1, 1–18.

Szyndler, J., Madej, L., 2014. Effect of number of grains and boundary conditions on digital material representation deformation under plane strain. Arch. Civ. Mech. Eng. 14, 360–369.

Tadano, Y, Yoshida, K., Kuroda, M., 2013. Plastic flow localization analysis of heterogeneous materials using homogenization-based finite element method. Int. J. Mech. Sci. 72, 63–74.

Taylor, G.I., 1938. Plastic strains in metals. J. Inst. Metals 62, 307–324.

Van Houtte, P., 1994. Application of plastic potentials to strain rate sensitive and insensitive anisotropic materials. Int. J. Plast. 10, 719–748.

Van Houtte, P., Li, S., Seefeldt, M., Delannay, L., 2005. Deformation texture prediction: from the Taylor model to the advanced Lamel model. Int. J. of Plas. 21(3): 589-624.

Wang, H., Wu, P.D., Boyle, K.P., Neale, K.W., 2011. On crystal plasticity formability analysis for magnesium alloy sheets. Int. J. Solids Struc. 48, 1000–1010.

Wu, P.D., MacEwen, S.R., Lloyd, D.J., Neale, K.W., 2004. Effect of cube texture on sheet metal formability. Mater. Sci. Eng. A 364, 182–187.

Wu, P.D., Neale, K.W., Van der Giessen, E., 1997. On crystal plasticity FLD analysis. Proc. R. Soc. Lond. A 453, 1831–1848.

Wu, P.D., Neale, K.W., Van der Giessen, E., Jain, M., Makinde, A., MacEwen, S.R., 1998. Crystal plasticity forming limit diagram analysis of rolled aluminum sheets. Metall. Mater. Trans. A 29, 527–535.

Yoshida, K., Ishizaka, T., Kuroda, M., Ikawa, S, 2007. The effects of texture on formability of aluminum alloy sheets. Acta Mater. 55(13), 4499-4506.

Yoshida, K., Kuroda, M., 2012. Comparison of bifurcation and imperfection analyses of localized necking in rate-independent polycrystalline sheets. Int. J. Solids Struct. 49, 2073–2084.

Yuan, M., Paradiso, S., Meredig, B., Niezgoda, S.R., 2018. Machine Learning–Based Reduce Order Crystal Plasticity Modeling for ICME Applications. Integrating Materials and Manufacturing Innovation, 7, 214–230.

Zecevic, M., McCabe, R.J., Knezevic, M., 2015a. Spectral database solutions to elasto-viscoplasticity within finite elements: Application to a cobalt-based FCC superalloy. Int. J. Plast. 70, 151–165.

Zecevic, M., McCabe, R.J., Knezevic, M., 2015b. A new implementation of the spectral crytsal plasticity framework in implicit finite elements. Mechanics of Materials 84: 114-126.

Zhang, L., Wang, J., 2012. Modeling the localized necking in anisotropic sheet metals. Int. J. Plast. 39, 103–118.